UNIVERSITY OF OKLAHOMA

GRADUATE COLLEGE

DESIGN, ANALYSIS AND FABRICATION OF POROUS TITANIUM IMPLANTS USING ELECTRON BEAM MELTING FOR CRANIOFACIAL APPLICATIONS

A DISSERTATION

SUBMITTED TO THE GRADUATE FACULTY

in partial fulfillment of the requirements for the

Degree of

DOCTOR OF PHILOSOPHY

By

JAYANTHI PARTHASARATHY
Norman, Oklahoma
2009

Downloaded from SHAREOK. Persistent Handle URL: https://hdl.handle.net/11244/318652

DESIGN, ANALYSIS AND FABRICATION OF POROUS TITANIUM IMPLANTS USING ELECTRON BEAM MELTING FOR CRANIOFACIAL APPLICATIONS

A DISSERTATION APPROVED FOR THE
SCHOOL OF INDUSTRIAL ENGINEERING

BY

_____

Dr. Shivakumar Raman – Chair

_____

Dr.Binil Starly – Co Chair

_____

Dr. Thomas Landers

_____

Dr.Randa L Shehab

_____

Dr.Zahed Siddique

© Copyright by JAYANTHI PARTHASARATHY 2009
All Rights Reserved.

ACKNOWLEDGEMENTS

I would like express my sincere deep sense of gratitude to Prof Dr. Shivakumar Raman, for his ever-ready guidance in the research at hand and whole hearted support and encouragement throughout the course of this study and investigation. I should specially thank Dr.Binil Starly my co-advisor for the constant review and guidance of my research and the time spared for my discussions.

I express my profound gratitude to Dr.Thomas Landers Dean, College of Engineering, for his invaluable help as committee member. I thank ever smiling Dr.Randa L Shehab Director, School of Industrial Engineering, for guidance with the IRB process and support and encouragement given to me during my time as a graduate student at the University of Oklahoma both as a director and a committee member. I must appreciate Dr.Zahed Siddique, Professor of Mechanical Engineering, for his time and very stimulating discussions in my research. I must also thank for the time and contribution of Professors Dr. Hank Grant and Dr.Trafalis Theodore.

I acknowledge and thank Dr.James Baldwin for his throwing open their facilities for the mechanical testing of the samples. I thank Dr. Olson Brandon for helping with the shear testing. I also have to acknowledge Preston Larson of Sam Noble Microscopy laboratory for helping with the SEM testing. I must thank Dr.Chandra Rai for opening his laboratory for my research. I gratefully acknowledge the help and guidance of Rebecca Cranford and Dr. Turner of Oklahoma Medical Research Foundation for facilitating the Micro CT scanning. I acknowledge the assistance rendered by Mr.Joel Young of the Physics Department and Mr.Billy and Mr.Craig of the Machine shop of school of Aerospace and Mechanical Engineering of OU.

I acknowledge and thank the staff of School of Industrial Engineering, Cheryl Carney, Jean Elva Schingledecker and Amy J Piper for their support during my graduate studies at the School of Industrial Engineering.

I am grateful to all my friends who have been a great source of inspiration and support during my graduate studies here at the School of Industrial Engineering, at the University of Oklahoma.

This research would not have been possible without the support of Dr.Andy Christensen of Medical Modeling inc. for fabrication of all the titanium models used in this study at no cost to us.

I express my heartfelt thanks to my family, my husband Parthasarathy, daughters Arathi and Preethi Srikanth for the support and encouragement given to me throughout my life without which it would not have been possible for me to get here. I have to express my gratitude to my parents, Seshadri and Kamala and my parents inlaws Srinivasan and Rajalakshmi for their blessings and support throughout.

I thank Guru Raghavendhra and my Gurus and the almighty for the immense grace and blessings that has made my aspirations a reality.

TABLE OF CONTENTS

1. INTRODUCTION 1

1.1 Factors Affecting the Longevity of the Implant **1**

1.2 Background of Materials and Fabrication methods of craniofacial implants **3**

1.3. Deficiencies with the current methods **10**

1.4 The Next Generation of Titanium Craniofacial Implants **11**

1.5 Enabling Technologies **12**

1.6. Need for the Study, Problem Statement and Methodology **13**

1.7 Aim, Objective and Scope of the Research **16**

2. LITERATURE SURVEY 18

2.1 Summary **18**

2.2 Design of Craniofacial Implants **18**

2.3 Materials used in Craniofacial Reconstruction **22**

2.4 Fabrication of Porous Titanium Parts for Biomedical Applications **29**

2.5 Characterization of Microstructure of Titanium **40**

2.6. Prediction of Mechanical Properties **41**

2.7. Experimental Methods for Mechanical Properties **43**

3. IMAGE BASED MODELING OF PATIENT SPECIFIC 46

CRANIOFACIAL IMPLANTS 46

3.1 Summary **46**

3.2 Reconstruction of External Geometry of the Porous Implant **48**

3.3 Design of Internal Architecture of the Porous Implant **58**

4. PREDICTION OF EFFECTIVE MECHANICAL PROPERTIES 62

4.1 Summary **62**

4.2 Prediction of Effective Elastic Modulus **63**

4.3 FEA Based Analysis of Mandibular Implants in Response to Masticatory Forces **66**

4.4 Results **68**

4.5 Discussion **78**

4.6 Fabrication of Porous Mandible by 3D Printing **83**

5. EVALUATION OF POROUS TITANIUM CONSTRUCTS 86

FABRICATED USING EBM 86

5.1 Summary **86**

5.2 Electron Beam Melting (EBM) **86**

5.3 Fabrication of Porous Parts **90**

5.4 Characterization of Porous EBM Titanium Parts **93**

5.5 Results **103**

5.6 Discussion **115**

6. CONCLUSION, RESEARCH CONTRIBUTIONS AND SCOPE OF FUTURE WORK **121**

6.1 Conclusion **121**

6.2 Research Contributions **122**

6.3 Scope for future work **123**

REFERENCES 124

APPENDIX **134**

LIST OF TABLES

Table 1. 1 Properties of metallic biomaterials 7

Table 3. 1 Hounsfield values of tissues 53
Table 3. 2 Estimated weight of the implant 58

Table 4. 1 Pore size, Pore volume and porosity % for 60 mm cube 65
Table 4. 2 Characteristics of the beam element model.....66
Table 4. 3 Material properties 67
Table 4. 4 Loads applied on dental implant abutments 67
Table 4. 5 Elastic modulus prediction using Gibson and Ashby's formula 69
Table 4. 6 Elastic modulus prediction using FEA method 70
Table 4. 7 Estimated properties of patient specific cranial and mandibular implants.....71
Table 4. 8 Model 3 VonMises stresses 76
Table 4. 9 Model 2 - Stress in screws of various modifications of the retention plate systems.....81

Table 5. 1 Mechanical properties of EBM processed Ti6Al4V 89
Table 5. 2 Pore and Strut sizes, number of pores and varying porosities.....91
Table 5. 3 Average strut and pore sizes for the samples (n=7).....104
Table 5. 4 EDS evaluation of elements present 107
Table 5. 5 Comparison of theoretical and actual values of weight and porosity 109
Table 5. 6 Compressive stiffness and compressive strength.....111
Table 5. 7 Elastic modulus and maximum compressive strength of cortical and trabecular bone 118

LIST OF FIGURES

Figure 1. 1 Elastic modulus of biocompatible materials 7
Figure 1. 2 a-e Procedures involved in fabrication of a titanium cranioplasty plate for correction of a large cranial defect approximately 130 X 101 mm^2 using RP and metal forming and surgical fixation 9
Figure 1. 3 (a)Mandibular tumor (b)Titanium implant using CNC machining 10
Figure 1. 4 a Mandibular substitute made from investment casting, b and c Generic mandibular reconstruction plates (www.Stryker.com) 10
Figure 1. 5 Organization of the research work.....17

Figure 2. 1 Effect of scan spacing on tensile strength 32
Figure 2. 2 Influence of peak power on tensile strength.....33
Figure 2. 3 Stress – strain curves of Ti-6Al-4V 36
Figure 2. 4 a)Average compression strength versus relative density for tested and estimated mesh structures b) ANSYS simulated results for compression stiffness versus relative density in XY orientation and Z orientation. 43

Figure 3. 1 Sequence of processes in creating patient specific porous cranial implants...47
Figure 3. 2 Roadmap for the design of mandibular implant from CT images 48
Figure 3. 3 (a) CT scan image (b) DICOM file.....49
Figure 3.4 Image data orientation.....51
Figure 3. 5 Thresholding operation 52
Figure 3. 6 Reconstructed skull model with defect 53
Figure 3. 7 (a) Skull with implant (b) Reconstructed implant external geometry 54
Figure 3. 8 (a) Thresholding operation; (b) Reconstructed mandible with defect; (c) Virtual surgical simulation and reconstruction of external geometry of the implant.....55
Figure 3. 9 (a): Canine to canine reconstruction - Model 1; (b): Premolar to sub-condylar reconstruction - Model 2; (c): Hemi mandible reconstruction -Model 3.....57
Figure 3. 10 Creating the bounding volume for 59
Figure 3. 11 Porous part enclosing the implant.....59
Figure 3. 12 (a) Bounding porous cube intersected with the implant (b) Resultant porous implant after the boolean operation with interconnected pores (c) Porous cranial implant fitted to the skull.....60
Figure 3. 13 (a) Bounding porous cube intersected with the implant (b) Resultant porous implant after the boolean operation with interconnected pores (c) Porous mandibular implant fitted to the right normal mandible 60

Figure 4. 1 a) RVE with applied boundary conditions 64
Figure 4. 2 Beam elements model.....65
Figure 4. 3 Loads and constraints on mandibular models 1, 2 and 3 68
Figure 4. 4 Effective elastic modulus predicted by FEA and method.....70
Figure 4. 5 Comparison of the properties of the solid and porous titanium implants, and its bone equivalent (a) cranial implant (b) mandible implant (Model3).....71
Figure 4. 6 Model 1 Von Mises stresses under masticatory load.....72
Figure 4. 7Model 1 Maximum Principal strain 73

Figure 4. 8 Model 1 X Y and Z Displacement Effective E Vs Displacement 73
Figure 4. 9 Model 1 Y displacement 74
Figure 4. 10 Model 2 Von Mises stresses 74
Figure 4. 11 Maximum Principal strain 75
Figure 4. 12 Model 2 X Y and Z Displacement Vs Effective E 75
Figure 4. 13 Model 3 Von Mises stresses Maximum Stresses seen at the screw joints. ...76
Figure 4. 14 Model 3 Load Vs Max principal stress 77
Figure 4. 15 Model 3 Effect of elastic modulus on 77
Figure 4. 16 Model 3 X Y Z Displacement Effective Vs Displacement 78
Figure 4. 17 Model 2c – finalized design - VonMises stress 81
Figure 4. 18 Model 3b - Final design - VonMises stresses 82
Figure 4. 19 Model 3a and 3b comparison VonMises stress 82
Figure 4. 20 Model 3 - Maximum displacement for effective elastic modulus of 3GPa ..83
Figure 4. 21 CAD design of porous mandible for 3D printing 84
Figure 4. 22 3DP model of porous mandible 84

Figure 5. 1 Steps in fabrication of an EBM part 88
Figure 5. 2 Schematic of representation of working of EBM 90
Figure 5. 3 Design of cube with porosity 75.83 % 91
Figure 5. 4 The designed porosity of Ti6Al4V parts fabricated 93
Figure 5. 5 Optical Microscope – surface characterization 94
Figure 5. 6 SEM Carl Zeiss 960 96
Figure 5. 7 Micro CT Imaging, MIMICS 2D image thresholding 97
Figure 5. 8 Helium gas Pycnometer used for estimation of pore volume 98
Figure 5. 9 MTS alliance RT30 electromechanical testing test frame 101
Figure 5. 10 Fixture for shear testing Figure 5. 11 Porous titanium part.....102
Figure 5. 12 Fixture bolted to the tensile testing machine 102
Figure 5. 13 Optical microscope images set 1, 2, 3 and 4 (scale bar = 2mm) 104
Figure 5. 14 (a). SEM image of surface microstructure showing complete melting of powder particles. (b) SEM image of showing pore size 105
Figure 5. 15 EDS analysis of Ti6Al4V surface 106
Figure 5. 16 SEM image showing Silica bead 106
Figure 5. 17 3D reconstruction and analysis of micro-CT data 107
Figure 5. 18 Porosity Vs Surface area micro CT data 108
Figure 5. 19 Comparison of Theoretical, Experimental and Micro CT Porosity.....109
Figure 5. 20 Stress strain curves 50.75, 60.41 and 70.32 % porosity.....110
Figure 5. 21 Stress strain curves 49.75 % porosity 110
Figure 5. 22 Porosity Vs Compressive stiffness 112
Figure 5. 23 Porosity Vs Compressive strength σ_{max} 112
Figure 5. 24 Sheared part within the fixture 114
Figure 5. 25 Porosity Vs Shear modulus 115

ABSTRACT

Patient specific implants for the reconstruction of craniofacial defects have gained importance due to better performance over their generic counterparts. This is due to, the precise adaptation to the region of implantation, reduced surgical times, and better cosmesis. Titanium implants built using traditional manufacturing processes are often heavy compared to the parts they replace and can cause discomfort to the patients. The variation in mechanical properties as elastic modulus between the implant and bone reduces the longevity of the implant. In mandible reconstruction, post implant dental reconstruction poses additional problems. Recent introduction of direct digital manufacturing technologies as electron beam melting (EBM) and Selective Laser Melting for processing of titanium has led to a one step fabrication of near net shape porous custom titanium implants with controlled porosity to meet the requirements of the anatomy and functions at the region of implantation.

The first part of this research is directed towards development of a design strategy using representative volume element based technique, in which precisely defined porous implants with customized stiffness values are designed to match the stiffness and weight characteristics of surrounding healthy bone tissue. Dental abutment structures have been incorporated into the mandibular implant. Finite element analysis is used to assess the performance of the implant under masticatory loads. This design strategy lends itself very well to rapid manufacturing technologies such as Selective Laser Sintering (SLS) and Electron Beam Melting (EBM) processes.

The second part of the research consists of an image based micro-structural analysis and mechanical characterization of porous Ti6Al4V structures fabricated using the EBM

rapid manufacturing process. SEM studies have indicated complete melting of the powder material with no evidence of poor inter-layer bonding. Micro-CT scan analysis of the samples indicate well formed titanium struts and fully interconnected pores with porosities varying from 49.75 – 70.32%. Compression tests of the samples showed effective stiffness values ranging from 0.57 ($\pm$0.05) – 2.92($\pm$0.17) GPa and compressive strength values of 7.28($\pm$0.93) - 163.02($\pm$11.98) MPa. For nearly the same porosity values of 49.75% and 50.75%, with a variation in only the strut thickness in the sample sets, the compressive stiffness and strength decreased significantly from 2.92GPa to 0.57GPa (80.5% reduction) and 163.02MPa to 7.28MPa (93.54 % reduction) respectively. Grain density of the fabricated Ti6Al4V structures was found to be 4.423g/cm^3 equivalent to that of dense Ti6Al4V parts fabricated using conventional methods.

In conclusion, a methodology for fabrication of craniofacial implants that would have better aesthetics, and improved masticatory functions, enhancing patient comfort and compliance, has been developed. From a mechanical strength viewpoint, we have found that the porous structures produced by the electron beam melting process presents a promising rapid manufacturing process for the direct fabrication of customized titanium implants for enabling personalized medicine with reduced lead time and cost.

CHAPTER 1

1. INTRODUCTION

A surgeon operating on any patient has the objective to make his patient better to the best of his ability. There are 206 bones in the human body, all of which differ in size, shape and function from each other and from person to person making any generalization difficult. Population standard parameters for age, sex and race have wide variations making the readily available generic implants difficult to be adapted for specific needs. Precise prediction of performance and longevity of these implants in a dynamic clinical situation is also difficult. Hence it would be very useful for the surgeon to be aided by standard practice and proven methods in engineering wherein the performance of the reconstructed implants/prosthesis can be predicted with accuracy.

1.1 Factors Affecting the Longevity of the Implant

Success and longevity of implants depends upon factors such as material characteristics, design of the implant, region of implantation, patient specific response and surgeon's skill**.** Of these factors material properties and design of the implants can be studied with good accuracy using robust engineering principles. The design, material properties and advantages of custom designed implants will be discussed herein. To make the right choice of material for a specific implant and predict the long term effects, it is pertinent to understand the properties of tissues - bone, biomaterials available and their mechanical and chemical properties and the interaction at the site of implantation between the host tissues and implant material. Hence, the properties of bone and materials available for replacement will be reviewed.

Skeletal structure is the first and foremost mechanical structure, the major functions of which is to transmit forces from one part of the body to another (limbs, mandible) and provide protection to internal organs such as heart, lungs and brain. Bone is a calcified structure that is continuously being remodeled dynamically by bone formation (osteoblastic) and bone resorption (osteoclastic) activity, depending on the quantum of mechanical forces transmitted. Balancing of this osteoblastic and osteoclastic activity seen in nature keeps the bone and muscles healthy performing their activities. Disuse atrophy and hypertrophy due to increased usage are well known in physiological/ pathological situations. The process of bone adaptation continues with the surgical placement of implants and is a key factor for successful retention and performance of the implant. Adaptation to the newly placed material at the bone implant interface is both chemical and mechanical. Chemical factors affecting the cellular reaction are directly related to the chemical composition of the implant material. The mechanical factors affecting the cellular reaction are the forces at the implant - host tissue interface. These factors are directly dependent on the mechanical properties of the implant material and the bone. Further the structure of bone is not uniform and has an inner less dense region – the cancellous bone and the outer denser region the cortical bone with a modulus of elasticity ranging from 0.5-20GPa. Less amount or even lack of stress transmission at the interface due to the high modulus of elasticity of the implant material leads to an imbalance in the process of bone resorption and apposition. This causes increased bone resorption as against apposition at the bone implant interface leading to loosening of the implant. This process is known as “stress shielding.” (Park & Lakes, 1992).

Increased mechanical forces at the interface also lead to failure of the implant, emphasizing the need for implants with right mechanical properties.

Replacement or reconstruction of skeletal structures can be performed using autografts, allografts, and xenografts. Autografts are tissues grafted from the same individual and is the "Gold standard" from an immune response aspect. However, it is limited by, availability of suitable donor site, additional expensive surgeries, tissue harvesting problems, secondary site of morbidity with additional patient discomfort, chances of infection both at the site of surgery and the donor site, increased surgical time, and additionally skilled surgical team (Shimko & Nauman, 2007, Schlickewei & Schlickewei, 2007, Lane & Sandhu, 1987, St.John, et al., 2003, Silber, et al., 2003). This has lead to the search of extraneous material that would be suitable without the inherent problems (Martin, et al, 1994)

1.2 Background of Materials and Fabrication methods of craniofacial implants

1.2.1 Materials

Biocompatible materials available for fabrication of implants in the present time can be enumerated as bioceramics, polymers and metals and metal alloys.

Bioceramics

Bioceramics used for fabrication of implants are calcium phosphate materials such as hydroxyapatite (HA) and tricalcium phosphate (TCP). These materials have been successfully used in orthopedic and dental applications for decades. TCP is readily

resorbed but HA is almost a permanent material. These materials have good osteoconductive properties but limited osteoinductive properties and mechanical strength (Khan, Tomin, & Lane, 2000) limiting their usage to non weight bearing regions. Alumina ceramics are very hard with high modulus of elasticity of 380 GPa almost twice that of metal alloys, limiting the stresses at the implant - bone interface causing bone resorption and aseptic loosening. Its resistance to flexion is also low and hence can be used only as an osteosynthesis plate. Zirconia (ZrO_2) has excellent mechanical properties as flexion and resistance to wear, but fracture of the implanted femoral heads has been reported (Kraay, et al 2006). Moreover fabrication of the materials to the complicated anatomical geometry is also a limiting factor.

Polymers

Polymers used in biomedical applications are Polymethylmethacrylate (PMMA), Polylactides (PLA), Polyglycolides (PGA), Polycaprolactone (PCL), Polyethylene Ultra-high-molecular-weight (UHMW). Heat cured PMMA has been used in dentistry for fabrication of dentures for several years. Cold cured PMMA (bone cements) however is not an ideal implant material as the heat produced during the polymerization could reach more than 70^0C which is more than the coagulation temperature of proteins (56^0C) and bone collagen (70^0c). Increased rate of infection is seen with PMMA cranioplasty plates as compared to other materials as titanium and ceramic implant materials (Matsuno, et al 2006). UHMW polyethylene is used for making friction components for prosthesis of hip, knee and elbow due to its mechanical properties. PLA, PLGA, PEG, PCL are being investigated as tissue engineered implant materials due to their programmable biodegradable properties. Their routine use as a clinically implantable prosthesis would

be the ultimate achievement of tissue engineering. These materials are presently being used in clinical scenarios as absorbable suture materials, and osteosynthesis plates. These materials have been experimented for closure of trephination holes and small cranial defects but cannot be used for large defects and load bearing implants.

Metals and Metal Alloys

Metals and metal alloys as stainless steel, cobalt chromium and titanium and titanium alloys have been successfully used as fracture fixation and as joint replacement materials and the expectation of their performance is increasing.

Stainless steel used for biomedical application is 316LV (ASTM F 138) austenitic, low carbon and vacuum processed. Fracture fixation plates and syringe needles made of 316LV have been used but removal of the plates has been necessitated due to corrosion (Urban, et al 2003). Moreover the modulus of elasticity of the material is above 200GPa which makes the material unusable for reconstruction prosthesis as it is intended to remain permanently inside the body.

Cobalt Chromium Alloys used for biomedical applications are Cobalt – Chromium - Molybdenum Co-Cr-Mo (ASTMF75) and Cobalt – Nickel - Chromium Molybdenum Co-Ni-Cr-Mo (ASTM F562). Other alloys with the presence of Nickel (25-30%) promise increased corrosion resistance but raises concerns about toxicity and / or immune related reactions. The modulus of elasticity is around 200 GPa i.e. ten times that of bone and leads to stress shielding and consequent loosening of the implants.

Zirconium (Zr) and Tantalum (Ta) Alloys have a high corrosion resistance due to the stability of the oxide layer that forms on the implant (Jacobs et al, 1998, Levine et al 2006). The materials also have a high wear resistance. Difficulties with forming and

machining the materials restrict their use in implant fabrication (Black, 1996). However, large streaking, and burst star artifacts have also been noticed in spinal replacements with this metal (Levi et al 1998, Wang et al 1998).

Titanium and Titanium Alloys – Titanium the supra alloy has found wide aerospace, and medical (implants) applications. Titanium has been used an implant material due to its high strength to weight ratio, corrosion resistance (Khan, Tomin, & Lane 2000, Robertson, Pierre, & Chahal, 1976) biocompatibility and osseointegration properties. Commercially pure titanium (CPTi) has been used in manufacturing of dental implants due to the ductility permitting cold working. Ti-6Al-4V (ASTM 136) and Ti-6Al-4V ELI are used as joint replacement components due to their superior mechanical properties compared to CPTi. Ti-6Al-4V is composed of $\alpha + \beta$ material phases i.e. Hexagonal close-packed (HCP) α and Body centered cubic phase (BCC) β phase. Aluminum 5.5 – 6.5 % stabilizes the α phase while Vanadium 3.5-4.5 % stabilizes the β phase. Titanium alloys are particularly preferred implant materials compared to stainless steel and Co-Cr-Mo alloys because of their high corrosion resistance due to the oxide coating (TiO_2) formed on the surface of the implant. This stable protective oxide coating protects Ti alloys from pitting corrosion, intergranular corrosion and crevice corrosion and is mainly responsible for the excellent biocompatibility of titanium alloys. Strength of titanium alloys exceeds that of stainless steel and Co-Cr-Mo alloys. The modulus of elasticity 114 GPa of titanium is much closer than stainless steel and Co-Cr-Mo alloys to that of bone and therefore less stress shielding is seen with titanium alloys. The above mentioned property along with the excellent biocompatibility and corrosion resistance makes titanium alloys the best available material for prosthesis fabrication (Hallab,

Urban, & Jacobs, 2004). Figure 1.1 shows the comparative elastic modulus of biocompatible materials and Table 1.1 shows the properties of metallic biomaterials used presently. From the representations it can be observed that most of the materials used for implantation have much higher elastic modulus compared to bone. Among the metallic materials it can be seen that Ti6Al4V has the lowest elastic modulus

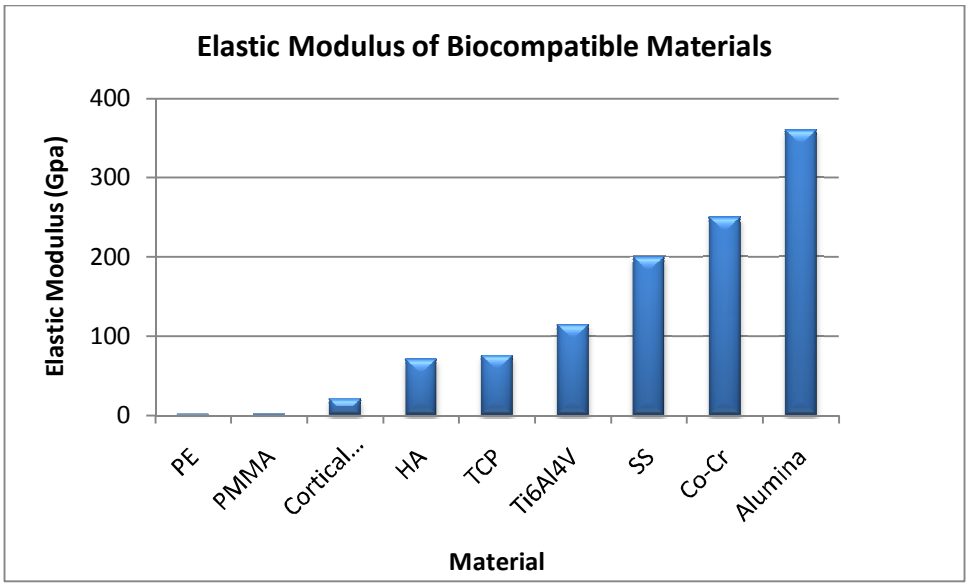


Figure 1. 1 Elastic modulus of biocompatible materials

Table 1. 1 Properties of metallic biomaterials

Characteristics	S-Steel	Co-Cr-Mo	Titanium
Stiffness	High	Medium	Low
Strength	Medium	Medium	High
Corrosion Resistance	Low	Medium	High
Biocompatibility	Low	Medium	High

A very important reason for titanium being the preferred implant material is its unique property of **osseointegration** that is the direct structural and functional connection between living bone and the surface of a load-bearing implant, making the implant and

adjoining bone function in unison. The process was first reported by (Brånemark, et al 1977, Albrektsson, et al 1983).

1.2.2 Current Status of Fabrication of Titanium Patient Specific Craniofacial Implants

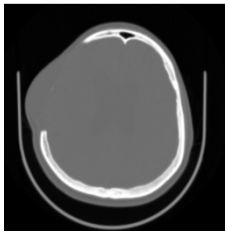
Custom designed and fabricated implants are found to have advantages of better fit, reduced operating time, lesser chances for infection, faster recovery, and better cosmesis in craniofacial surgery (Connell et al 1999, D'Urso, et al 2000, Ming et al 2002). Currently custom designed craniofacial implants are fabricated using reverse engineering, medical image processing and rapid prototyping (RP).

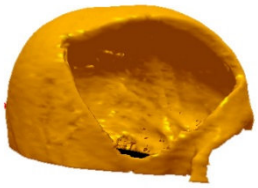
Indirect Prosthesis Fabrication

Indirect prosthesis fabrication involves an intermediary step wherein the implant is not fabricated directly from the CT scan data. A model of the part with the defect is fabricated using RP. The model is then used as a replica or template of the actual region of interest with the defect and secondary processing methods as forming (Chen et al 2006) is used to produce the actual implant.

Figure 1.2 a – e shows the processes involved in fabricating a custom titanium mesh cranioplasty plate (Parthasarathy and Parthiban, 2008). RP model of the skull is made that is an exact replica of the region of interest. A titanium mesh is then formed into the shape of the defect and is fitted surgically. This process makes a well fitting prosthesis and is very useful in treating large cranial defects with advantages of reduced, operating time, healing time and hospitalization period which eventually leads to reduced cost to the patient. However, the process involves fabrication of the RP model at an additional

cost and time. Moreover the same methodology cannot be used for fabrication of more complex implants that require exact anatomic reconstruction for proper function and aesthetics e.g. mandible.


(a)


(b)


(c)


(d)


(e)

Figure 1. 2 a-e Procedures involved in fabrication of a titanium cranioplasty plate for correction of a large cranial defect approximately 130 X 101 mm^2 using RP and metal forming and surgical fixation

Another case of mandibular tumor is seen in Figure in 1.3 a**.** An example of a mandible reconstruction prosthesis made from titanium is shown in Figure 1.3 b. Though the part geometry conforms anatomically to the region to be replaced and is made of the right material it is still unusable as the weight of the part is much more than its bone equivalent as it is a dense structure, density of bone being 19.90 g/cm^3 (Torontolo, et al 2000), and that of titanium being 4.43 g/cm^3 (ET UK LTD). Figure 1.3.c shows the generic mandibular reconstruction plate placed in situ surgically. Martola, et al (2007) suggested plates that match closely the three-dimensional shape of the mandible to avoid requirements of intra operative bending leading to fractured reconstruction plates while in use.



(a) (b) (c)

Figure 1. 3 (a)Mandibular tumor (b)Titanium implant using CNC machining (c) Generic mandibular plate placed in situ

Yaxiong et al (2003) used investment casting for fabrication of custom mandibular substitutes as seen in Figure 1.4 a, to be used instead of the presently used off the shelf generic mandibular reconstruction plates seen Figure 1.4 b, and c. This method of making holes in the implant (Figure 1.4a) is not a controlled method of manufacturing and therefore is not repeatable.

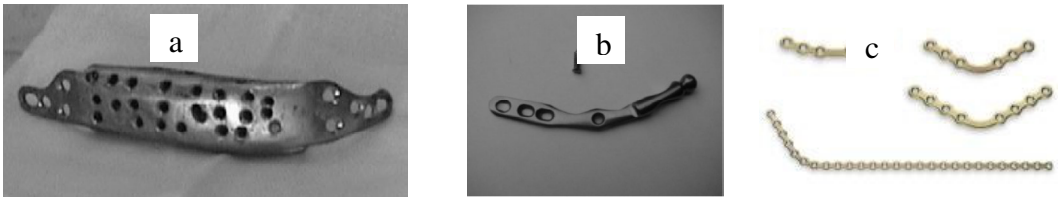


Figure 1. 4 a Mandibular substitute made from investment casting, b and c Generic mandibular reconstruction plates (www.Stryker.com)

1.3. Deficiencies with the current methods

Though the above mentioned processes are being used presently and have improved treatment modalities, and patient comfort, still have inherent deficiencies enumerated below:

i. Titanium implants built using this process are often heavy and can cause discomfort to the patients. The Young's modulus of titanium is almost 5 times

that of cortical bone and results in stress shielding effects (Robertson et al 1976, Ryan et al 2006).

ii. The secondary processing increases cost and time, resulting in subsequent delay in treatment and increased cost of health care to the patient / insurance provider.

iii. RP models are used only as sacrificial models and secondary manufacturing methodologies as forming, casting and swaging are required to be used for fabrication of the final implants.

Therefore, it is imperative to explore methodologies for building of netshaped porous parts with repeatable mechanical properties. Advantages being, reduction of weight of the implant bringing it close to that of the natural bone and also reduction of effective stiffness of the material thereby reducing the stress shielding effects making way for increased longevity of implants (Parthasarathy et al., 2008; Parthasarathy et al., 2009, Starly et al., 2003, Wei et al., 2005).

1.4 The Next Generation of Titanium Craniofacial Implants

The above mentioned deficiencies have to be addressed in the fabrication of the next generation of implants. New generation of implants would require being porous enabling the in-growth of healthy bone tissue for additional implant fixation and stabilization. Newer implants would need to conform to the external shape of the defect site that is intended to be replaced. More importantly, the effective elastic modulus of the implant should match that of surrounding tissue. Ideally the weight of the implant should also equal to the weight of the tissue that is being replaced leading to increased patient comfort. All of the above requirements would have to be made at an affordable cost that

is at least equal to if not less than the present healthcare costs and with the least time required.

Therefore an ideal design strategy for a craniofacial implant would determine porosity % that would have an elastic modulus of .5 - 20 GPa equivalent to that of cranial bone and weight equal to that of bone (density of cranial bone $2g/cm^3$). Size of pores would be 500µm to 2000 µm to facilitate tissue ingrowth.

Advantages of the methodology would include:

i. direct fabrication of the implant without the need for the template
ii. conformance of the implant to the normalized shape of the part that it replaces
iii. mechanical properties being close to that of the region of implantation and
iv. repeatability of implant properties.

1.5 Enabling Technologies

This necessitates exploration of advanced manufacturing technologies since conventional manufacturing processes fail to produce the desired porosity in the structure. Advanced manufacturing processes based on layered manufacturing principles do provide an alternative for the fabrication of patient specific porous implants.

Recent advances in computer imaging and processing of graphic data from CT/MRI scans leading to development of medical imaging softwares such as MIMICS™, 3D Doctor, and Biobuild, and advances in layer manufacturing technologies with Electron Beam and Lasers using titanium powder, have opened a new horizon for direct fabrication of next generation of custom implants with the desired external and internal characteristics. CT scan and RP are layer based technologies and transfer of data from CT

scan for RP manufacturing has been performed with good precision in the past thus making it the chosen method of fabrication of direct custom titanium implants.

CAD/CAM based layered manufacturing techniques have found applications in near net shape fabrication of porous parts with controlled porosity. The recent introduction of Electron Beam Melting (EBM) and Direct Metal Laser Sintering (DMLS) processes allow a direct digitally enabled fabrication of porous custom titanium implants with controlled porosity and desired external and internal characteristics (Harrysson, O., and Cormier,D., 2006; Lin et al., 2007).

Several researchers have successfully attempted at preparing porous medical grade titanium alloy as medical implants through commercially available rapid manufacturing technologies.

1.6. Need for the Study, Problem Statement and Methodology

Recently, Electron Beam Melting (EBM) has been studied as a feasible method for manufacturing patient specific porous orthopedic implants such as femoral stems and spinal interbody fusion cages (Harryson et al., 2005, Heinl et al., 2007). This technology has opened up a new fabrication possibility for the next generation custom implants. Electron beams when compared to lasers have greater energy density which leads to reduced build times and consequently reduced manufacturing costs. The high energy available fully melts the metal powder resulting in dense parts with better control of the mechanical properties of the fabricated porous parts. Successful use of this technology for implant fabrication will result in customized features for faster rehabilitation, increased longevity, better functionality and cosmesis apart from reducing surgical time. Some essential factors for consideration while developing a design strategy for porous

implants include pore size and shape for the in-growth of healthy tissue, weight and mechanical properties, manufacturability and economic viability of the final implant.

EBM as a metal rapid prototyping process has not been used for fabrication of patient specific net-shaped parts for use as cranioplasty plates and mandibular implants. Fabrication of implants from patient specific data with controlled mechanical properties and precise adaptation to the region of implantation is made possible with EBM, eliminating expensive secondary processing such as machining, forging, swaging, or forming and their related lead times. Harrysson et al (2007) studied the process of direct metal fabrication of titanium implants with tailored materials and mechanical properties using electron beam melting technology. In order to reduce the stiffness of titanium, the investigators designed cubes with porosities ranging from 60 - 96.2 % with a final effective elastic modulus ranging from 23MPa to 78MPa. However the parts had larger pores which limit the amount of tissue in-growth into the porous structures. The mechanical properties of the fabricated structures were also close to cancellous bone and cannot be used for replacing cortical bone and load bearing craniofacial structures. Also the effect of variation of pore and strut sizes on the mechanical properties of porous titanium structures with small pore sizes that facilitate tissue ingrowth have not been studied.

Methodology

This first part of the research presents a design strategy developed for a patient specific porous titanium cranial and mandibular implant with an ideal porosity and desired density taking into consideration both aesthetic and functional requirements. A representative volume element based technique is used in which precisely defined porous implants with

customized stiffness values is designed to match the stiffness and weight characteristics of surrounding healthy bone tissue. Dental abutment structures are incorporated into the mandibular implant over which fixed prosthodontic restorations can be made to address needs for improved masticatory functions. Finite element analysis is used to assess the performance of the implant under masticatory loads.

The second part of the research forms the design, fabrication and evaluation of porous titanium parts fabricated with EBM technology with porosities and pore sizes ranging from 50 - 70% and 1000 - 2000μm respectively. These features would be conducive for tissue ingrowth and can be used to replace cortical bone, cranioplasty plates and load bearing structures as in mandible or maxillary reconstruction. An image based micro-structural analysis using Micro CT scan data is used to evaluate the strut formation, porosity, and surface area. EBM as an additive manufacturing process uses temperatures as high as 1600^0C to melt powder titanium layer by layer. Scanning electron microscopy is used to evaluate the inter layer metallic bonding. Porosity of the porous titanium parts is also evaluated experimentally by Helium Pycnometry method. Compressive testing to failure, is performed calculate the stiffness and maximum load bearing, for porosities of 49.75 – 70.32% fabricated by varying pore and strut sizes. Analysis of the relationship of mechanical properties to overall porosity and the size of the solid structures is then made. Shear testing is performed to evaluate the shear modulus and strength and in turn the interlayer strength.

1.7 Aim, Objective and Scope of the Research

Aim of this research is to design, and evaluate porous titanium implants fabricated using EBM for use in craniofacial applications.

The main objectives are:

i. to develop a design strategy for a patient specific porous titanium based cranial and mandibular implant with an ideal porosity and desired density taking into consideration both aesthetic and functional requirements,

ii. to predict effective mechanical properties of porous titanium implants using finite element method and

iii. to evaluate of porous titanium fabricated with EBM

Organization of the research plan is shown in Figure 1.5

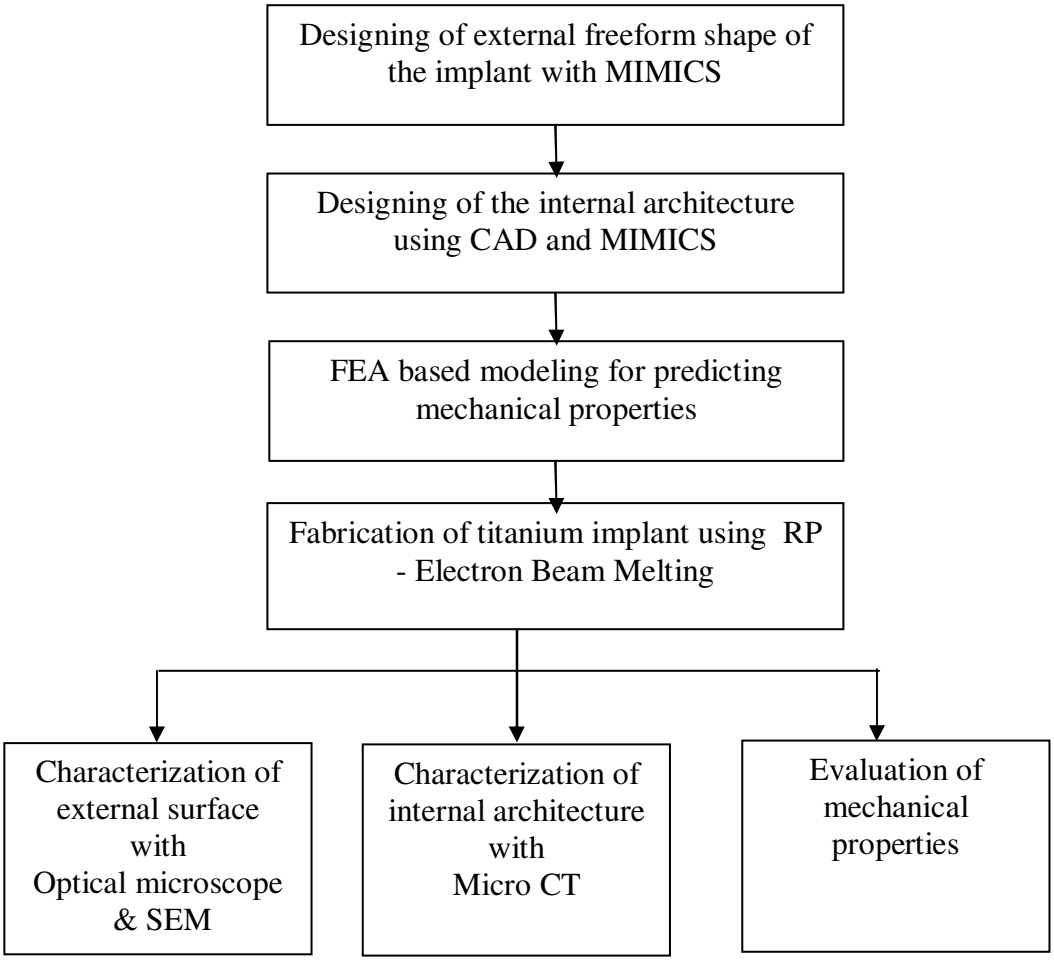


Figure 1. 5 Organization of the research work

CHAPTER 2

2. LITERATURE SURVEY

2.1 Summary

This chapter reviews the work done by researchers in CAD CAM assisted fabrication of craniofacial implants. First the work done in designing of craniofacial implants will be reviewed. Next various materials that have been used for implantation will be reviewed which will be followed by fabrication methodologies. Next characterization of the fabricated part will be reviewed followed by methodologies for evaluation of mechanical properties.

2.2 Design of Craniofacial Implants

The first step in computer assisted design of craniofacial implants involves reconstruction of external geometry of the implant from the basic input - CT scan data. The second step is to design of the internal architecture to achieve the desired mechanical properties for improved performance of the implant.

2.2.1 Reconstruction of External Geometry of the Implant

He et al (2006a) and He et al (2006b) used a method based on three - dimensional modeling based on sectional medical images, triangular fragmentation and RP technology. The designer could consult with the surgeon to arrive at an exact fitting implant for knee replacement applications. The STL file so generated could be used for fabrication of custom implants using advanced manufacturing technologies.

A spline based program known as “SURFACE” was developed by Dean et al (2003). The program used mapping processes to identify the hole in the 3D model and

reconstructed the region. A push test could also be performed to ensure the fit of the implant. The 3D CAD file of the implant was generated so that it could be used to fabricate precise fitting cranial implants with the material being the choice of the surgeon.

Hieu et al (2003) used CT scan data and used a Non Uniform Rational Spline (NURBS) based program. The authors used commercial MIMICS^{TM} program to generate the 3D model of the skull. Data from the unaffected side was mirrored and a 3D model of the implant was derived. Since the authors wanted to fabricate the implant only to fit the external architecture, used NURBS approach and fabricated the implant. The author opined that this method would reduce time and cost of the surgery. The procedure could also reduce design time and required design skills.

Wang et al (2005) designed a lateral biomechanical titanium mandibular prosthesis (BMMP) with new retention structure taking into consideration masticatory muscle attachments and soft tissue lying over the implant. Finite Element Method was used to analyze the biomechanical effects on the retention of prosthesis and the results showed that the BMMP had better load conductibility and stable retention compared to the traditional reconstruction plate. The authors report a case of reconstruction using this methodology and showed better aesthetics, continuity and function.

A custom mandibular tray was designed from clinical data to overcome problems of facial contour, jaw relationship and condylar position while using traditional reconstruction plates by Samman et al (1999). The tray was either made by casting or swaging, and bone graft material was then filled into the tray and used. The problem with this methodology is that only the external contour can be made and the interior has to be

filled with bone pieces or bone like material which could still lead to complications as resorption and infection.

A case of fabrication of custom chin implant has been reported by Singare et al (2005) wherein the authors used CT scan data for generation of the skull model and the implant. The SLA models of the skull and the implant was used for surgical planning. The finalized chin implant was cast in titanium and surgically fitted into the patient. The authors found good fit, resulting in better aesthetics and lesser time for surgery.

2.2.2. Design of Internal Architecture

Rajagopalan and Robb (2006) have enumerated the requirements of scaffolds as

i. Optimal surface texture for cell adhesion, promote cell growth and retention of differentiated cell functions.
ii. Porosity should be high enough for cell adhesion, extra cellular matrix (ECM) regeneration, and even, to allow for homogenous tissue formation
iii. Scaffolds should have adequate mechanical strength to function as the host tissue
iv. Reproducible with the same predicted properties into 3 dimensionally complex anatomic shapes.
v. Properties of the scaffolds should be able to vary depending on the anatomic site of implantation.

The Interior Architecture Design (IAD), a CAD based approach, generates scaffold layered freeform fabrication tool path without forming complicated 3D CAD scaffold models was used by Wei et al (2004, 2005), Starly et al (2006), Nam et al J (2004) and

Wettergreen et al (2005). Principle of layered manufacturing is used to determine the scaffold individual layered process planes and layered contour. The 2D characteristic patterns of the scaffold building blocks (unit cells) are used to form the interior scaffold pattern. The authors proposed a two step procedure; the first step was to decompose the 3D volumetric model into layers during model decomposition using the direct slicing method and stack them back with materials during the material accumulation in the same sequence. The external surface was defined by Non-Uniform Rationale B-Spline (NURBS) surfaces. The second step involved the generation of tool path based on Internal Architecture design (IAD) – 2D layered scaffold pattern for freeform fabrication.

Hollister, et al., in 2005 used an image based homogenization approach for designing, construction and fabrication of patient-specific (craniofacial) biomaterial scaffolds directly from CT or MRI data and used voxel density distribution to define scaffold topology which was created using image processing techniques. The voxel density distribution was then converted to data that can be used to drive a SFF fabrication machine to either directly build the scaffold or build a mold for the scaffold reverse SFF. Two image databases are used, a global one to define the anatomic shape that serves as a template in which to position the porous scaffold architecture design and a local image database for each separate microstructure design which enables the creation of scaffolds with heterogeneous structure. The authors proposed the use of stiffness (elastic modulus) for load bearing and porosity and permeability as a measure of capability to deliver biofactors and used homogenization theory to compute elasticity and permeability.

2.3 Materials used in Craniofacial Reconstruction

Craniofacial bone replacement has traditionally been performed using autogenous bone harvested from other regions as well as with alloplastic materials.

2.3.1. Natural Bone Material - Autogenous Bone Grafts

In a ten years study of cases where 1 – 3 rib grafts were used for cranioplasty in 13 patients in the age group of 11 months to 20 years (Taggard & Menezes, 2001) reported a mean operative time of 6 hours and 30 minutes.

Grant et al (2004) studied reasons for failure of bone grafts after decompressive craniectomy in children and adolescents in the age group of 4 months to 19 years and found a high incidence of bone resorption of as much as 50 %. Fresh frozen bone that was resected at the time of decompression was used for cranioplasty. The resorption increased with the size of the defect but was not related to age, sex, or the surgical procedure.

Long term evaluation of fibular grafts used for mandibular reconstruction on 112 patients showed continuous resorption in both microsurgical and free grafts in a study by Li, et al (2007)

2.3.2 Alloplastic Materials

Alloplastic materials that have been used as implant materials are classified as metallic materials and non metals. Metals used in fabrication of implants are, stainless steel, chrome cobalt, tantalum and titanium and its alloys. Nonmetals used are polymers and bioceramics.

Metals

Hippocrates (460-377 B.C) is believed to have used golden wires to treat fractures. Steel was used in the form of fracture fixation plates and screws in the 19th century. Steel with nickel plating and vanadium steels replaced carbon steels but were not corrosion resistant inside the human body. Subsequently with the search for newer more biocompatible materials stainless steels, chrome cobalt alloys (Vitallium), titanium and titanium alloys have made their way as implant materials (Sumita and Teoh 2004).

i. Stainless steel

Datti et al (1985) used stainless steel wire mesh for cranioplasty in 183 patients. The authors reported complications in 18.2% of patients for whom surgery was performed within 6 months of the first surgery.

Ueyama et al (1996) retrospectively studied the effect of single AO stainless steel plates for reconstruction of mandibular malignant tumors. The authors reported a 28% complications, extra oral plate exposure (2 cases), fracture of the plate (1 case), mandibular fracture (1 case), screw loosening (3 cases), and screw fracture (1 case). The authors further concluded from the findings that a single A-O reconstruction plate can be used for temporary reconstruction after mandibular resection or as fracture fixation plates.

ii. Chrome cobalt

Sensitivity to stainless steel screws used for treating chronic patellar dislocation has been reported by Barranco & Soloman, (1972) in a patient who developed chronic eczematous dermatitis and was asymptomatic the day after removal of the screws.

Similar hypersensitivity to cobalt-alloy plates and screws used to fix a fracture of the left radius and ulna was reported by Halpin, (1975) as cited by Singh & Dahotre, (2007).

The high modulus of elasticity and strength of stainless steel and Chrome cobalt causes stress shielding and makes the metals more useful as rigid fixation plates for fracture fixation that are functional temporarily and can be removed once the fracture has healed.

iii. Titanium and Titanium alloys

Commercially pure titanium CPTi is used in fabrication of dental implants. Osseointegration properties of titanium has been demonstrated by Brånemark, et al., (1977) which has made it the most accepted implant material till date.

Lijian, et al (2000) studied the integration of CPTi with bone by implanting a 12 mm X 3 mm piece into rabbits. The results obtained showed that titanium and bone tissue integrated closely. The action between CPTi and bone tissue was a reactive process and the integration was both physical chemical and occurred at the titanium–bone interface. The authors found titanium diffusing into the bone tissue, though the diffusion density is limited and the area of diffusion of titanium into bone tissue seen during the follow up period was up to 100 μm.

Aksakal, et al (2004) analyzed the causes of metallurgical failure of implant materials used for orthopedic applications. The materials included in the study were Chromium-Nickel (total hip prosthesis) and Chromium-Nickel and Niobium alloys (intermedullary nails), titanium (compression plates) and stainless steel vertebral implant and femoral nail plates).It was found by Scanning Electron Microscopy (SEM) that 42% of failures

occurred due to corrosion and erosion corrosion, 16.5% were due to inclusions and stress gaps that could be correlated to fatigue, 16.5% had traces of production impurities and 25% showed ductile fatigue – ductile type failures.

ASTM specifications of titanium and titanium alloys as implant materials are given hereunder

a. Mechanical specifications

ASTM F 136 – 02a (2002) specification for Ti6Al4V

Yield strength	120-124KSi
Ultimate strength	135-147 KSi
Rockwell Hardness	30-35 HRC
Elongation	10-14%
Fatigue strength @ 87KSi	>10,000,000cycles
Modulus of elasticity	114 GPa

ASTM F 136 – 02a (2002) specification for Ti6Al4V ELI

Yield strength	115 KSi
Ultimate strength	125 KSi
Rockwell Hardness	30-35 HRC
Elongation	10%
Fatigue strength @ 87KSi	>10,000,000cycles
Modulus of elasticity	114GPa

b. Chemical specifications

ASTM F 136 – 02a (2002) specification for Ti6Al4V

Aluminum Al	5.5-6.5 %

Vanadium V	3.5-4.5 %
Iron Fe	<0.3 %
Oxygen O	<0.2 %
Nitrogen N	<0.05 %
Hydrogen H	<0.01%
Carbon	<0.1 %
Titanium	Balance

ASTM F 136 – 02a (2002) specification for Ti6Al4V ELI

Aluminum Al	5.5-6.5 %
Vanadium V	3.5-4.5 %
Iron Fe	<0.25 %
Oxygen O	<0.13 %
Nitrogen N	<0.05 %
Hydrogen H	<0.01%
Carbon	<0.08 %
Titanium	Balance

ASTM standard specifications for cranioplasty plates F452 – 76

a. Material for fabrication to be F 56 Grade2, F 75, or F 139, Grade 2.

b. Cranioplasty plates confirming to this specification shall be fabricated to accommodate without further alteration, various sized skull defects.

c. Shape shall be contoured so as to re-establish the normal configuration and symmetry of the skull at various anticipated sites of defect such as the parietal bosses, the inion, the brow, the linea temporalis and so forth.

d. Plates shall contain multiple perforations.

e. Thicknesses and individual shapes shall very with need.

f. Material used for fastening the plates shall be of the same alloy as the material used to make the specific plate installed.

Non metals

i. Polymers

The most commonly used polymer is PMMA which can be used in different ways such as: PMMA plain (self curing), PMMA reinforced and PMMA fabricated with CT scan data guided mold preparation (heat cured).

Lara, et al (1998) recommended the use of plain PMMA for small defects ($5cm^2$-$15cm^2$), the fiber reinforced type in medium sized defects (16 cm^1-49 cm^2), and the computer guided mold in large defects.

Tomancok, et al (1998) used carbon fiber reinforced plastic for cranial reconstruction and found reduced operative time was achieved along with better cosmetic results. The authors also found better post operative imaging as an advantage over other radiopaque materials.

Lewis, (1997) in his review of properties of bone cement identified several drawbacks in the use of bone cements. Firstly thermal necrosis of bone, impaired local circulation, and tendency for membrane formation at the cement bone interface was seen due to exothermic reaction of polymerization of the liquid monomer and powder polymer which can produce temperatures above 67 and 124^0C (Wang, et al 1995)**.** Secondly it was postulated that the residual monomer could also cause chemical necrosis (Kindt–Larsen 1995). The third drawback was found to be due to shrinkage of the cement during

polymerization. Stiffness difference between the bone and the cement was the fourth problem. The last problem was the cement particles interacting with the surrounding tissues causing an inflammatory response and increasing bone destruction. Aseptic loosening of the prosthesis was caused by interfacial failure, bond failure, bone remodeling and cement failure (Jasty et al 1991, Spector et al 1992).

ii. Bioceramics

Bioceramics used as craniofacial implant material are Hydroxyapatite (HA) and Calcium Phosphate (CAP).

Staffa et al (2007) fabricated stereolithography models for 25 patients requiring cranioplasty. The criterion for using ceramic implants were complex surfaces, extended surfaces greater than $25cm^2$, rejection of previous grafts or infection and bone flap resorption. A mean 30 months follow up showed no rejection or infection. However the limiting factors were found to be poor malleability of the material and the high cost of the fabrication of the stereolithography model.

To improve material performance Itokawa et al (2007) developed a new material by mixing HA (67%) and PMMA (33%) to be used for cranioplasty. The expectation was, the osteoconductivity of the HA and strength of PMMA would combine to make the new material a good candidate for cranial bone implants. In vivo studies in beagles were conducted to verify the osteoconductivity and biocompatibility. The authors found that one year after the operation, HA-PMMA composite with 40% porosity showed the osteoconductivity in the HA portion, as was seen in the surface of the composite and the bone. Minimal inflammatory response and no abnormal osteolysis were seen and hence it

was reported that biocompatibility was good. The authors also suggested further investigations to be done for use of the material as a cranioplasty material in humans.

Eufinger et al (2007) used three different polymers, poly-L-Lactide (PLLA), poly-DL Lactide (PDLLA), carbonated amorphous calcium phosphate (carbonated ACP), and calcium carbonate (calcite $CaCO_3$) in different layers resembling the human calvarial bone. The outer part consisted of PLLA+carbonated ACP a slow degrading material for mechanical strength of the implant and the inner part was made of PDLLA+$CaCO_3$ a faster degrading material for in growth of cells, vascularization, and bone formation. Using CT data individual implants were made by hot pressing and gas foaming. The implants were placed in bovine models and in eighteen months, resorption of the implant and new bone formation was evidenced. Further successful research of the above mentioned animal experiments using cranial implants fabricated with a combination of polymers and bioceramics could make the material to be of use in routine clinical procedures in the future.

2.4 Fabrication of Porous Titanium Parts for Biomedical Applications

The recent advent of metal RP technologies has led to research in using the technology for fabrication of porous parts with altered mechanical properties to suit the requirements of bone replacements. Parts with mechanical properties close to that of bone are being tried in orthopedic applications. Reducing mechanical properties as elastic modulus of implants helps in overcoming the stress shielding, which occurs due to differences in modulus of elasticity between the implant and the host tissue the bone. Also, it reduces the weight of the titanium implants, and enhances tissue in growth for increased stability

and longevity of the implant. Porous titanium implants also encourage osteoblastic growth for better fixation and integration with the anatomical part to which it is fixed. However, studies have not been done for applying the methodology to craniofacial applications. The function and load bearing requirements of craniofacial implants are very different from the orthopedic implants in a clinical scenario making it necessary to study the properties from the perspective of craniofacial applications.

Lopez-Heredia et al (2007) fabricated 800 and 1200 μm and an interconnected network were manufactured using rapid prototyping and implanted into 15 New Zealand White rabbits and found abundant bone growth after 3 and 8 weeks in both pore sizes of the implants.

A method of indirectly using RP processes as Stereolithography and FDM for fabrication of sacrificial parts/molds either with polymer or wax and investment using them as patterns or molds casting in titanium was used by some researchers (He et al 2006, Singare et al 2006). Casting of titanium and titanium alloys is a cumbersome process due to the high melting temperature and reactivity of the material. More over the porosity and pore morphology also cannot be controlled.

Processes capable of making metallic parts directly are fiber deposition, selective laser sintering (SLS) / selective laser melting (SLM), laser engineered net shaping (LENS) and electron beam melting (EBM).

2.4.1. 3D Fiber Deposition

Li et al (2002, 2005, 2006, and 2007) used slurry with titanium in a syringe and deposited 3D fibers in the form of a scaffold using the Bioplotter from EnvisionTech GmbH Germany. The method was similar to FDM, used for tissue engineering. The authors also

compared scaffolds fabricated by 3D fiber deposition and the ones, made by sponge replication (Sponge Ti) and found that although the macrostructure of the two materials were different, the microstructure was similar. Both scaffolds had an open pore structure, D3DP fiber showed a fairly regular open pore structure, and sponge titanium exhibited an irregular open pore structure that resembled cancellous bone. The elastic modulus of titanium scaffold were found to be higher than that of cancellous bone but the permeability of both titanium scaffolds were comparable to cancellous bone. The compressive strength of the D3DP was higher than that of sponge replication since the D3DP had a constant fiber diameter. Permeability of the sponge Ti was comparable to that of cancellous bone. D3DP had a higher permeability due to the 0-90 lay down.

2.4.2. Selective Laser Sintering (SLS) / Selective Laser melting (SLM)

SLS and SLM are SFF techniques where a Laser Beam is used to sinter layer by layer metallic powder to form a solid part.

Hayashi et al (2005) used Nd: YAG laser beam to sinter a thin layer of titanium sheet powder. The authors studied the influence of laser scan spacing on tensile strength and porosity and average laser power on the bonding strength. The tensile strength decreased with increased scan spacing. A reduction in the line spacing meant more laser beam overlap area so that the energy input per unit area is increased. Increased energy input lead to increased size of the titanium particles during the sintering process resulting increased strength of the parts. Maximum tensile strength of 36MPa was obtained at a scan spacing of 0.15mm and the maximum Young's modulus of 1.66GPa was obtained at a scan spacing of 0.2 mm. A maximum porosity of 40% was seen with a scan spacing of 0.1mm, the tensile strength was 35MPa but the Young's modulus was only 1.07GPa. The

authors recommended a scan spacing of .2mm for a spot size of .35 mm for parts that require high strength and high porosity. To improve the strength, influence of laser power on the bonding strength between the layers was studied and an average power of 15W and pulse width of 2.2 ms was recommended. The authors found that optimum pore sizes of 200µm were obtained in the average power region between 12 and 16W as seen in Figure 2.1. This demonstrates that melt width and melt height is dependent on the energy supplied apart from material properties. Optimum sintering parameters for producing porous parts with bending strength of 63MPa, Young's modulus of 1.5 GPa in the direction of lamination and 79MPa and 1.8GPa in the direction vertical to the lamination respectively was a pulse frequency of 80Hz, pulse width of 2.2ms, pulse energy 189mJ, peak power of 85.0W, beam spot size of 350µm, scan spacing of 0.2mm and scan speed of 3.3mm/s. The strength of the material requires to be improved as the Young's modulus of bone is 1-20GPa. The pores are also not interconnected and further research will have to be done to fabricate parts with improved mechanical properties and interconnected pores.

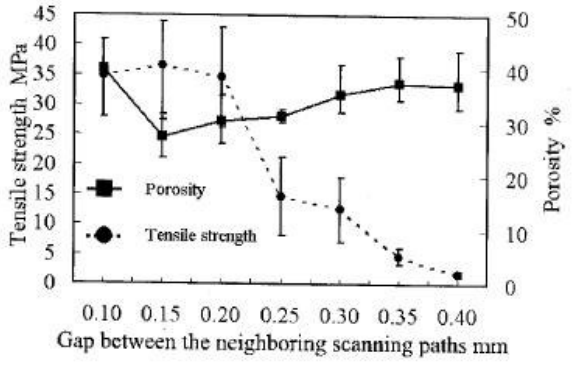


Figure 2. 1 Effect of scan spacing on tensile strength

Vaucher et al (2003) used SLS for fabrication of dental implants using aluminum and titanium composites. Parts of titanium samples were manufactured with a pulsed laser.

The authors found that at low laser power (25-40W), the porosity was finely dispersed and at high power 60-100W dense parts were formed.

Properties of titanium implant models made by CW ND:YAG Laser and pulsed ND YAG Laser processing was studied by Laoui et al (2004). The authors reported that peak power had high influence on tensile and fatigue strengths. The higher the peak power, the higher the melting depth and better bonding between layers as seen in Figure 2.2. The fatigue strength of the parts made with a hatching pitch of 0.4mm was greater than those made with a hatching pitch of 0.75mm due to the better metal bonding and higher density when the hatching pitch is smaller. The best parameters to produce parts with tensile strength 300MPa and torsion fatigue strength 100MPa (comparable to wrought titanium) were found to be: scan speed 6mm/s, laser peak power 1KW and hatching pitch of 0.4mm.

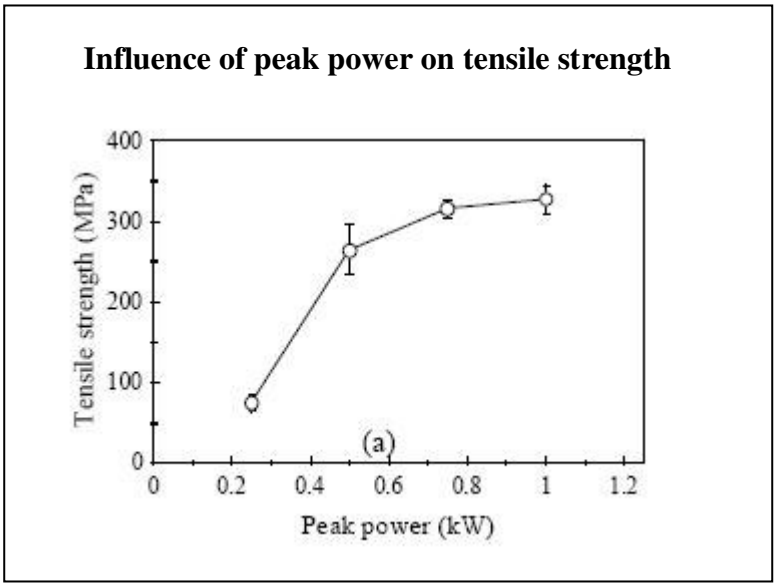


Figure 2. 2 Influence of peak power on tensile strength

Binding mechanisms in selective laser sintering and selective laser melting has been studied by Kruth et al (2005). Solid state sintering- the binding occurred at temperatures between $T_{Melt} / 2$ and T_{Melt} and the main cause for the sintering was the lowering of free energy resulting in the particles growing together. Since the process is slow, preheating of the material was required to increase the diffusion rate of atoms and reach an acceptable laser scan velocity. Titanium powder was preheated using a low intensity laser light (100-300W/cm^2) for 5secs. The degree of sintering was low as the temperature reached and stayed below α / β transition temperature (890^{0}C). Above this temperature, the sintering degree was increased due to the high self-diffusion coefficient of the β-phase compared to the α phase. Full melting binding was also studied for the fabrication of dense parts with mechanical properties equal to that of bulk materials. The process parameters required to be varied depending on the properties of the materials as laser absorption, surface tension and viscosity of the material to avoid sphereodization of the liquid melt pool – balling.

2.4.3. Laser Engineered Net Shaping (LENS)

Griffith et al (2000) described LENS as a process similar other rapid prototyping systems capable of producing metal parts directly from CAD data. The uniqueness of the process is that fully functional dense parts similar to wrought metals can be produced in a short time, thereby reducing manufacturing costs. The process had the potential to manipulate the material properties through precision deposition of the material, which includes thermal behavior control, layered or graded deposition of multi-materials, and process parameter selection. Microstructure and properties of components fabricated by LENS were studied, and the effect of many-layered interfaces on the mechanical properties was

also studied. Two stainless steel alloys, SS316V,H and SS316L V,H and IN 690 V,H were studied. The stainless steel alloys showed lower strength in the vertical direction, probably due to stress state, as the layers are perpendicular to the pull direction, and fracture initiation occurred at the layer interface. However, no defects were seen at the layer interface as a cause of this observation. Horizontal samples showed higher yield strength, but the ductility was less, and secondary cracks were seen forming at the interface, depicting weak microstructure at the interface.

Kummailil et al (2005) studied the effect of laser power, scan velocity, hatch spacing and powder mass flow rate on deposition. Hatch spacing ranged between 381 μm and 457 μm, and the laser power varied between 250W to 350W, though the upper limit of the laser power of the equipment was 1000W. The mass flow rate was varied between 38mg s^{-1} to 76.4 mg s^{-1}, and the scan velocity ranged between 16.9 mm s^{-1} and 27.5 mm s^{-1}. The authors found that the effect of mass flow rate and scan velocity had the highest effect on deposition. Deposition was 2.5 times less sensitive to changes in hatch spacing and 4.5 times sensitive to changes in laser power.

Lin et al (2007) fabricated topology optimized Ti-6Al-4V alloy lumbar interbody fusion cage using SLM. The experimental average compressive modulus of the cage was 2.97 $\pm$ 0.90 GPa, which was found to be half that of the FEA computed simulation values of 5.5 GPa. The stress strain curve, as seen in Figure 2.3, showed that the compressive moduli was consistent, showing that the fabrication process was capable of achieving parts with consistent mechanical properties. The designed pore sizes were 1000 μm, but in the fabricated part it was 700 μm. The rims of the pores were thickened to 150 μm**.** The authors used micro CT for characterization of the internal structure, and found that

the internal structures could be well-visualized, showing that though titanium alloys produce metal artifacts in magnetic resonance images, they give clearer pictures with micro-CT imaging, which could be a useful modality for post operative evaluation of implants and the structures inside. However, only one porosity of 52% was tested.

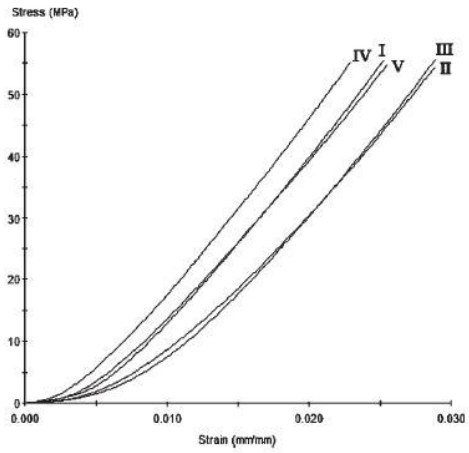


Figure 2. 3 Stress – strain curves of Ti-6Al-4V
5 optimized interbody fusion cages fabricated by SLM

Studies on SLS and LENS show that the quantity of power used for melting the powder has an influence on the height and width of the melt pool, which in turn affects the mechanical properties of the final part.

2.4.4 Electron Beam Melting

Electron-beam melting is a solid freeform fabrication method for creating solid/porous metal parts from a CAD file. Titanium powder is fully melted by scanning an electron beam, and cooled to make it solid. Solidification of multiple layers results in a solid part. The characteristics and mechanical properties of the built part depend on process parameters as scan velocity, power of the electron beam, layer thickness, build orientation, line width, and scan direction.

Harrysson et al (2003) used EBM technology initially to fabricate custom knee implants from a .STL file, generated from computer tomography data. Titanium powder was used as the material. Apart from the parameters mentioned in the previous paragraph, the authors opine that the process parameters are also geometry dependent. The authors produced the same part with investment casting and compared the processes. EBM process took 25 hours to make the part, while investment casting took 78 hours, clearly showing the time and cost advantage of EBM. However, it is also stated that process parameters for Ti and its alloys will have to be optimized, as it is different from that used for processing steel using EBM. Using the technology for fabrication of functionally graded parts with more porous outer segments, facilitating bone growth, and dense inner segments, for adequate strength, has been suggested.

Kalinyuk et al (2003) studied the microstructure, texture and mechanical properties of EBM melted titanium. Ingots with 200mm diameter and length of 1.5m (ingot1) and 400mm diameter and 2m length (ingot2) were melted using a YE-208 electron beam. Two EB guns were used for melting, and the molten metal was fed into a mold. The material was melted and remelted for homogeneity and dissolution of low-density inclusions. Chemical analysis showed that the alloying elements and impurities were uniformly distributed within the ingots. The microstructure was characterized by coarse β grains with α at the grain boundary in both the ingots. The thickness of α lamellar grains was 5-7.5 μ m in ingot 1, and 10-15 μ m in ingot 2. The yield strength and ultimate strength were 763-793 and 792-818 MPa for ingot 1 and 769-792 and 809-834 MPa for ingot 2 respectively, from the periphery to the center. The impact strength was very high in the range of 51-58 and 52-62 10^4 J m^{-2}.

Cormier et al (2004) experimented on optimization of the process in relation to surface quality and build speed by varying beam current from 5mA – 20mA and beam velocity from 1000mm/sec to 5000 mm/sec. Surface roughness of the fabricated part was 19.78 μ m(Ra). Experiments also suggested that complete densification of parts took place at scan speeds of 1000mm/sec to 1500mm/sec. It was also noted that the metallurgical bonding between layers was incomplete at 1500 mm/sec. Although the 2000-2500mm/sec specimens were only loosely bonded as per the SEM images, they could not be broken by hand.

To study the effect of process parameters on thin-walled plates fabricated using EBM, Cormier et al (2004) fabricated a bulky part and a thin-walled part. When heated, titanium undergoes allotropic transition from α Ti to β Ti. The authors observed that in thin-walled specimens the α-Ti needles were approximately 1/3 of the size produced in bulk parts. It was also observed that the contours were melted approximately at 25% of the speed of the fill area to improve surface finish. Experiments using recommended processing parameters showed that the refined microstructure was due to the effect of the geometry on the cooling rate of the part. Finer microstructure of thin-walled parts are preferred in fatigue applications where fracture toughness is important, as in bone plates. The authors opine that the columnar grains seen in the experiments could give rise to parts with tailored anisotropic properties.

H13 steel was fabricated in accordance to ASTM E8 standards by Cormier et al (2004) using EBM. The layer thickness was 0.1 mm. Each layer was preheated 10 times with a scan speed of 10,000 mm/sec, and the beam current was progressively increased from 2mA in the first scan to 20mA in the 10^{th} scan. The first set of two specimens were

removed and rapidly air-cooled. The second set was annealed in a furnace by heating to 900^0C, and then cooled at a rate of 22^0C/hr. The third set was slowly cooled to room temperature under vacuum. Micro structural analysis showed the structure was virtually 100% dense, and interlayer fusion was complete. Localized non homogeneities were observed at the boundary between the melted contours and the interior square regions.

Harrysson et al (2005) designed a Tibial Plateau Slope (TPS) correction plate for dogs. Two build orientations, one on the side, and one flat with the concave surface facing down, were chosen by the authors. Bending tests were performed as the plates were subjected to bending loads when implanted. Both plates showed very similar characteristics, but the plate built on the side showed higher ultimate strength. The surface texture of the bone plates was rough, and hence, further finishing was needed to prevent soft tissue ingrowth. Furthermore, the rough surface would provide plenty of micro crack initiation sites that would reduce the ultimate strength of the plate. A three point bending test of six plates with greater thickness showed that the ultimate strength directly correlated with the thickness. The thinner plates, were similar to the commercial plates whose modulus of elasticity and ultimate strength, were found to be 103-104 GPa and 950-1000MPa respectively. Using FEA, the modulus was calculated to be 116-122 GPa.

EBM has been used by Heinl et al (2007) to produce an interbody fusion cage, a lattice structure, by varying the line offset and altering the scan direction. The authors produced structures with porosities ranging from 60 % – 25 % with elastic moduli ranging from 1 GPa to 30 GPa, making fabrication of titanium structures with mechanical properties as close to that of human bone as possible.

Harrysson et al (2007), also used EBM for fabricating custom hip implants with titanium with defined mechanical properties. First, lattice structures with 6 mm, 8 mm, and 10 mm and 12mm cell sizes were tested. Compression tests showed that structures were stiffer in the Z direction than the XY direction. Elastic modulus in the XY and Z direction for 8mm, 10mm and 12 mm, when tested, was 60 MPa, 25 MPa, 12 MPa, 78.81 MPa, and 23.63 MPa respectively. Flexure testing showed the average modulus for 6 mm and 8 mm structures in the XY orientation were 349.5 MPa and 47 MPa respectively. As a second step, three types of hip implants with stems, that were solid, mesh, and with holes, were designed and fabricated. Mechanical properties of the three were tested. Weight of the stems after cleaning the powder was 46.72 g for the solid stem, 33.83 g for the stem with holes, and 26.19 g for the mesh stem.

2.5 Characterization of Microstructure of Titanium

Rack and Qazi (2006) observed three types of microstructures, lamellar, equiaxed, and bimodal, that can be produced in Ultra fine grain (UFG) titanium through control of solution annealing temperature, cooling rate and final aging temperature. The lamellar structure was formed by solution treatment above the β transus, followed by air cooling and aging between 700 and 800^0C. Solution annealing below the β transus between 800 and 925^0C produces equiaxed structures, and solution annealing below the β transus between 900 and 950^0C produces bimodal structures. The three structures have varying mechanical properties. The equiaxed micro structures had high strength and ductility and lower fracture toughness; the lamellar structures had better fracture toughness, but relatively lower strength and ductility. Fatigue strength was found to be highest with bimodal structures, followed by equiaxed structures, and the lamellar structure had the

lowest fatigue strength. The authors observed that plastic deformation of titanium also resulted in 20% increase in yield and ultimate tensile strength as against annealed material. The tensile elongation was found to be 10% more than required for biomedical applications. Additional enhancements could be achieved by Equal Channel Angular Pressing and upsetting. The ultra fine grain titanium processed as previously mentioned did not have much effect on dynamic frictional coefficient and steady state wear. Osteoblast growth was also found to be enhanced in UFG processed titanium. It is therefore found that UFG titanium has better mechanical and biological properties than the regular material.

2.6. Prediction of Mechanical Properties

2.6.1 Analytical /Numerical Methods.

Ashby and Gibson (1997) provide simple relationships between elastic modulus E and relative density

$$\rho_{rel} E \times \rho^{2}_{rel.}$$

This has been used by Heinl et al (2007) for arriving at the elastic modulus as a function of compressive yield strength.

Thelen et al (2004) compared the results of elastic moduli from experimental data from ultrasound experiments and uniaxial compression testing on microporous Ti. Analytical models were used to predict the elastic modulus, including "structural" approaches, and Ashby and Gibson's equation for finding relation between porosity and elastic modulus of 2D honeycomb

$$\frac{E^*}{E} = 2.3\left(\frac{\sqrt{3}}{2}(1-\Phi)\right)^3$$

and 3D open cell material

$$\frac{E^*}{E} = (1-\Phi)^2$$

Where E* = effective elastic modulus, E = Elastic modulus of the dense part and Φ = porosity of the part to be tested.

The authors also used a "composite material" approach (Mori and Tanaka 1973)

$$E_{eff} = \frac{E_m(1-\Phi)}{(1+\Phi)}$$

Where

E_{eff} = the effective elastic modulus of the porous part

E_m = modulus of the dense part and

Φ = porosity.

Finally, a two-dimensional finite element model, based on optical micrographs of the material, was used. Simulations were performed by varying conditions and levels of approximation. The results showed that simple analytical models could provide good estimates of the elastic properties of the porous titanium, and that the moduli can be significantly reduced to decrease the mismatch between solid titanium and bone. Finite element models did not consistently reproduce the experimental values for modulus, but showed that bone ingrowth dramatically reduces stress concentrations around the pores.

Kotan & Bor, (2007) used Ashby's formula, mentioned in a previous section, for prediction of effective elastic modulus for porous Ti, porous parts fabricated by space holder method, and found the theoretical values to be much higher than experimental

values. The authors attributed it to the fact that the model takes the metal part as a dense solid and no consideration is given for the microporosity of the porous part.

2.6.2 Finite Element Analysis

Image based FEA analysis has been used by Williams et al (2005) for prediction of elastic modulus. The authors used voxel based homogenization software VoXELCON (Quint Corp. Tokyo Japan). The mean experimental and predicted values varied from 52MPa – 67MPa and 46MPa – 68MPa respectively.

Harrysson et al (2007) also used FEA for predicting compressive modulus of titanium lattice structures fabricated using EBM, but found the predicted values were increased by a factor of 4 as seen in Figure 2.4. The authors however used FEA for determining the stresses at the end of the implant.

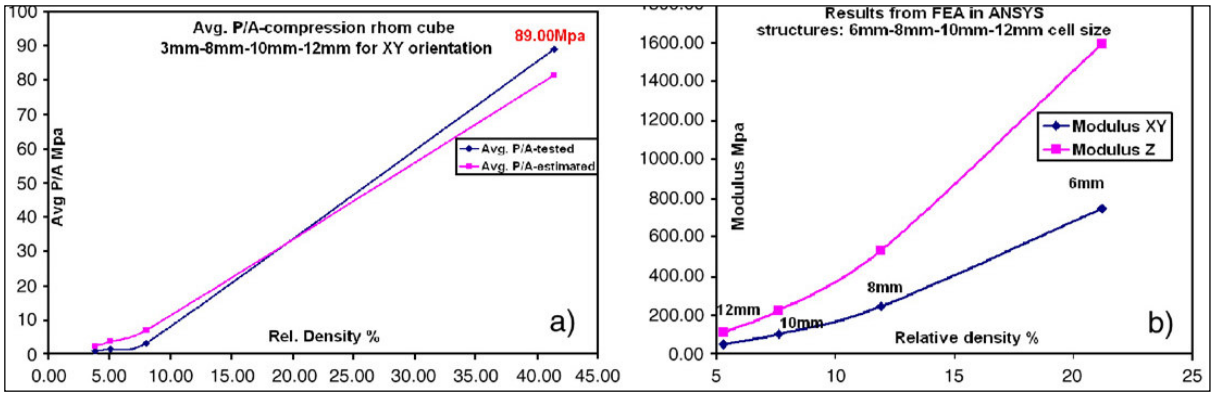


Figure 2. 4 a)Average compression strength versus relative density for tested and estimated mesh structures b) ANSYS simulated results for compression stiffness versus relative density in XY orientation and Z orientation.

2.7. Experimental Methods for Mechanical Properties

Thelen et al (2004) used ultrasonic method to determine the elastic moduli for several porous Ti specimens. A transducer transmitted a sinusoidal signal to the front surface of

the specimen and recorded the waves reflected by the opposite surface. Transducers of 2.5MHz, 5MHz, and 50 MHz were used. The elastic moduli and porosity were found to be inversely proportional. Despite the dramatic differences in microstructures the normalized moduli of the cp-Ti and Ti-6Al-4V samples followed a similar trend. The slightly lower moduli of the Ti-6Al-4V samples may be due to the shape of their pores. The pores of the cp-Ti foams were roughly spherical and smooth, the pores of the Ti-6Al-4V foam showed many cusp-like features. The authors compared these values with analytical values and found them to correlate with Ashby's (1997) and Mori and Tanaka's formulae discussed in the previous section.

Lin et al (2007) performed Axial compression tests to measure construct stiffness on porous titanium constructs with porosity of 54%, fabricated with selective laser melting. A 4.45 N preload was applied followed by a compressive test to failure at a crosshead speed of 1 mm/min (ASTM) D695-02a using a MTS Alliance RT30 electromechanical test frame (MTS Systems, MN). The compression test was continued, until the set break point of 20,462 N was met in the real-time compressive load-displacement curve, since the failure load of tested samples made of Ti-6Al-4V alloy was estimated beyond the maximum load of 22,261 N of the default load cell of the testing system that is mainly designated for the biological tissue testing. Load versus deflection was continuously monitored and recorded, and stress-strain curve was generated based on geometrical parameters of samples. Effective compressive moduli defined as the slope of the linear region at the stress-strain curve were then calculated by the system. To further characterize the ultimate compressive strength of the designed cage, the authors subjected two cages to more destructive loads at a rate of 0.25 mm/min until they reached

catastrophic failure using an Instron Floor Model Testing System (Instron, MA) with 150 kN loading capacity.

CHAPTER 3

3. IMAGE BASED MODELING OF PATIENT SPECIFIC CRANIOFACIAL IMPLANTS

3.1 Summary

This chapter discusses the processes involved in arriving at an appropriate design for porous implants. The first part describes the method of reconstruction of patient specific anatomy from CT scan data, defining the defect and designing of external geometry of the implant that would correct the defect using dedicated medical imaging software MIMICS^{TM}. The second part describes the process of defining the internal architecture to arrive at a porous implant with predicted mechanical properties close to that of native structures.

The methodology for image based modeling of a patient specific cranial implant used in this study is shown in Figure.3.1.

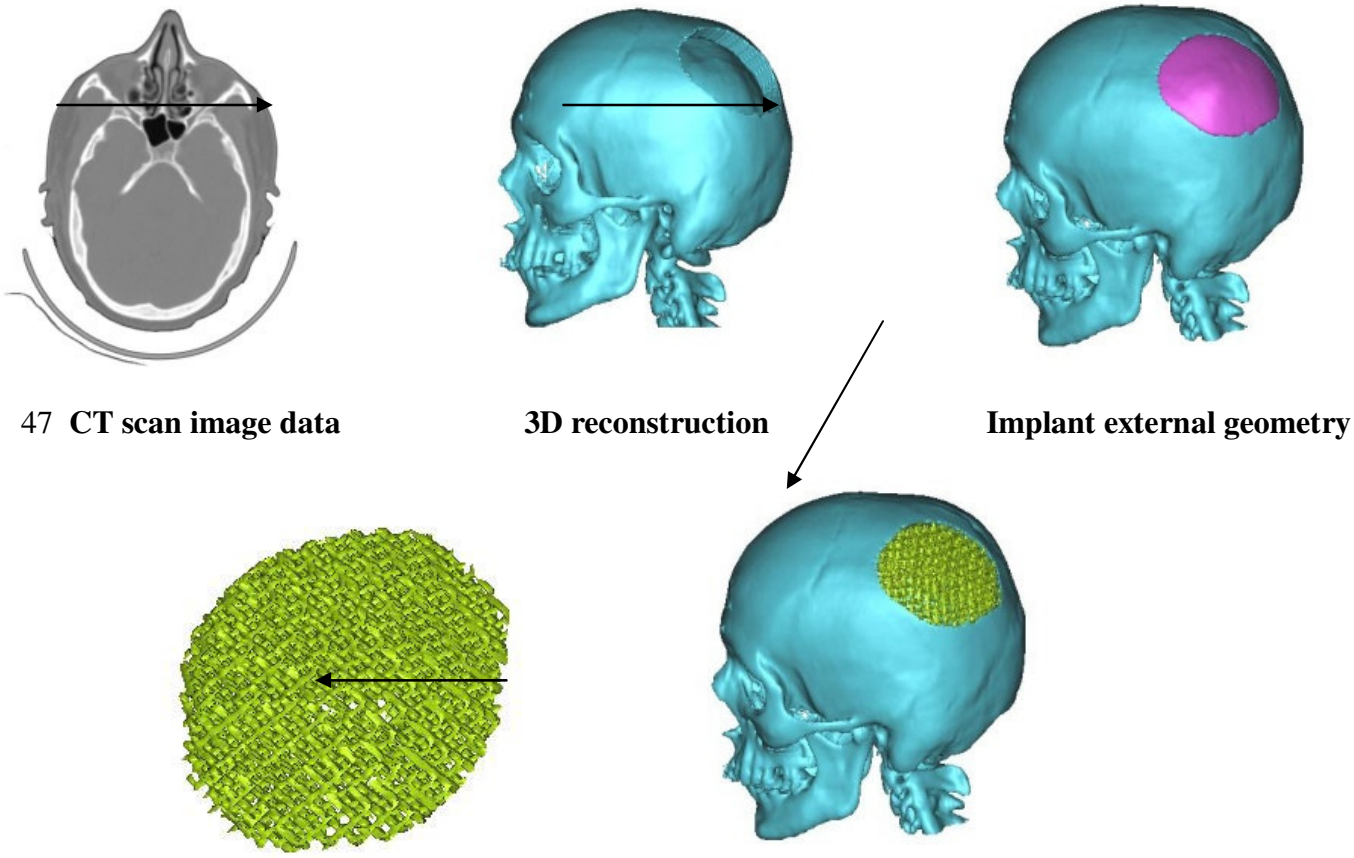


Figure 3. 1 Sequence of processes in creating patient specific porous cranial implants

The general methodology followed in design and fabrication of the porous implants is shown in figure 3.2.

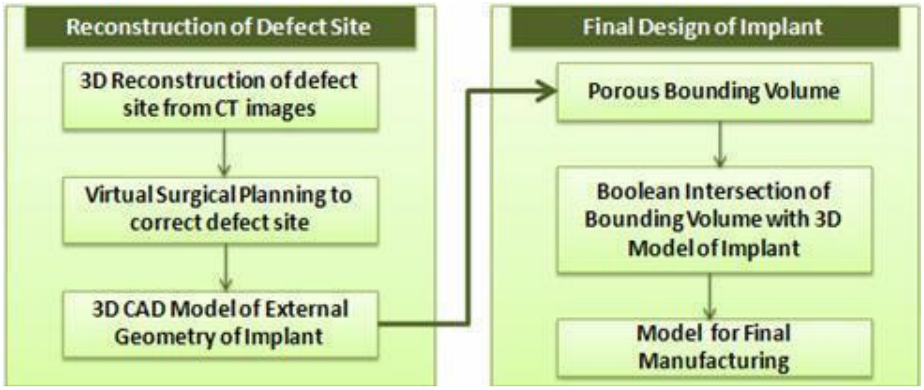


Figure 3. 2 Roadmap for the design of mandibular implant from CT images

3.2 Reconstruction of External Geometry of the Porous Implant

Reconstruction of the external implant design is done in two steps.

3.2.1 3D Reconstruction of Region of Interest with the Defect from CT Scan Data

The process of 3D reconstruction from CT scan image data can be divided into data acquisition and data processing.

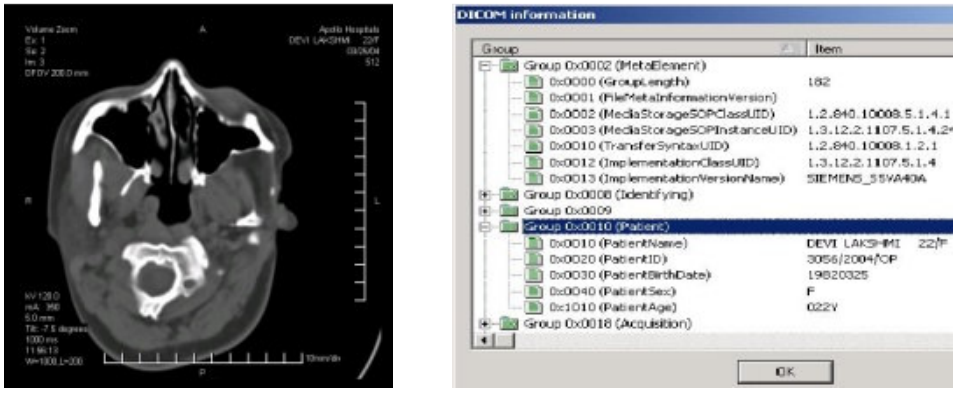
Data Acquisition

CT Scan Protocol

Slice image data from CT scans are used for the study. Images are taken with a gantry tilt of zero degrees and a slice thickness of 1.25 mm. The patient's head is fixed to prevent any movement during examination, and image data is collected 2 cm above and below the region of interest. The CT scan data is acquired on a compact disc in a DICOM compatible format. Figure.3.2a shows a typical DICOM file. DICOM - The Digital

Imaging and Communications in Medicine (DICOM) standard – IMAGES are image formats specified by the National Electrical Manufacturers Association (NEMA) for the distribution and viewing of medical images - CT scans, MRIs, and ultrasound. This standard describes a file format for the distribution of radiological images.

A single DICOM file contains a Header (which stores information about the patient's name, the type of scan, image dimensions, etc.) and image data, the 3D information, as shown in Figure.3.3a and b.



(a) (b)

Figure 3. 3 (a) CT scan image (b) DICOM file

Output Images from CT Scan

2D images are output in a matrix of 512 X 512 pixels and a gray scale of 16 bits per pixel on the screen. They are then transferred to a compact disc in DICOM, JPEG or PNG formats as a soft copy that could be directly imported into the medical image processing software for further processing. These images are processed using 3D medical modeling software - MIMICS™

Data processing

i. Software Used for Medical 3D Modeling and their Requirements

Advances in computer graphics and image processing have revolutionized medical imaging with the display of 3D objects being visualized at different angles and distances with varying colors, lighting and surface properties.

In this research, dedicated medical imaging software MIMICS^{TM} is used for processing CT scan images. Medical imaging software is capable of handling DICOM and other image formats, such as TIFF, JPEG, PNG, GIF, and BMP. Both gray scale and color images can be handled. The software is capable of working with CT, MRI, PET, microscopy data. 3D image processing, image registration for multi-modality application, image fusion, image resizing, and image reslicing are some important features of the software used in this research. Other essential features of the medical modeling software used are brightness contrast adjustment, thresholding / segmentation, region growing, rotation, scaling, reslicing, measurements, editing, examination of three dimensional volumetric data, assigning different object names for various tissues and capability of visualizing the objects either individually or together, visualizing internal structures by assigning transparency feature to the external objects. The software has capabilities of exporting the 3D digital object in a compatible format either to RP machines for model manufacturing or into CAD software for further analysis.

ii. 3D Reconstruction of External geometry Patient Specific Implants - MIMICS^{TM}

3D reconstruction of the region of interest of the patient specific anatomy from a CT scan is done in the following steps:

- Creation of an image data set

- Thresholding
- Region growing and 3D reconstruction
- Reconstruction of the implant's external geometry

Creation of Image Datasets

From the DICOM directory of files, a list is created with the relevant image slices pertaining to the pathology. Figure 3.4 shows the display of images in three orientations: axial, sagittal and coronal with a space to display the reconstructed 3D image. The images have a 512 X 512 pixel resolution.

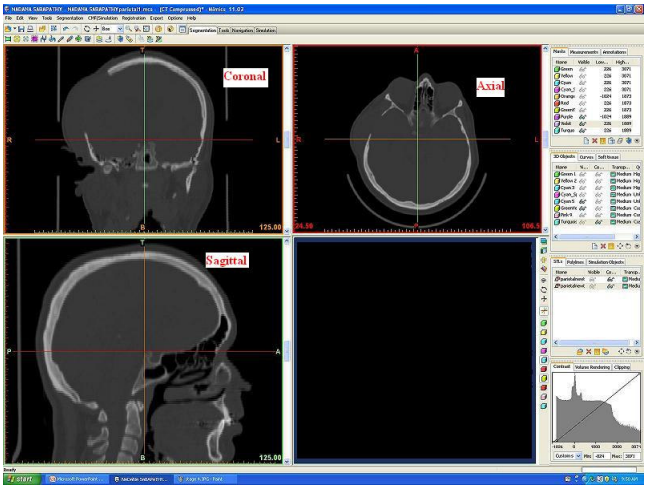


Figure 3.4 Image data orientation

Thresholding

For analysis of objects in an image, it is essential to distinguish between the objects of interest from "the rest." This latter group can also be referred to as the background. The techniques that are used to find the objects of interest are known as segmentation techniques - segmenting the foreground from background. Segmentation of CT 2D slice images is done by selecting specific image intensities (Hounsfield units) within the region

of interest. The use of CT numbers, or Hounsfield units, provides an indication of the nature of the tissues being imaged.

Thresholding is done by selecting the upper and lower threshold values of image intensities. Specific tissues such as bone, skin, and muscles are identified by their Hounsfield units. In a similar manner the pathological area is also delineated. The software displays all the pixels within the range of the specified intensity as shown in Figure 3.5.

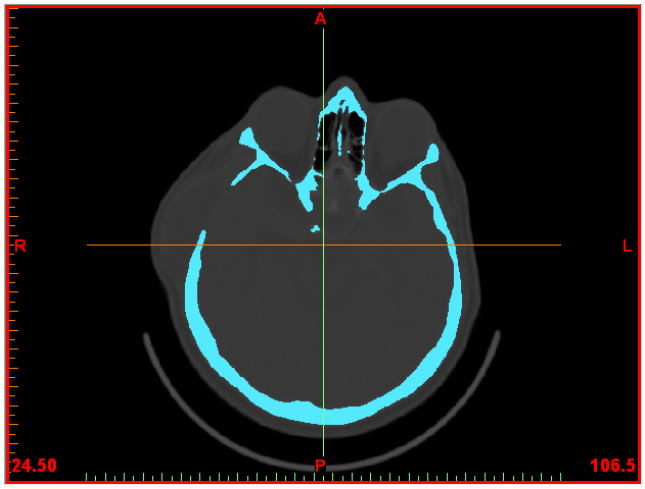


Figure 3. 5 Thresholding operation

Hounsfield units (HU) is a system to measure the attenuation coefficient of tissues in CT scan images. HU are also termed CT numbers. Bone has a higher Hounsfield value when compared to skin and soft tissues as it absorbs most of the radiation. Table 3.1 shows the Hounsfield values of some tissues that are commonly studied with CT images.

Table 3. 1 Hounsfield values of tissues

Tissue	CT number (HU)
Bone	1000
Liver	40-60
White matter (brain)	46
Grey matter (brain)	43
Blood	40
Muscle	10 - 40
Kidney	30
Cerebrospinal fluid	15
Water	0
Fat	50 to –100
Air	-1000

Region Growing and 3D reconstruction

Region growing is the process by which noise is minimized, and structures that are not connected in the image data are eliminated, resulting in a set of pixels that are connected within the same layer as well as with the upper and lower layers of data. By using the 3D reconstruction function, a 3D rendered model of the image data is generated. A skull with the defect rendered is seen in Figure 3.6.

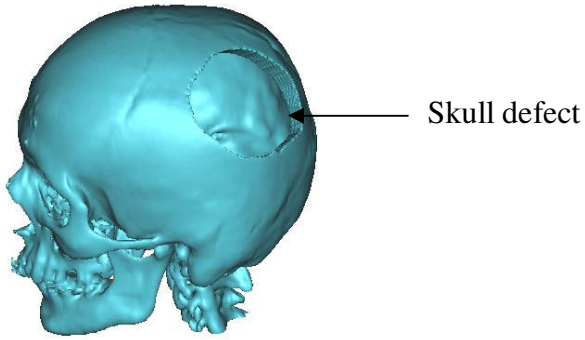


Figure 3. 6 Reconstructed skull model with defect

3.2.2. Reconstruction of the Implant's External Geometry

Using the above mentioned procedures, reconstructions were done for two clinical scenarios, namely a defect in the skull and a mandibular tumor.

Skull Defect

Since symmetry of the human body structure is a natural occurrence it is assumed that both the right and left sides are similar. The geometry of the cranial implant was determined by the shape of the outer and inner table of the cranial vault. The contact surfaces of the implant were decided by delineating the edge of the defect. Image data from the contralateral side was mirrored and the defect was closed. The external geometry of the resultant implant is seen in Figure 3.7a and b

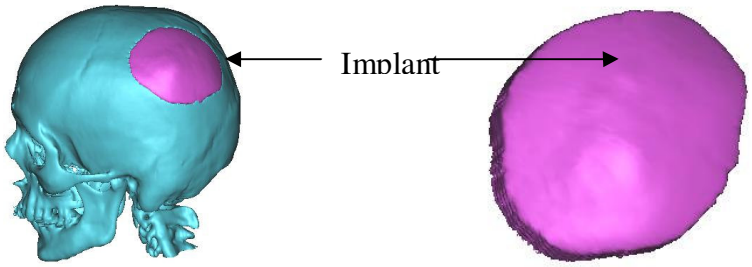
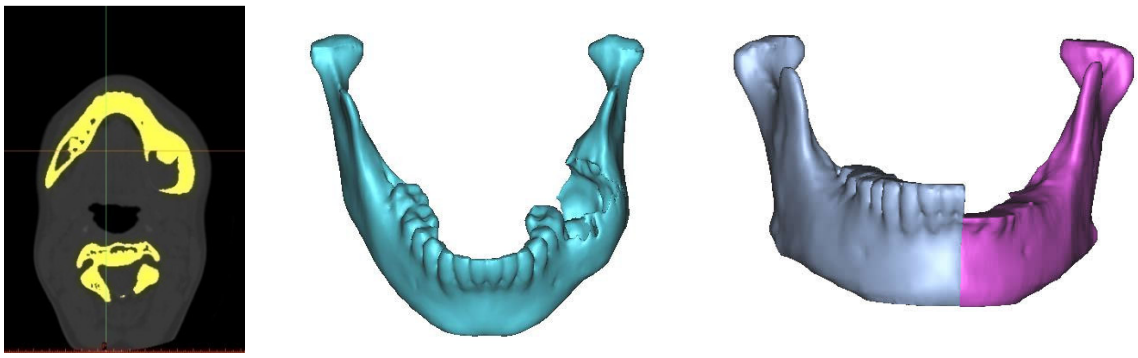


Figure 3. 7 (a) Skull with implant (b) Reconstructed implant external geometry

Prosthesis Planning for a Mandibular Tumor

A case with the mandibular (lower jaw) tumor extending only on the left side was chosen for reconstruction, as it is a common clinical finding requiring reconstruction. MIMICS™ medical imaging software is used to create the 3D models by performing thresholding and region growing operations as shown in Figure 3.8a and b. Surgical simulation of removing the left half of the mandible was performed, and image data from the right side was mirrored for deriving the external shape of the patient specific implant. The external

geometry of the mandibular implant was determined by the outer and inner surfaces and the contact regions of the proximal and distal ends of the tumor resected region. A final rendered virtual model of the patient's reconstructed mandible is shown in Figure 3.8c.



(a) **(b)** **(c)**

Figure 3. 8 (a) Thresholding operation; (b) Reconstructed mandible with defect; (c) Virtual surgical simulation and reconstruction of external geometry of the implant.

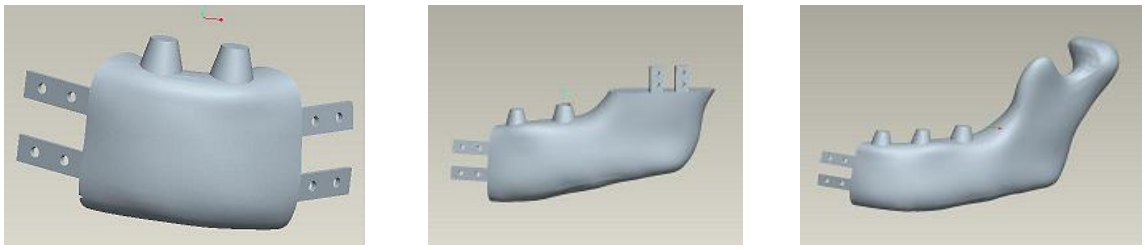
The implants thus designed were exported as .STL files from MIMICS^{TM} and the internal architecture was designed using CAD software Pro Engineer (PTC). .STL is a simple tessellated format of a solid model that can be sliced by the internal software of RP machines to create slice data for material deposition. The .STL file consists of triangular facets that are approximated to the geometric shape of the model. The data contained in the .STL file are the coordinates of the triangle and the facet normal. There are two .STL formats, the ASCII and binary. ASCII is the readable format but has a larger file size than the binary. Retention structures and dental implant abutments were designed in the mandibular implant to arrive at the final external geometry of the implant.

Virtual reality has played an important part in surgical simulation, as the digital model can be cut, repositioned and tried until satisfactory results of the post-operative outcome are reached. Surgical simulation for three common clinical scenarios is considered here:

Model 1 – anterior canine-to-canine resection – Model 2 – premolar-to-subcondylar resection – and Model 3 - hemi mandibulectomy – were conceived. Image data from the contralateral side is mirrored for deriving the external shape of the corrected site as shown in Figure 4. The corrected model would then form the external shape of the metallic implant. All the models are converted to a usable digital format (.iges) file type using the method described by Starly et al (2005).

3.2.3 Dental Abutments and Retention Structures

Retention structures in the form of plates are required for fixing the implant to the normal mandible. Dental implant abutments are also designed to enable the implants to be used in a clinical scenario over which fixed prosthodontic restorations can be fixed. The retention structures are 15 mm in length, 5mm wide and 1mm thick and have two 2mm diameter holes placed 3mm from the edge to fix osteosynthesis screws. Three implant abutments are designed as per specifications from Bicon™ (www.Bicon.com). All implants are 6mm in height and have a taper of 15° between the top and bottom surfaces. The implants with diameters of 3.5, 5.00 and 6.00 mm are placed in the anterior, premolar and molar regions respectively. The three implants with the fixtures are seen in Figures 3.9 a, 5b and 5c.



(a) **(b)** **(c)**

Figure 3. 9 (a): Canine to canine reconstruction - Model 1; (b): Premolar to sub-condylar reconstruction - Model 2; (c): Hemi mandible reconstruction -Model 3

3.2.4. Estimation of Mechanical Properties of Bone and Solid Titanium Implant

The estimated volume and corresponding weight of the corrected site model of the skull (Figure 3.7 b) and mandible implant (Figure 3.9 c) with two different materials are shown in Table 3.2. The volume of the models of the skull and mandible implants as estimated by the software is given to be 54640 mm^3 and 60626 mm^3 respectively. If the corrected models were to be built of solid titanium alloy, it would be 2.2 times heavier than the original bone it would to replace. More importantly, the elastic modulus of titanium alloy is about 114GPa while that of cortical bone at max would be 20GPa. This relative difference in stiffness results in significant stress-shielding effects. Therefore, it is imperative to build in two design criteria in the new implant – 1) Reduce the weight of the implant to be brought close to that of the natural bone and 2) reduce the effective stiffness of the material while still having titanium alloy as the primary choice of the implant biomaterial. Both of the above two criteria can be met by building in porous structures within the mandible structure.

Table 3. 2 Estimated weight of the implant

Type of implant	Material	Density ($g/cm^{3)}$	Volume (mm^3)	Estimated weight (g)
Cranial	Bone	2	54640	109.28
Cranial	Titanium	4.43	54640	241.50
Mandible (Model 3)	Bone	2	60626	121.25
Mandible	Titanium	4.43	60626	268.57

3.3 Design of Internal Architecture of the Porous Implant

Some essential considerations while designing porous implants are – 1) pore sizes to allow for the in-growth of new bone; 2) final implant weight and mechanical properties to be close to that of surrounding bone tissue to prevent stress shielding; 3) implant manufacturability and repeatability. The porous implant apart from providing structural support would also have to function in unison with the host tissue as an integral part of the anatomy and cater to functional requirements as mastication in the case of the mandible. To reduce the weight of the titanium alloy implant, a pattern of series of square holes were propagated throughout the interior volume of the implant. The controlled patterning of the holes would reduce the weight, reduce the effective Young's modulus (effective stiffness) and provide a network of pores for the in-growth of healthy bone tissue. Steps in creating the porous implant are described hereunder.

3.3.1 Design of Porous Implants

Design of porous implants was done in the following steps:

i. Creating the Bounding Volume (PRO Engineer)

The .iges model was imported into Pro Engineer^{TM} and a bounding volume was created. The bounding volume part so created enclosed the complete external geometry of the implant created using MIMICS^{TM} as shown in Figure 3.10.

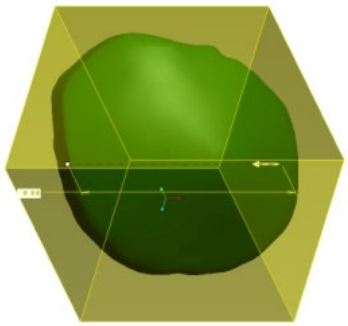


Figure 3. 10 Creating the bounding volume for external implant geometry – cranial implant

ii. Designing of Pores in the Bounding Volume part (PRO Engineer)

To achieve an internal porous architecture, a square bounding volume cube was created containing square pores, each measuring 1.5mm by 1.5mm propagated throughout the bounding volume in the XY, XZ and YZ planes as shown in Figure 3.11

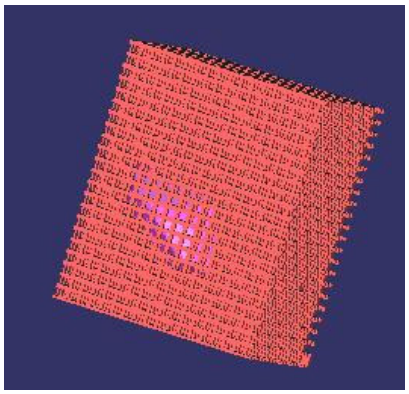
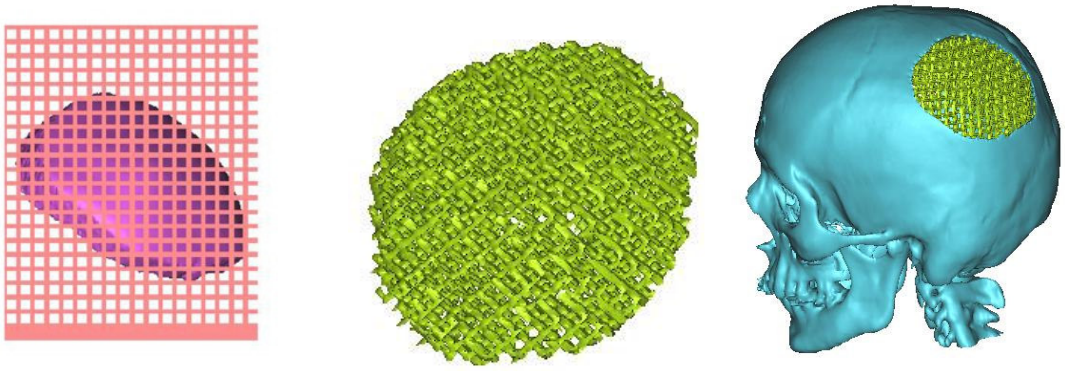


Figure 3. 11 Porous part enclosing the implant created in Pro Engineer™

iii. Creating the Porous Implant (MIMICS™)

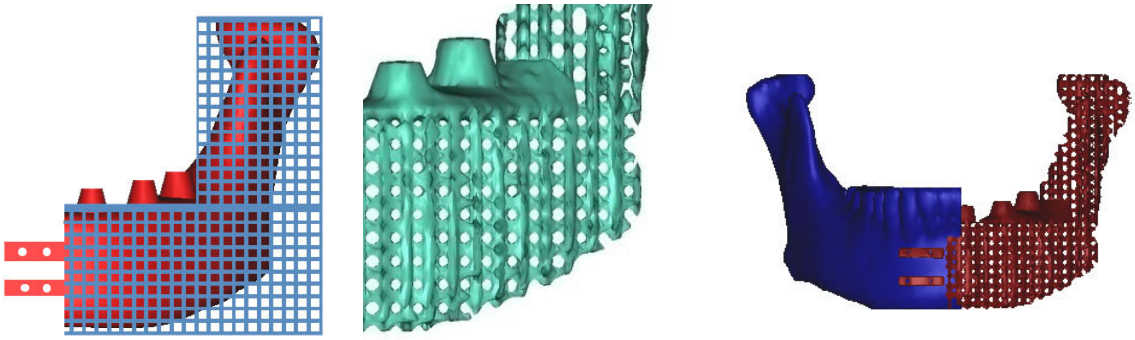
The porous part so created is imported into MIMICS™ as a .STL file. Using the boolean operation functions of MIMICS™, the original external shape of the implants (Figures 3.7 b and 3.9c) and the porous volume data is intersected. (Figures 3.12 a and 3.13 a).

The resultant porous models of the cranial implant is seen in Figures 3.12 b and 3.13 b respectively. The final porous model is matched with the skull and the healthy right side mandible of the patient (Figures 3.12 c and 3.13 c).



(a) **(b)** **(c)**

Figure 3. 12 (a) Bounding porous cube intersected with the implant (b) Resultant porous implant after the boolean operation with interconnected pores (c) Porous cranial implant fitted to the skull



(a) **(b)** **(c)**

Figure 3. 13 (a) Bounding porous cube intersected with the implant (b) Resultant porous implant after the boolean operation with interconnected pores (c) Porous mandibular implant fitted to the right normal mandible

The resultant porous implant will have an equivalent porosity given by equation 1 below. The weight of the porous implant can also be calculated given the density of the titanium alloy. The porosity (P) equation is given as:

$$P = \frac{V_1 - V_2}{V_1} \qquad \text{Eq (1)}$$

Where V_1= volume of the solid implant and V_2= volume of the final porous implant. The dimensions of the pore were also varied to obtain different weight characteristics. In the next chapter, the influence of pore dimensions on the effective stiffness of the implant will be described.

CHAPTER 4

4. PREDICTION OF EFFECTIVE MECHANICAL PROPERTIES

4.1 Summary

The design of the porous scaffold requires not only providing structural support but also functioning in unison with the host tissue as an integral part of the organ. Therefore, the effective mechanical properties of the implant have to be estimated prior to fabrication. Some of the common methods that have been used for predicting the mechanical properties of implants are Finite Element Analysis, Numerical methods, and Experimental methods.

The long term successful retention and function of the porous titanium implant depends not only on the implant providing structural support, but also biofunctionality of the prosthesis. Biofunctionality is defined as the mechanical and physical properties that enable the implant to perform its functioning in unison with the host tissue. In this context, this function would be to behave as an integral part of the mandible taking part in masticatory functions generating and transferring stresses to the adjoining bone. This is essential for maintaining the natural balance between bone apposition and resorption process. High stresses may lead to bone resorption and ultimate failure while low stresses at the bone implant interface could lead to stress shielding, leading to aseptic loosening due to failure of bone apposition.

4.2 Prediction of Effective Elastic Modulus

4.2.1 Empirical Method of Estimation of Effective E

Effective elastic modulus was also calculated for porosity values from 0 – 95 % using Ashby's and Gibson's formula:

$$E_{eff} = E (q_{rel})^2 \qquad \text{Eq (2)}$$

Where, E = Elastic modulus of the solid structure, q_{rel} = relative density of the cellular structure, E_{eff}= Elastic modulus of the cellular structure. Effective elastic modulus of the cellular titanium for porosity ranges from 0 – 95 % were calculated.

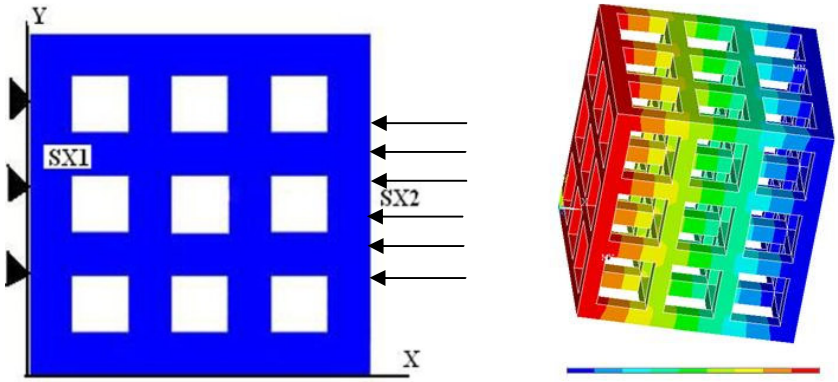
4.2.2 Finite Element Analysis

Mesh Based Method

Recently FEA techniques have been utilized in the biomedical engineering context, for analyzing parts of human body using realistic biomechanical data for the relevant tissues and alloplastic materials that are used for prosthesis fabrication. FEA has been used by Knoll et al (2006) and Tie et al (2006) effectively to study the stresses and biomechanical effects in mandibular reconstruction. Anup, et al (2007) used FEA for studying the effect of low velocity impact on skull bones. Therefore the effective mechanical properties of the implant and performance of the patient specific implant were estimated using FEA.

The geometrical complexity of the porous implant (Figure 3.13c) makes it computationally intensive and cumbersome for the discretization procedure during the mesh definition stage of the FEA analysis. To avoid this potential bottleneck, we have utilized the Representative Volume Element (RVE) method described by Hollister et al (2005), Starly et al (2006) and Fang et al (2005, 2006). In this homogenization method, an RVE is selected to represent the porous structure of the implant, and the effective

Young's modulus of the porous RVE is then calculated. Once the effective Young's modulus is determined for a range of porosity values, this value can then be the material input into the FEA analysis for assessing the performance of the implant.



(a) (b)

Figure 4. 1 a) RVE with applied boundary conditions
b) FEA contour plot for stress distribution within the RVE

The selected RVE for our implant is the square pore holes as shown in Figure 4.1a. The square pore is constrained at one face while a strain of 0.1% is applied at the opposite face. Periodic boundary conditions were assumed at all other faces. The RVE was meshed using 4 node tetrahedral elements. An FEA program, ANSYS™ (ANSYS Inc.), is used to predict the effective stiffness of the porous structure. The effective stiffness can be calculated by using equation 3 as follows:

$$E_{XX} = \frac{\sigma_X}{\varepsilon_X} = \frac{(\frac{R_X}{A_{SX1}})}{(\frac{U_X}{L_X})} = \frac{R_X}{0.001 * A_x} \qquad \text{Eq (3)}$$

Where A_x is the area of cross section of the face S_{x1} and R_x is the average reaction force on the surface S_{x1}. Since the unit cell is symmetric in the x, y and z directions, we obtain $E_{xx} = E_{yy} = E_{zz} = E_{effective}$. The prediction of effective stiffness was performed for a range

of RVE porosities ranging from 28.18% to 78.4%. Table 4.1 shows the volume of pores, pore size and the respective porosity % and elements and nodes of the RVE used in this study.

Table 4. 1 Pore size, Pore volume and porosity % for 60 mm cube

S.No	Pore size (mm)	Pore volume (mm^3)	Nodes	Elements	Porosity %
1	7	60858	46823	28211	28.18
2	10	108000	39131	22034	50.00
3	11	124146	36049	19841	57.48
4	12	139968	44177	24101	64.80
5	13	155142	50303	26839	71.83
6	14	169344	60363	32528	78.40

Beam Elements Based Method

Since the cuboid represented a beam structure a second method using beam elements was used to predict the mechanical properties of the representative volume element. The cross section of the beam was the square of the strut size and four elements were created in the X, Y and Z directions, generating a model 3mm X 3mm X 3 mm for pore sizes from 500 to 800µm and 6mm X 6mm X 6mm for pore sizes from 1000 – 1500 µm. The beam model so generated is seen in Figure 4.2.

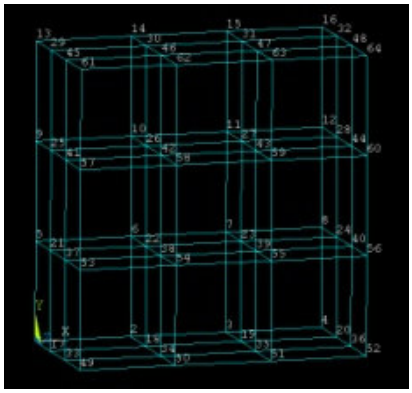


Figure 4. 2 Beam elements model

Table 4.2 shows the characteristics of the models generated with beam elements.

Table 4. 2 Characteristics of the beam element model

S.No	Size of the cuboid (mm)	Pore size (um)	Strut size (mm)	Beam cross section (mm2)	Porosity %
1	3	500	0.375	0.140625	50
2	3	600	0.3	0.09	64.81
3	3	700	0.225	0.050625	78.4
4	3	800	0.15	0.0225	89.6
5	6	1000	0.75	0.5625	50
6	6	1100	0.675	0.455625	57.48
7	6	1200	0.6	0.36	64.66
8	6	1400	0.45	0.2025	78.4
9	6	1500	0.3	0.09	84.38

4.3 FEA Based Analysis of Mandibular Implants in Response to Masticatory Forces

Apart from precise fitting and integration, the mandibular implants would require functioning in unison with the rest of the mandible during mastication. The three implant design models 1, 2 and 3 (Figures 3.9 a, b and c) described earlier were imported into Pro-Mechanica™ (PTC Corp., Massachusetts) and finite element method was used to predict the stresses and strains generated in the implant during mastication. A p-mesh was generated and the three anterior, premolar to subcondylar and hemi mandible implants had 722, 777 and 1475 tetrahedral nodes respectively.

The material properties assumed in this study are shown in Table 4.3. The Young's modulus and the assumed Poisson's ratio for the three different material types are shown. Cortical bone is assumed to be at 20GPa, while dense Titanium alloy at 114GPa. We

have considered different Young's modulus values for the porous titanium structure ranging from 3GPa to 114GPa corresponding to porosities ranging from 0% to 80%.

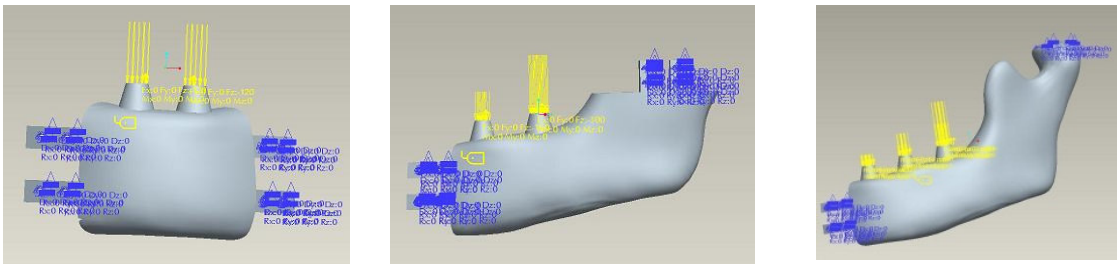
Table 4. 3 Material properties

Material	Elastic modulus(GPa)	Poisson's Ratio
Mandible – Cortical bone	20	.33
Titanium (Dense)	114	.32
Porous titanium alloy implants	3 (83.6 %),5 (80.6 %),10 (73.2%), 15(66.4%),20(60.2%),30(49.3),114 (0)	.32

All loads were vertical and compressive. Table 4.4 shows the loads applied on the dental implant abutments and were as used by Wang et al (2005). Loads were applied on the two implant abutments for models 1 and 2 as per the Table 4.4 as shown in Figure 4.4 (a) and (b). Since model 3 was a hemi mandible reconstruction, three load patterns were assumed - 1) Incisor loading, 2) Premolar and molar loading, and 3) Incisor, premolar and molar loading as seen in Figure 4.4 (c). The loads were applied on the implant abutments and with constraints applied in the X, Y and Z directions on all holes provided for fitting of osteosynthesis screws. Additionally in model 3 constraints were applied on the condylar region of the mandible. Von Mises stresses, displacement and strains generated in the implants were determined to evaluate the performance of the implants under masticatory loads.

Table 4. 4 Loads applied on dental implant abutments

Incisor	Premolar	Molar
60	150	300



a b c

Figure 4. 3 Loads and constraints on mandibular models 1, 2 and 3

4.4 Results

4.4.1 Effective Young's Modulus of Porous RVE

A relationship between porosity and effective elastic modulus of the constructs is first arrived at and the values are used to predict the properties of the patient specific implants.

Empirical Method of Estimation of Effective E

Effective elastic modulus of the cellular titanium as calculated using the Ashby's and Gibson's formula using equation 2 for porosity ranges from 0 – 95 % are seen in Table 4.5

Table 4. 5 Elastic modulus prediction using Gibson and Ashby's formula

S.No	Porosity%	Elastic modulus
1	0	114
2	5	102.89
3	10	92.34
4	15	82.37
5	20	72.96
6	25	64.13
7	30	55.86
8	35	48.17
9	40	41.04
10	45	34.49
11	50	28.5
12	55	23.09
13	60	18.24
14	65	13.97
15	70	10.26
16	75	7.13
17	80	4.56
18	85	2.57
19	90	1.14
20	95	0.29

FEA Based Method

For the FEA method the stress-strain values at the constrained nodes are plotted and the effective elastic modulus is estimated from the slope of the stress-strain curve of the porous constructs. As expected, the effective stiffness of the porous RVE (Ti alloy) gradually reduced with increasing porosity values. However, for all useful applications, typically porosity values ranging from 55% to 85% are selected which gives a corresponding effective stiffness to range from 24.7 – 3.2GPa. Table 4.6 shows the effective elastic modulus calculated using finite element method.

Table 4. 6 Elastic modulus prediction using FEA method

S.No	Beam elements		Mesh	
	Porosity %	Predicted E(GPa)	Porosity %	Predicted E(GPa)
1	50.00	30.31	28.18	63.68
2	57.48	25.43	50.00	30.01
3	64.66	19.07	57.48	22.56
4	78.40	9.53	64.80	14.26
5	84.38	6.06	71.83	11.39
6	89.60	3.81	78.40	7.92

Using Figure 4.4, it is seen that a 60% porous Ti alloy should have an effective Young's modulus of about 19.51GPa.

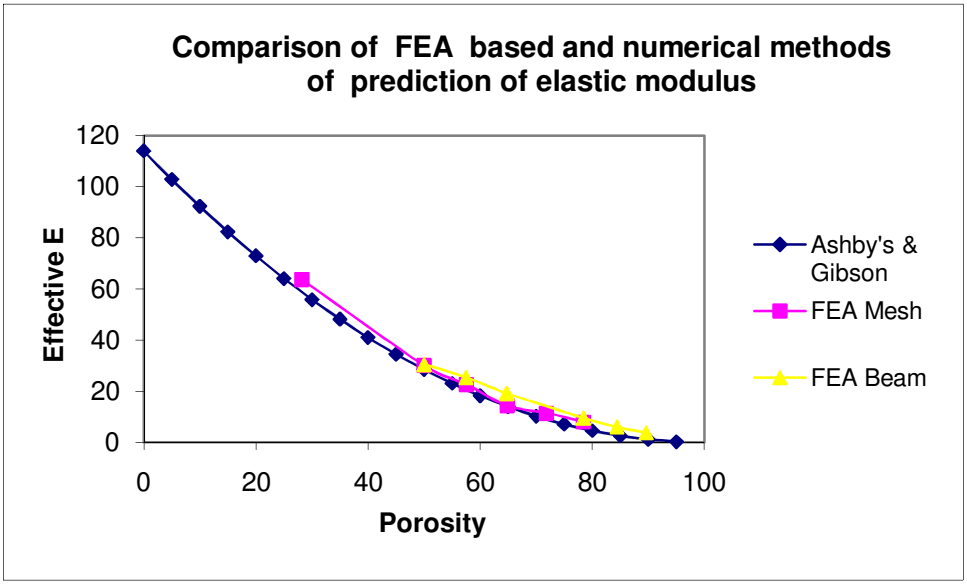
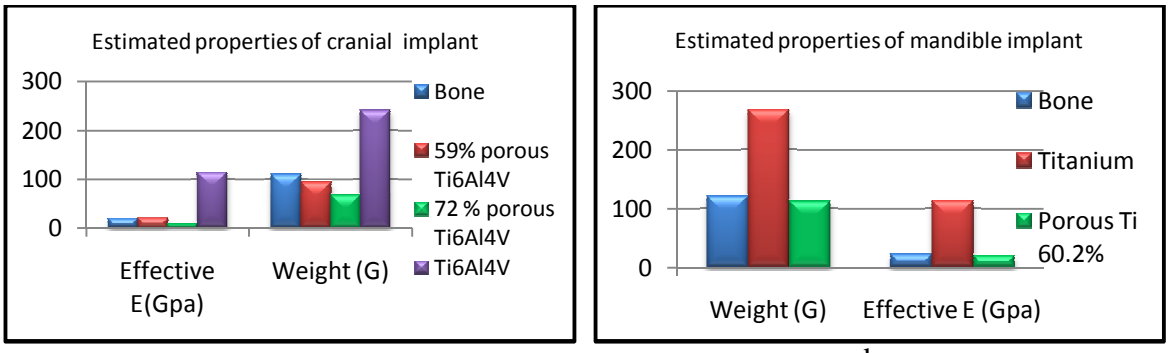


Figure 4. 4 Effective elastic modulus predicted by FEA and method

4.4.2 Estimation of Properties of Patient Specific Implants

If a 58.59 % and 60.2% porous structure is incorporated into the cranial model (Figure 3.12 b) and mandible Model 3 (Figure 3.13 c), then final properties such as weight and effective volume can be estimated. A comparison of the properties of the solid titanium, porous titanium and a bone model of the cranial and mandibular implant is displayed in

Figure 4.5 a and b respectively. Notice that a porosity value of 60% is selected so as to match the weight characteristics of natural healthy bone. Also, the effective stiffness of the implant would match that of the cortical bone. Estimated properties of the cranial and mandible implant model is shown in Table 4.7



a b

Figure 4. 5 Comparison of the properties of the solid and porous titanium implants, and its bone equivalent (a) cranial implant (b) mandible implant (Model3)

Table 4. 7 Estimated properties of patient specific cranial and mandibular implants

Type of implant	Material	Volume (mm^3)	Porosity %	Estimated weight (g)	Effective E (GPa)
Cranial	Bone	54640		109.28	20
Cranial	Titanium	54640	0	241.50	114
Cranial	Titanium	15386	71.84	68.01	9.59
Cranial	Titanium	22426	58.59	94.19	20.5
Mandible (Model 3)	Bone	60626		121.25	22.8
Mandible	Titanium	60626	0	268.57	114
Mandible	Titanium	25517	60.20	113.04	19.86

4.4.3 Performance of Patient Specific Mandibular Implants 1, 2 and 3 in Response to Masticatory Stresses

Von Mises stress is commonly used to study the stress measurements in mandible reconstruction (Cox et al 2003, Fernandez et al 2003, Knoll et al 2006 and Lovald et al 2006). In this study, Von Mises stresses generated during masticatory vertical compressive stresses are studied to arrive at an acceptable porosity of the implant to function well in a clinical scenario.

Model 1 Canine to canine Reconstruction: Maximum Von Mises stresses of 56.94MPa is seen to be in the region of the first set of screws on the retention structures bilaterally as seen in Figure 4.6.

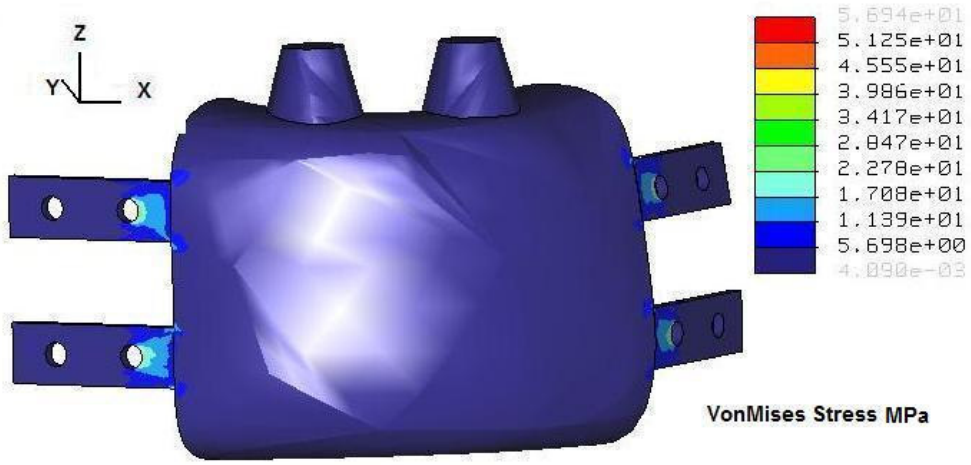


Figure 4. 6 Model 1 Von Mises stresses under masticatory load

Maximum principal strain is seen in the region of the first set of screws (Figure 4.7). Maximum principal strain reduced from0.01218 to 0.00032 with increase in elastic modulus from 3 – 114 GPa.

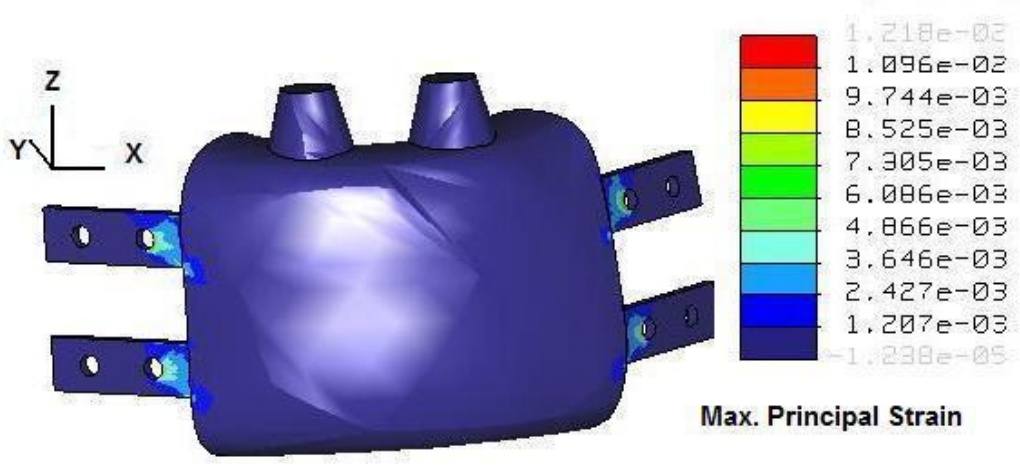


Figure 4. 7Model 1 Maximum Principal strain

Displacements are seen in the X, Y and Z directions of which the X and Z displacements are negligible. The maximum displacement is seen in the Y direction and is seen to be 0.01020 mm for an effective elastic modulus of 3 GPa which is seen to reduce to 0.00027mm when elastic modulus is increased to that of dense titanium as seen in Figure 4.8. The maximum Y displacement is seen in the lower part of the retention structures close to the distal ends of the implant (Figure 4.9).

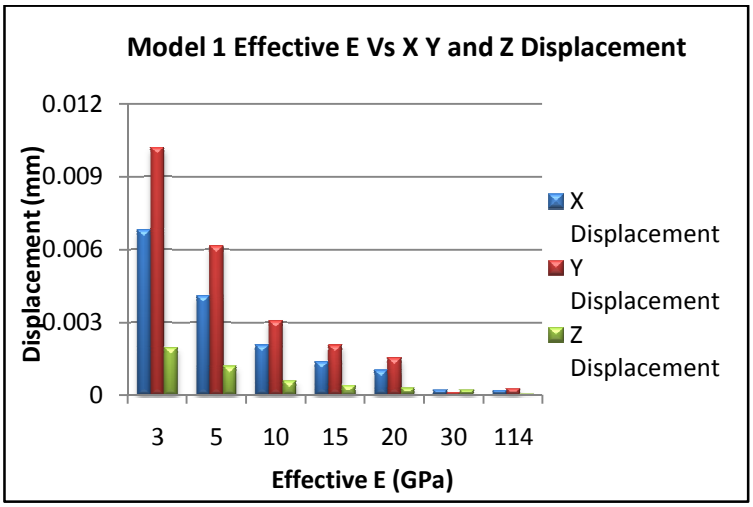


Figure 4. 8 Model 1 X Y and Z Displacement Effective E Vs Displacement

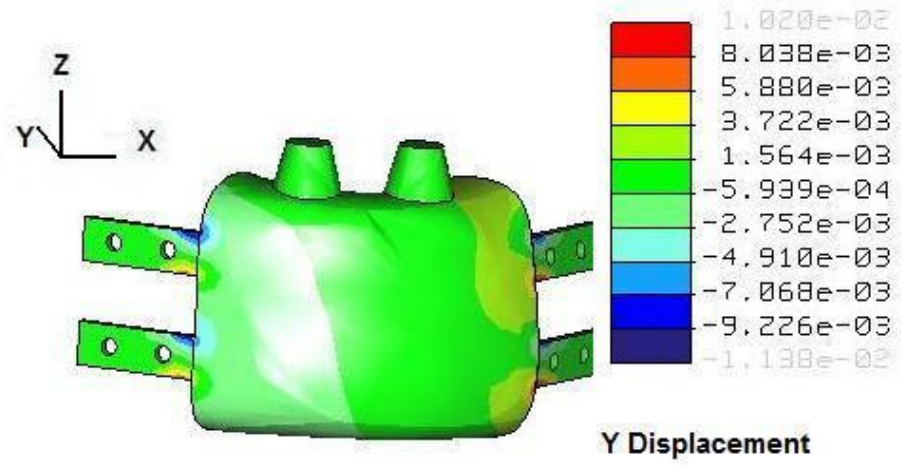


Figure 4. 9 Model 1 Y displacement

Model 2 Premolar to Subcondylar Reconstruction: Maximum Von Mises stresses for model 2 was 269.9 MPa. As seen in Figure 4.10 it was also seen at the screws on the first set of retention structures attached to the proximal end of the implant.

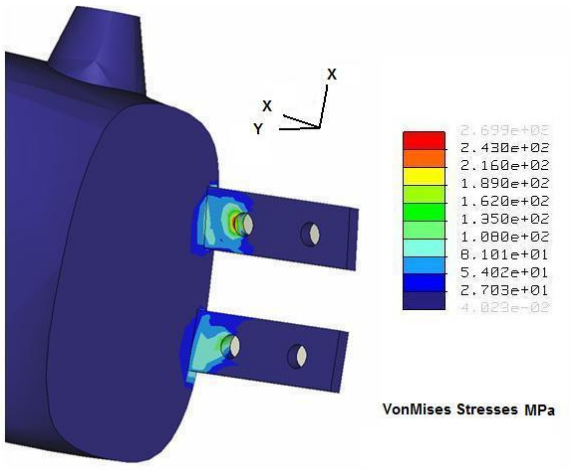


Figure 4. 10 Model 2 Von Mises stresses
Maximum stresses seen at the screw joints

A maximum principal strain of 0.07 was observed in the retention screws at the proximal retention structures (Figure 4.11). A maximum displacement of 0.06772 mm in

the X direction, a 0.045 mm in the Y direction and 0.05284 mm in the Z direction is seen as in figure 4.12.

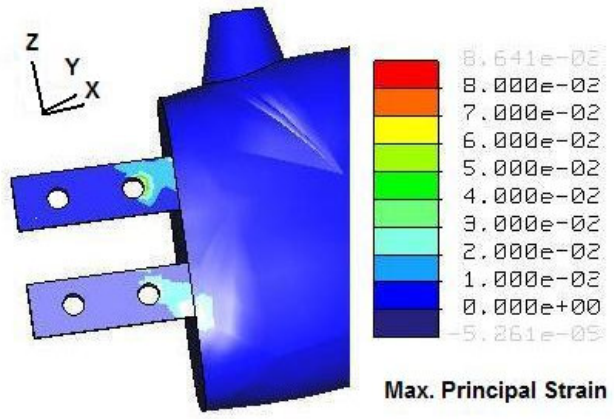


Figure 4. 11 Maximum Principal strain

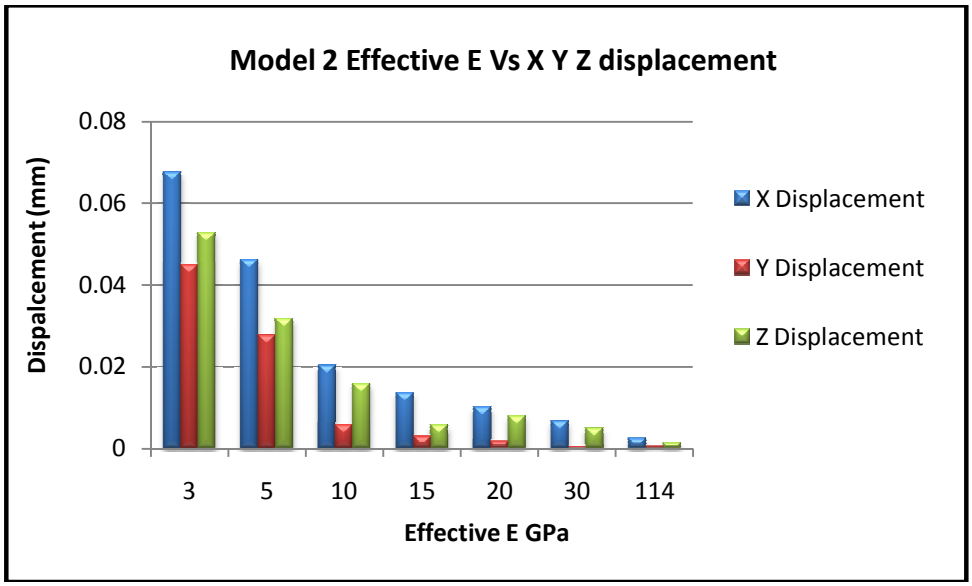


Figure 4. 12 Model 2 X Y and Z Displacement Vs Effective E

Model 3- Hemi mandible reconstruction

When a hemi mandible replacement is done, the implant could be subjected to varying loading patterns. Simulations of varying loading patterns were done as follows:

1. Incisor,

2. Premolar,
3. Molar,
4. Premolar and molar
5. Incisor, premolar and molar

Maximum Von Mises stresses for model 3 was seen at the screws on first set of retention structures as seen in Figure 4.13. VonMises stresses and shear stresses for the five load patterns are shown in Table 4.8.

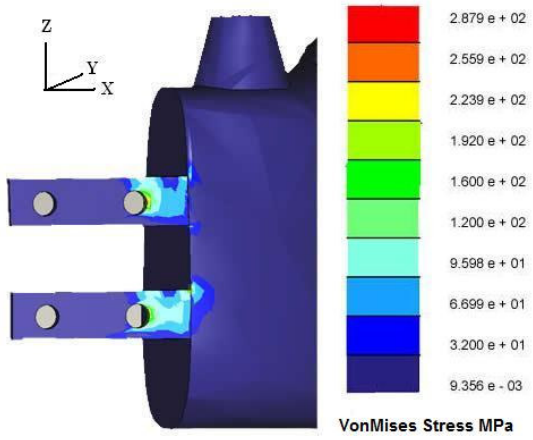


Figure 4. 13 Model 3 Von Mises stresses Maximum Stresses seen at the screw joints.

Table 4. 8 Model 3 VonMises stresses

Load pattern	Load Locations	Total load (N)	Von Mises stress (MPa)	Shear stress (MPa)
1	Incisor	60	43.01	22.44
2	Premolar	150	86.64	50.46
3	Molar	300	164.3	77.99
4	Premolar, Molar	450	245.8	127.4
5	Incisor, Premolar, Molar	510	287.9	149.2

The maximum principal stresses ranged from a minimum of 18.66 MPa for load pattern 1 to a maximum of 90 MPa for load pattern 5 (Figure 4.14). Similarly, the

maximum shear stresses ranged from a minimum of 22.44 MPa for load pattern 1 to a maximum of 149.2 MPa for load pattern 5.

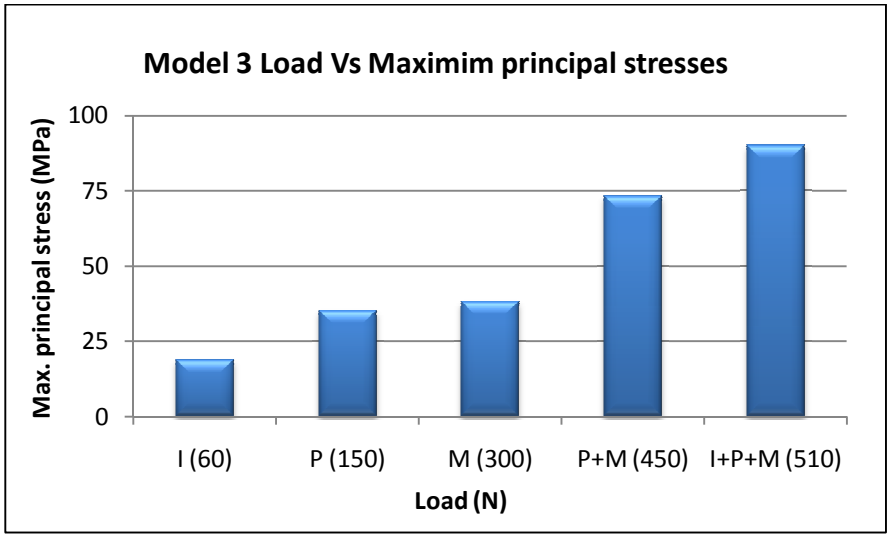


Figure 4. 14 Model 3 Load Vs Max principal stress

Maximum principal strains were observed in the proximal retention structures on the first set of screws and were very low. The maximum principal strains reduced from 0.03 for load pattern 5 for an effective elastic modulus of 3GPa (maximum load - minimum strength) to 0.0006827 when the elastic modulus equaled that of dense titanium.

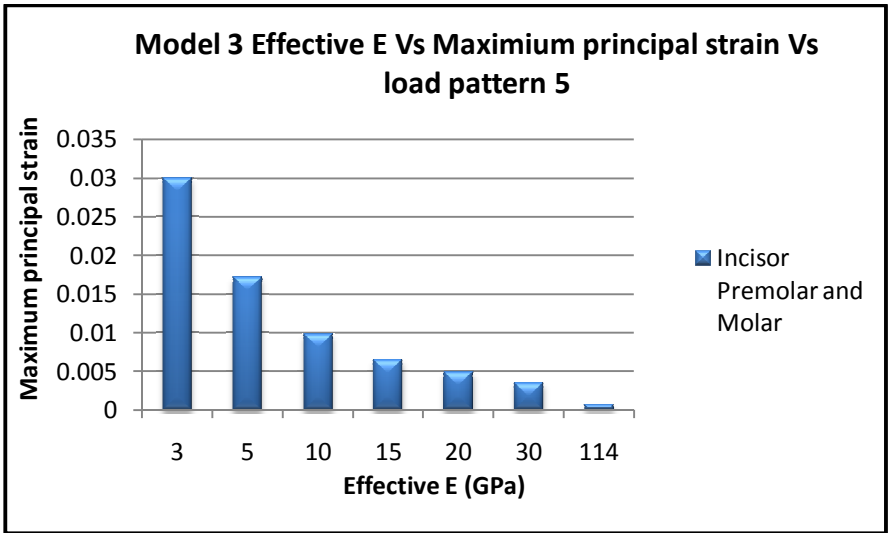


Figure 4. 15 Model 3 Effect of elastic modulus on Max principal strain for load pattern 5

Maximum displacements were seen for load pattern 5 for an effective elastic modulus of 3GPa and displacements in the X, Y and Z directions were 0.04, 0.0619 and 0.003909 mm respectively. Maximum displacements for all load patterns were seen in the Y direction (Figure 4.17).

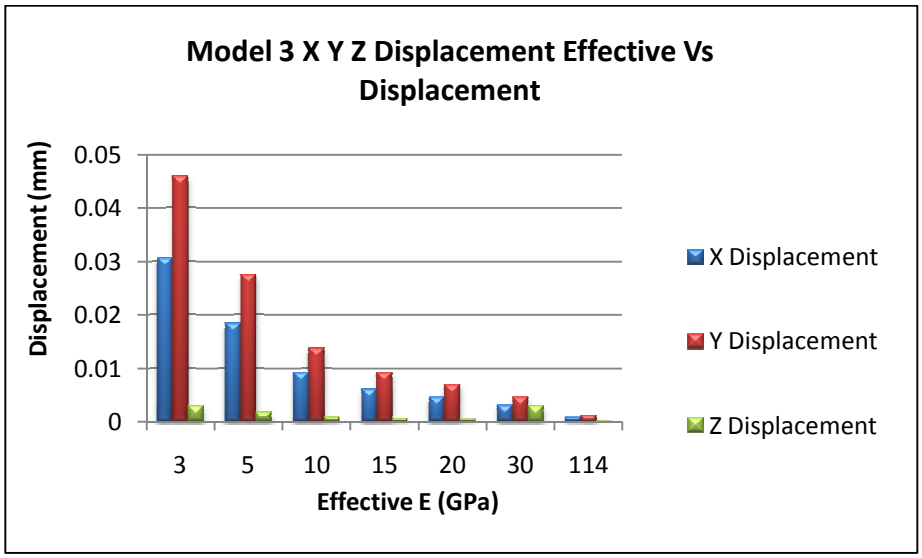


Figure 4. 16 Model 3 X Y Z Displacement Effective Vs Displacement

4.5 Discussion

The study has developed a repeatable design strategy for the fabrication of porous titanium mandibular implants with predictable properties. The main advantages over the previous methods are that implants with controlled shape and porosity can be designed for ingrowth of tissues for better integration (Lopez-Heredia, et al.2008). The second advantage of the design strategy is the restoration of the original anatomy for better aesthetics that would improve patient's acceptance. Dental rehabilitation which has been a major problem with generic reconstruction plates and bone grafts has been addressed by construction of dental implant abutments over which fixed prosthodontic restorations can

be made for improved masticatory functions. Mechanical properties of the implants have been modified for better integration. The weight of the implant has been reduced and effective elastic modulus of the implant material has been reduced close to that of cancellous and cortical bone.

4.5.1 Stresses Generated in Model 1, 2 and 3 due to Masticatory Loads

Medical grade titanium has an ultimate tensile strength of 970 MPa and yield strength of 930MPa. The implant itself can be porous but the retention structures and the dental abutments are fabricated as dense parts. Failure of the titanium implant from a strength perspective is highly unlikely. However, failure of the implant can occur due to high stresses at the screws in the retention structure which would be transmitted to the neighboring cortical bone with a tensile strength of 92- 185MPa causing micro fissures leading to loosening of the implant in the short term (An, 2000). In the long run, constant bone remodeling can reduce the risk; however, constant high stresses can lead to bone resorption leading to loosening of the implant (Knoll et al, 2006)**.** Since the retention structures for all the three implants resembled fracture fixation plates the results were compared with stresses generated in generic fracture fixation plates.

Model 1: The maximum Von Mises stress was 56.94 MPa which is very much lower compared to the tensile strength of titanium. The amount of stresses transferred to the screws and on to the cortical and cancellous bone would be very less than that of bone and therefore within acceptable limits. Maximum displacement of 0.01020 mm seen in the Y direction was well within the tolerance limits.

Model 2: The premolar to subcondylar model represented one of the most common clinical scenarios. Restoration of facial aesthetics and masticatory functions are the main

criteria in designing this implant. Buccal rotation of the implant during mastication, short thin segment of the residual ramus for distal fixation and high masticatory loads are some critical considerations in designing the implant. Hence, the right design would have the least stresses at the osteosynthesis screw holes in the retention structures. Von Mises stresses at the screws were 269.9MPa, only 25% of the ultimate strength of titanium giving a safety factor of 4. A high factor of safety is desired due to the fact that we have performed a static study and the assumption of a uniform elastic modulus for the implant. Increasing the size of the screws is shown to reduce the stresses. Maurer, et al, (1999) found that the maximum tensile strength was 610MPa for 1.5 and 2 mm screws and the acceptable chewing force would be 89.1N and 157.5 N respectively. Knoll et al (2006) increased the diameter of the standard reconstruction plates in their new design of reconstruction plates from 2.7mm to 4 mm (1.5 times). They found the stresses at the screws reduced from 1112N to 199N, 918N to 191N, 109N to 66N and 74N to 66N respectively. The authors also varied the configuration of the screws and the least amount of stresses were found with rectangular configuration of the screws.

In this study for Model 2, to reduce the stresses, the following modifications are made to the original design of the retention structures seen in Figure 3.9 b. Table 5 shows the VonMises stresses in the various modifications. Increasing the number of screws to 3 (model 2a) while keeping the diameter constant did not show significant reduction of stresses – 254.7 MPa. Increasing the diameter by 1.5 times to 3mm (model 2b) reduced the VonMises stresses from 269.9 MPa by 51.76 % to 130.2 MPa. The stresses are further reduced to 117.8 MPa (Figure 4.18) by merging the two plates at the proximal end into one as shown in table 5 – model 2c.

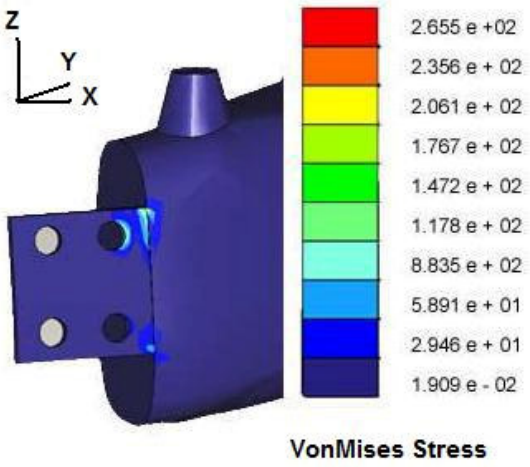


Figure 4. 17 Model 2c – finalized design - VonMises stress

Table 4. 9 Model 2 - Stress in screws of various modifications of the retention plate systems

Model No	No. of screws	Screw ϕ (mm)	Proximal plate	Von Mises stress (MPa)	Shear stress (MPa)	Distal plate	Von Mises stress (MPa)	Shear stress (MPa)
2	4	2		269.9	138.8		189.0	97.2
2a	6	2		254.7	115.4		159.2	82.4
2b	4	3		130.2	85.56		97.65	51.93
2c	6	3		117.8	62.79		88.35	47.09

Model 3: From the results of Model 2, it is observed that Model 2c, the 4 screw plate with 3mm screw holes has the least stresses. Therefore, this is incorporated in Model 3 by joining the two plates and increasing the screw diameter to 3mm to arrive at Model 3a. A maximum load of 510 N was applied on the Incisor, Premolar and Molar abutments (Table 4). The VonMises stress patterns are reduced as seen in Figure 4.19 and 4.20. From Figure 4.20, it is seen that the stresses are reduced by 44.35%. The maximum Von Mises stress for normal load on the incisor, premolar and molar together is 150.2MPa.

The final design of the implant would therefore be capable of withstanding 5 times the normal load.

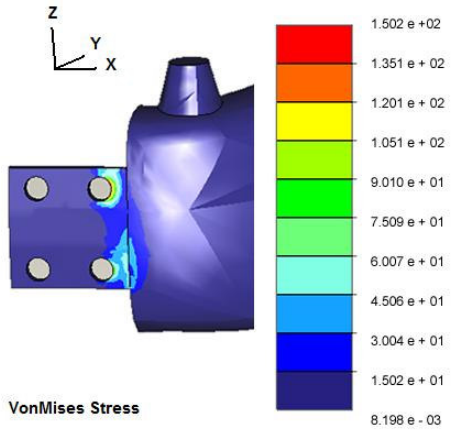


Figure 4. 18 Model 3b - Final design - VonMises stresses

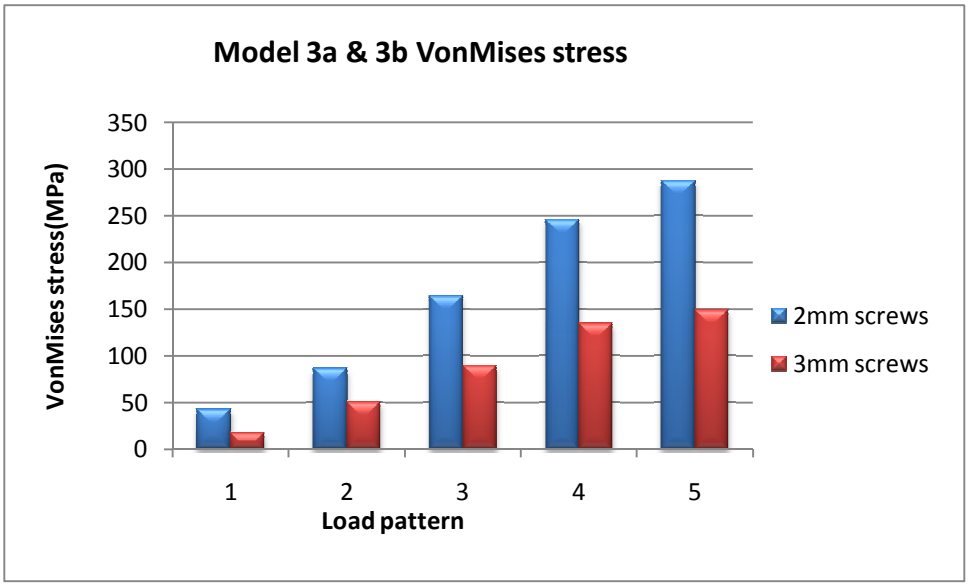


Figure 4. 19 Model 3a and 3b comparison VonMises stress

4.5.2 Micro-Motion

Micromotion occurs at the bone implant interface and leads to fibrous tissue apposition as against bone formation. Micro-motion is unavoidable during mastication. Bone tolerates micro motion in the range of 50 to 150 µm (Moncler et al 1998) beyond which bone resorption occurs leading to the loosening of the implant. The displacements in the X, Y and Z directions were studied for the three implant models and the maximum displacement was found to be .068 mm as seen in Figure 4.20.

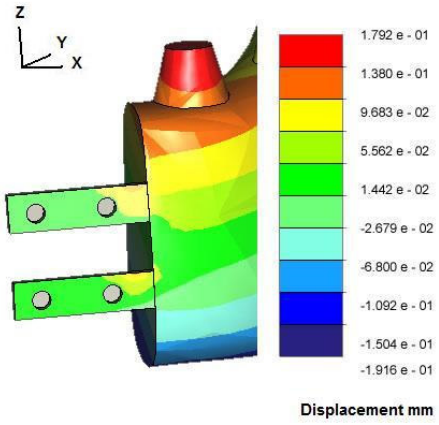


Figure 4. 20 Model 3 - Maximum displacement for effective elastic modulus of 3GPa

4.6 Fabrication of Porous Mandible by 3D Printing

To study the feasibility of fabrication of patient specific porous mandible with inbuilt dental abutments, a realistic digital reconstruction of a porous model as shown in Figure 4.21 is conceived. The body of the mandible is designed with square pores in the X, Y and Z direction and dental abutments are designed as dense structures. The .STL file of the model is transferred to a 3D printer (Z Corp) and printed. The rapid prototype model is seen in Figure 4.22. Similar procedures can be used to fabricate the model in metal

based rapid manufacturing systems such as EBM and DMLS systems available from commercial vendors.

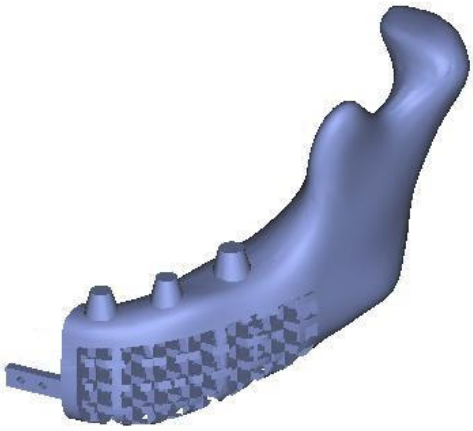


Figure 4. 21 CAD design of porous mandible for 3D printing

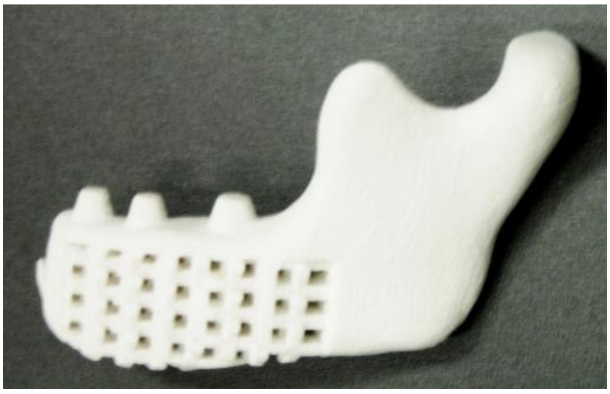


Figure 4. 22 3DP model of porous mandible

A design strategy has been developed for the eventual direct fabrication of Titanium implants for mandibular reconstruction with mechanical properties close to that of bone. Advantages of this design strategy are the preparation of custom porous titanium implants with controlled mechanical properties. The mechanical properties within the implant can also be varied according to the anatomical region of implantation. With the predicted

mechanical properties, masticatory and other functions of the mandible can be tested and implants with better longevity can be fabricated. This strategy can be applied to the design of custom implants for other parts of the body as well. Patients requiring mandibular reconstruction would have better aesthetics and functions with this new innovative design of implants. The Electron Beam Melting process of manufacturing is discussed in the next chapter.

CHAPTER 5

5. EVALUATION OF POROUS TITANIUM CONSTRUCTS FABRICATED USING EBM

5.1 Summary

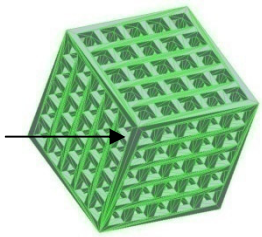
EBM is a direct CAD to metal rapid prototyping process that lends itself to fabrication of porous metal parts. This chapter describes the fabrication of porous titanium constructs to be used as bone replacements in craniofacial applications. The characterization of external surface constructs using an optical microscope and internal architecture using Micro CT will be discussed herein. The evaluation of the mechanical properties of the constructs will also be discussed.

5.2 Electron Beam Melting (EBM)

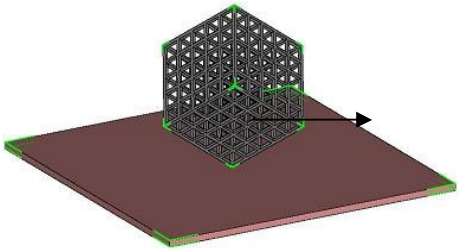
EBM is a direct CAD to metal, rapid prototyping process for the fabrication of dense and porous metal parts. The EBM system is manufactured by Arcam AB (Krokslätts Fabriker 27A, SE-431 37 Mölndal, Sweden). EBM is a rapid manufacturing process in which fully dense solid parts are fabricated by melting the Ti6Al4V powder layer by layer with an electron beam. The process uses .STL data (triangulated model) of the part to be fabricated. The .STL model of the part is sliced into different layers, with each contoured layered data passed onto the system. Parts are built through a layer by layer process by the directed solidification of the metal powder. The process is shown in Figure 5.1. The fundamental difference between EBM and the Selective Laser Sintering (SLS) process is that the EBM process uses an electron beam to melt the powder while SLS and SLM use

lasers to melt the powder, making the process faster with fully dense parts. The availability of high energy electron beams ensures the complete melting of the powder particles. Metallurgical bonding between layers as in all additive manufacturing processes results in the complete part. In addition, parts are fabricated in a vacuum chamber during the EBM process, which assures impurity free titanium parts unaffected by oxygen and other chemicals available in the atmosphere. The residual stresses are also minimized due to vacuum processing. Once the green parts are obtained from the system, the parts are cleaned to remove loose titanium powder lodged within the porous structure. This is usually done by a blast of high pressure silicon micro-beads filled air stream. Mechanical properties of EBM parts are comparable to ASTM F1108 cast material as seen in Table 1 (www.ARCAM.com) showing the process to be suitable for the fabrication of porous parts with mechanical strength equivalent to parts built from conventional manufacturing processes.

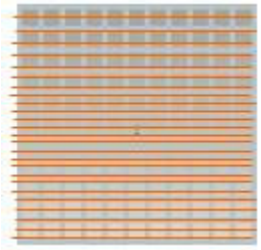
Figure 5.1 shows the steps involved in fabrication of a part with EBM machine



CAD model and input .STL file



Part orientation

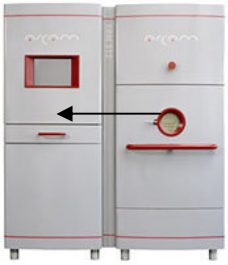


Slicing

88



Porous titanium parts



Arcam EBM S12

Tool path generation and setting process parameters

Figure 5. 1 Steps in fabrication of an EBM part

Table 5. 1 Mechanical properties of EBM processed Ti6Al4V

Mechanical properties		
	Arcam Titanium	**Titanium Required (Cast)**
Yield Strength (Rap 0,2)	910–940 MPa	758 MPa
Ultimate Tensile Strength	950–990 MPa	860 MPa
Rockwell Hardness	30–35 HRC	30–35 HRC
Elongation	14–16%	10%
Fatigue strength@600 MPa	>10,000,000 cycles	>1,000,000 cycles
Modulus of Elasticity	120 GPa	114 GPa

The schematic working of an EBM machine is shown in Figure 5.2. The equipment consists of an electron beam head with tungsten filament, a powder container, spreader, and a build table. The tungsten filament reacts with excited electrons causing a beam of electrons to pass out from the head. Two magnetic fields are present of which the first one organizes the electron beam in the desired shape and the second deflects the beam to the target position. The melting of the metal powder results from contact of the electron beam on the surface of the metal powder bed when the kinetic energy is changed to thermal energy that is above the melting point of the metal. The electron beam scans the metal bed in accordance to the slice data generated from the input CAD file and solidification occurs by cooling. Once a layer of powder is melted and solidified, the next layer of powder is spread and the process is repeated until the part is completed. The process takes place in a bed of the metal powder that acts as a support during fabrication of overhanging features. Fully dense parts comparable to ASTM F 136-02a and ASTM F 1108-04 standards of titanium are fabricated as the powder is melted and held together (Christensen et al 2007).

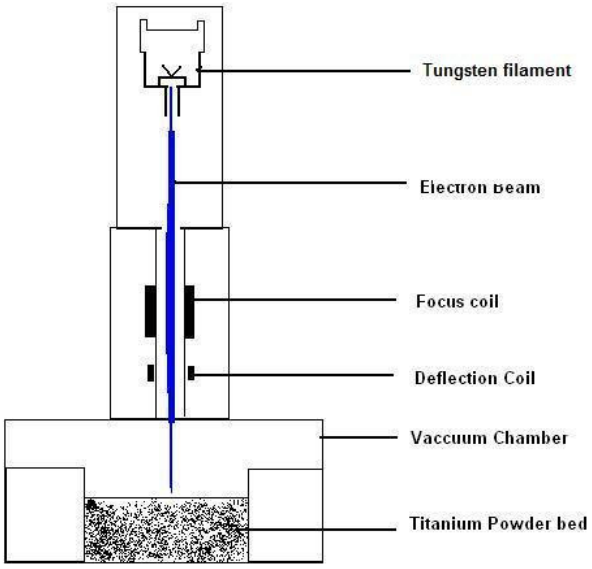


Figure 5. 2 Schematic of representation of working of EBM

EBM Characteristics and Process Parameters
Characteristics and process parameters of ARCAM EBM S12 machine are

1. Building tank volume 250x250x400 mm or 350x350x250 mm
2. Maximum build size 200x200x350 mm or 300x200 mm
3. Layer thickness 0.05–0.2 mm
4. EBM POWER – 5 – 20 mA
5. EB scan speed > 1000 – 5000 m/s
6. EB positioning accuracy +/– 0.025 mm
7. Build orientation
8. Part Accuracy +/– 0.3 mm
9. Power supply 3 x 400 V, 32 A, 7kW
10. Size and weight 1850 x 900 x 2200 mm (W x D x H) 1420 kg
11. Process computer PC, XP Professional
12. CAD interface Standard: STL

5.3 Fabrication of Porous Parts

5.3.1 Input CAD File

For our study, a total of 28 parts with three different porosities ranging from 50.75 - 70.32% (4 sets of 7 each) were fabricated. The parts were designed as 15mm cubes. For three sets, the strut dimension was kept constant at 800µm, with the pore size

varied to obtain different porosity ranges (Figure 5.3). The fourth set of 7 parts was built with an average porosity of 49.75% was fabricated with a reduced strut size equivalent to 450µm. Table 2 summarizes the pore size, the number of pores and the porosity values for each set of cubic structures fabricated.

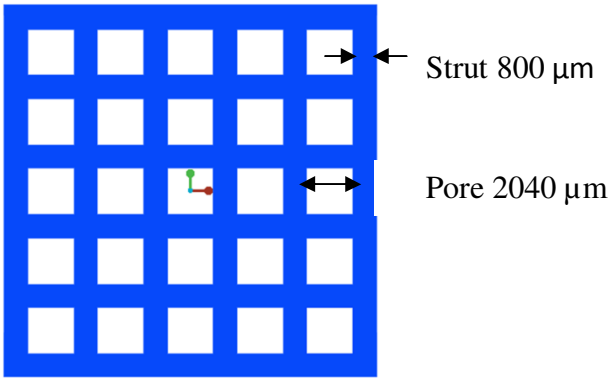


Figure 5. 3 Design of cube with porosity 75.83 %

Table 5. 2 Pore and Strut sizes, number of pores and varying porosities

Set No	Pore size (µm)	Strut size (µm)	No. of pores	Porosity %
1	1230	800	7	60.91
2	1570	800	6	68.6
3	2040	800	5	75.83
4	1000	450	10	74

Parts were designed in CAD using Pro Engineer (PTC, MA) and .STL files transferred to the EBM machine for fabrication.

5.3.2 Part Orientation

Part orientation partially determines the amount of time required to build the model. Placing the shortest dimension in the z direction reduces the number of layers, thereby shortening build time. The part orientation also affects surface finish and the strength

of the part. In our experiment, all parts were oriented as shown at 45 Degrees for equal strength in both parallel and perpendicular to build direction (Figure 5.1).

5.3.3. Adaptive Slicing and Tool Path Generation

The next step is to slice the .STL model into thin cross-sections for tool path generation. The slice thickness is the layer thickness for fabrication. The slicing thickness depends on the build style. During this step, support structures are also generated to support overhangs and thin-walled sections during the build, but in ARCAM EBM, the process takes place in the powder bed which itself acts as a support for the overhangs. The variable layer thickness is used in an adaptive fabrication process, generally thinner layers being used where part detail is greatest and a better surface finish is desired at the cost of manufacturing time. The Arcam EBM control software creates slice-files from input .STL file. Layer thickness of 100µm is maintained for all the parts. Ti6Al4V powder supplied by ARCAM AB with powder particle size at 40 – 80µm is used. Other machine parameters that are set to default are as follows

1. Scan speed = 1500 m/sec
2. Beam Power = 15mA
3. Line offset = 0 mm

Once all the above parameters are set, the tool/scanning path is generated. The machine then focuses the electron beam on the powder bed to melt completely the powder in accordance to the CAD file. As the molten metal cools, the layer solidifies to the specified pattern shape. The process continues until every layer is deposited and patterned using the electron beam. Figure 5.4 shows the porous Ti6Al4V parts fabricated using the EBM system.

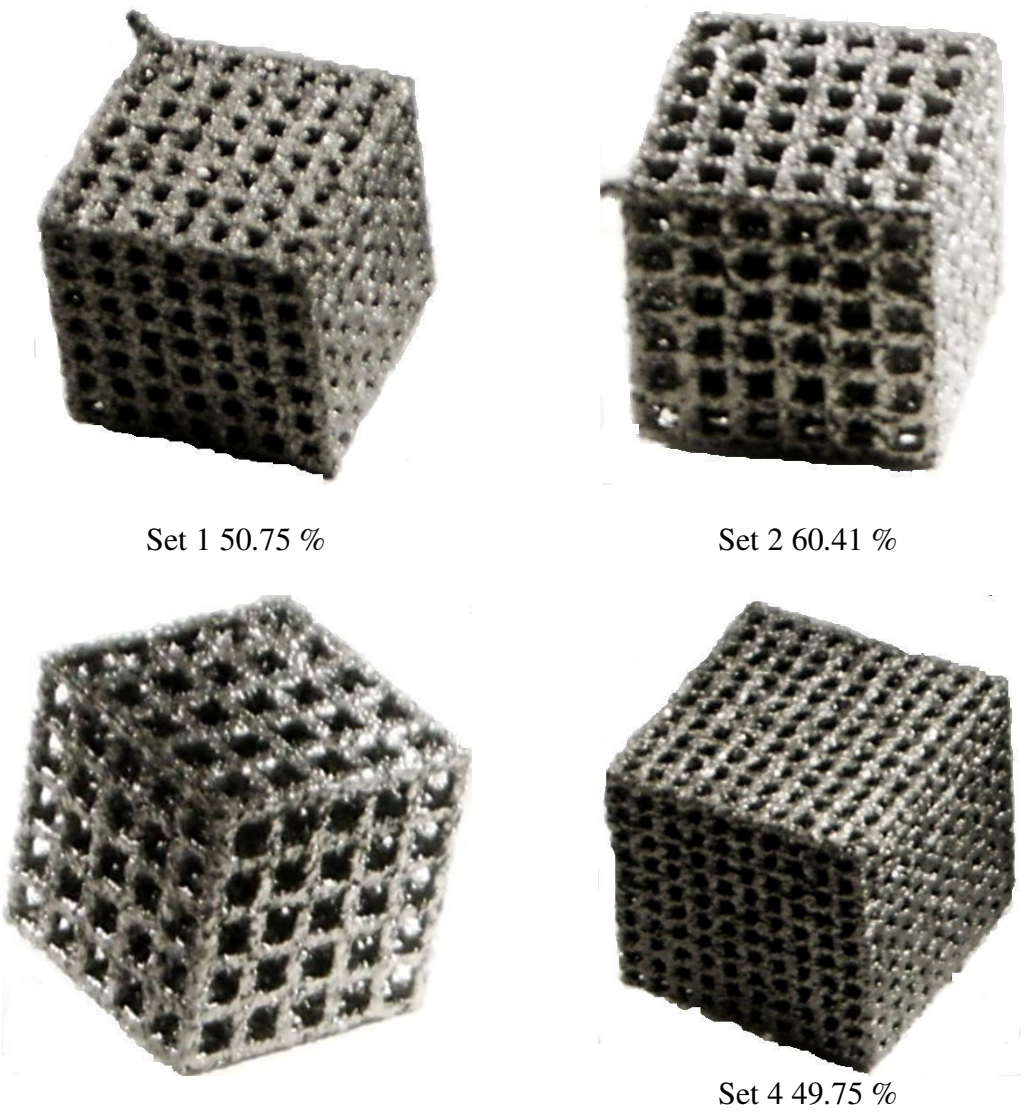


Figure 5. 4 The designed porosity of Ti6Al4V parts fabricated with the EBM system Set1,2,3 and 4

5.4 Characterization of Porous EBM Titanium Parts

Structural analysis of the fabricated porous parts was conducted to ascertain the effect of process parameters on the internal architecture and external topology of the part. Specifically, the strut thickness, pore size and pore shape were studied both from the

external and internal view. Porosity of the fabricated part was varied by varying the size and number of the pores.

5.4.1 External Characterization

The manufacturing process involves high temperatures of above 1666^0 C. These high temperatures on the material could have an effect on the pore and strut sizes of the final part. Optical microscopy and Scanning Electron Microscopy (SEM) are used to study the variation in pore and strut sizes that occurred due to the manufacturing process. Surface characteristics of the EBM fabricated titanium parts are also studied

Optical Microscopy

An optical microscope Leica (Figure 5.6) is used to analyze the external pore and strut size of the fabricated parts. For every digital image acquired, twenty four pores and struts (4 in each of the 6 sides) of the cube, are randomly selected and measured both in the X and Y directions, and average values calculated.



Figure 5. 5 Optical Microscope – surface characterization

Scanning Electron Microscopy

Scanning Electron Microscope (SEM) takes an image of the sample surface by scanning it with a high-energy beam of electrons instead of a light source as in an optical microscope in a raster scan pattern. The scanning electron microscope (SEM) uses a focused beam of high-energy electrons to generate a variety of signals at the surface of solid specimens. The signals that derive from electron-sample interactions reveal information about the sample, including external morphology (texture), chemical composition, and crystalline structure and orientation of materials making up the sample. In most applications, data are collected over a selected area of the surface of the sample, and a 2-dimensional image is generated that displays spatial variations in these properties. Areas ranging from approximately 1 cm to 5 microns in width can be imaged in a scanning mode using conventional SEM techniques (magnification ranging from 20X to approximately 30,000X, spatial resolution of 50 to 100 nm). The SEM is also capable of performing analyses of selected point locations on the sample; this approach is especially useful in qualitatively or semi-quantitatively determining chemical compositions using X-ray Dispersion Spectrometry (EDS).

Since the EBM process builds parts through melting of Ti6Al4V powder layer-by-layer using high temperatures, it is essential to analyze the surface characteristics of the finished part to assess the metallurgic bonding between the layers. Presence of void spaces between the layers would lead to reduction in strength of the finished product. Scanning Electron Microscope Carl Zeiss DSF 960 (Figure 5.6) is used to study the microstructural surface characteristics and pore morphology within the

structure in high resolution. Since titanium is a conductive material, no preparation is necessary and the sample is placed inside the chamber directly. Surface images of varying regions of all the six surfaces are taken. Pore and strut measurements of the samples are also taken. High resolution images of the metallic surface are analyzed for interlayer metallic bonding. Chemical composition is analyzed by performing EDS studies.



Figure 5. 6 SEM Carl Zeiss 960

5.4.2. Internal Characterization

Micro-CT scans of the part is a nondestructive technique for visualizing features in the interior of opaque solid objects and for obtaining digital information on the 3-D geometry of the part. It is useful for a wide range of materials, including rock, bone, ceramic, metal, and soft tissue. A sealed high resolution x-ray source with a spot size <5 µm is focused on the object that is rotated, and 2D images are captured with a CCD camera at each rotation.

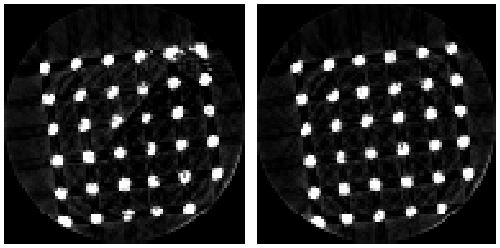
A cone beam micro CT scanner (Scanco, Medical Swiss) in Figure 5.7 is used and 2D slice image data are collected for the samples. The output data are 512 X 512 bitmap images collected at every 21µm slice levels of the part. Image analysis of this data included 2D analysis of individual slices and 3D volumetric reconstruction of the image data. CT image data reconstruction software MIMICS^{TM} (Materialise, Belgium) is used to reconstruct the 3D model of the fabricated parts using the obtained scan data. By analyzing the 3D model, it is possible to determine any internal defects, measure internal strut dimensions, find defunct void spaces and blocked pores. Geometric size of the pores, pore size distribution, surface area, and pore connectivity are studied using Micro CT data. Porosity of the part is calculated from the volume of the pores and the bounding volume of the part. Figure 5.8 shows processes in micro CT image reconstruction. A volumetric model was created for one sample in each of the three sets of parts.



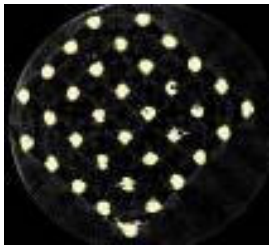
Porous Ti6Al4V part



Micro CT scanner



2 D images – slice data



Thresholding



3D reconstruction

Figure 5. 7 Micro CT Imaging, MIMICS 2D image thresholding and 3D reconstruction

5.4.3 Evaluation of Mechanical Properties

Porosity Measurement

In this research the bulk volume is calculated using micrometer measurements. Weights of the parts are determined after being placed in a Soxhlet extractor for removal of contaminants and drying in an oven for 12 hours.

Measurement of Pore Volume by Helium Pycnometry

Porosity of the fabricated parts was varied by varying the size and number of the pores. Helium Pycnometry has been used by (Semel & and Lados, 2006) and (Presz, Skibska, & and Pilecki, 1995) for determining porosity and density of porous materials. and pore volume is estimated using a Low Pressure Pycnometer (LPP) Accu Pyc 1330 Pycnometer from Micromeritics Instruments Corporation Figure 5.8.



Figure 5. 8 Helium gas Pycnometer used for estimation of pore volume

A pycnometer is a volume measuring instrument based on the pressure equalization principle. Any gas may be used but helium is preferred due to its small atomic size and negligible adsorption at ordinary temperatures. A typical pycnometer consists of two chambers of known volume reference chamber (1) and experimental chamber (2), a pressure monitoring device and a regulated high pressure source. The chambers are connected in series to the helium source. The specimen is placed in one of the chambers and helium gas is purged for several minutes to replace the air in the chambers. After the purge cycle

i. the two chambers are pressurized to 20 psi

ii. the chambers are isolated and one is pressurized to a higher value

iii. the chambers are then reconnected and the pressure difference between the two is equalized to an intermediate value.

The apparatus uses Boyle's law principle to measure grain volume. Therefore grain volume is calculated using

$$P_1V_1=P_2V_2 \qquad (4)$$

Where P_1 = pressure in the chamber 1 (20 psi), V_1 = Initial volume of helium in the chamber, P_2 = Pressure in the chamber and V_2 = Final volume of helium in the chamber.

Volume of the pores is then calculated as the difference between the actual volume of the part and the grain volume. Porosity is then determined using the equation

$$P = \frac{V_1 - V_2}{V_1}$$

Where V_1= volume of the part, V_2= volume of the pores.

Porosity is then calculated as follows:

Grain volume = $V_1 - V_2$

Pore volume = Bulk volume – grain volume

Porosity % = Bulk volume – grain volume/Bulk volume *100

Grain density = Weight of the sample/Grain volume

Compression Testing

Strength of porous Ti6Al4V implants is related to the porosity of the part. The effective stiffness and eventually the compressive strength of the part are reduced with increasing porosity. Axial compression tests were done to evaluate the stiffness of the porous Ti6Al4V parts as per ASTM D695 - 02 using an MTS alliance RT30 electromechanical testing test frame (MTS systems, MN) as seen in Figure 5.9. Compressive test to failure was done at a crosshead speed of 1 mm/min (Hienl et al 2007)**.** The maximum load of the machine was 20,000 N. A real time compressive load vs. displacement was continuously monitored and recorded. The stress-strain curves were generated for each sample set. Stiffness of the porous parts is calculated as the value of the slope of the stress - strain curve in the linear region. Average values of stiffness of the sample groups are taken as the stiffness value for the given porosity.



Figure 5. 9 MTS alliance RT30 electromechanical testing test frame

Shear Testing

A fixture was designed and fabricated as in, Figure 5.10, using stress proof steel, which is partially heat treated. It was designed to have the part set directly into the fixture, and then the part was epoxied to the fixture without using any holders. Also there were screw holes set into either end of the part in order to attach the fixture to the machine. The part was then epoxied to the fixture using JB Weld epoxy. The part was epoxied to one arm first and then placed in a 140^0 F oven for thirty minutes in order for the epoxy to set. The part and arm were then removed from the oven and cooled for a few minutes. After cooling, the second arm was epoxied to the part and the fixture was placed back in the oven for another thirty minutes. The fixture was then removed from the oven and left to set overnight before the testing process. The final setting of the part within the fixture is seen in figure 5.11.

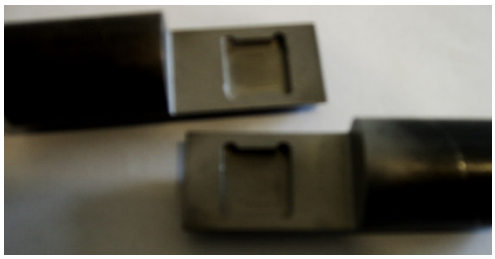


Figure 5. 10 Fixture for shear testing

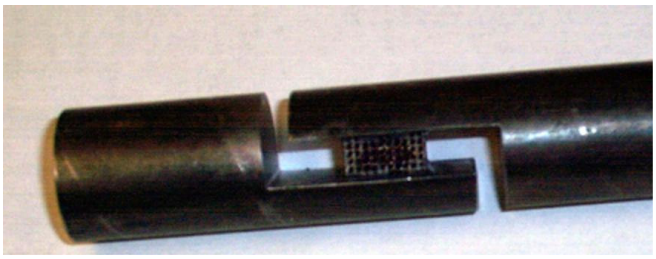


Figure 5. 11 Porous titanium part epoxied to the fixture

The machine used to test the part is a Com-Ten tensile test machine. The deflection limit was set to 10 mm. The test was conducted by the machine pulling the lower end of the fixture down and shearing the part as it is pulled. A bored out piece of brass was placed over the fixture for holding the fixture, part and epoxy together. This was then bolted, as seen in Figure 5.12, into the machine tests and conducted. The tests were then run and data collected for the displacement and the force. As the force of the machine increased, the fixture emitted a cracking noise, and the sample snapped. At this point the test was stopped.

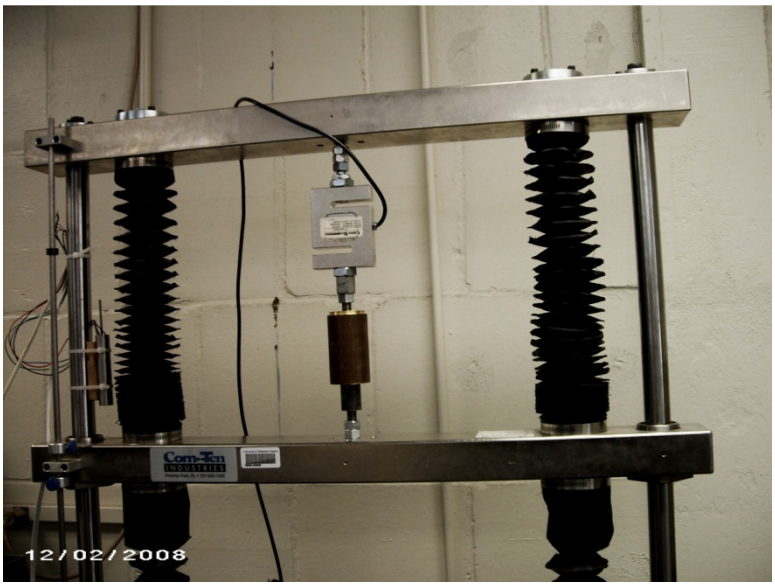


Figure 5. 12 Fixture bolted to the tensile testing machine

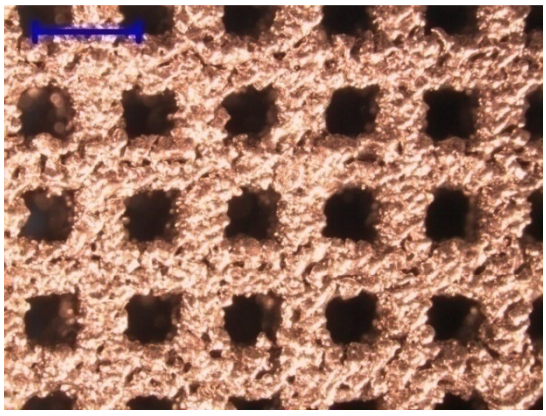
The data collected from this test are the displacements and the forces reached as the fixture was pulled. This data is then used to plot the stress versus strain curve. Stress is the force divided by the area of the part, and strain is the displacement divided by the original length of the part. The shear modulus is then the slope of the stress - strain curve.

5.5 Results

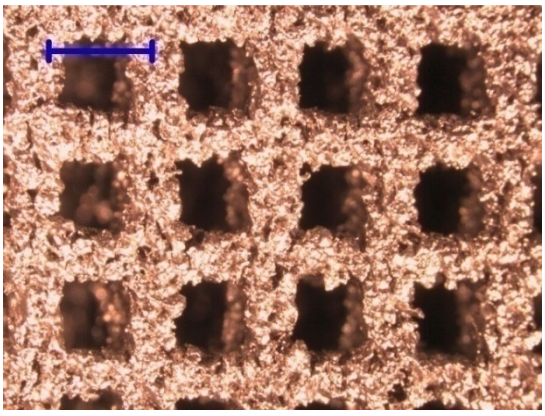
5.5.1 External Characterization

Optical Microscopy

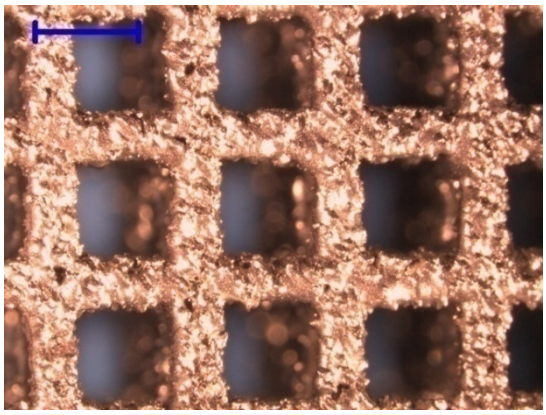
Figure 5.13 shows the optical microscope image of the exterior face of the part. Although the surfaces of the parts are very rough, the struts are well formed and continuous. Twenty four pores, 4 in each of the 6 sides of the cube, were randomly selected and measured both in the X and Y directions and average values were calculated. Table 5.3 shows the average strut and pore sizes for the various samples as measured by the optical microscope. All the seven samples in each set are evaluated.



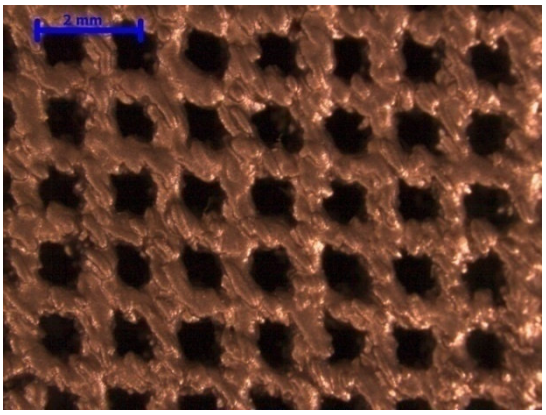
50.75 %



60.41 %



70.32 %



49.75 %

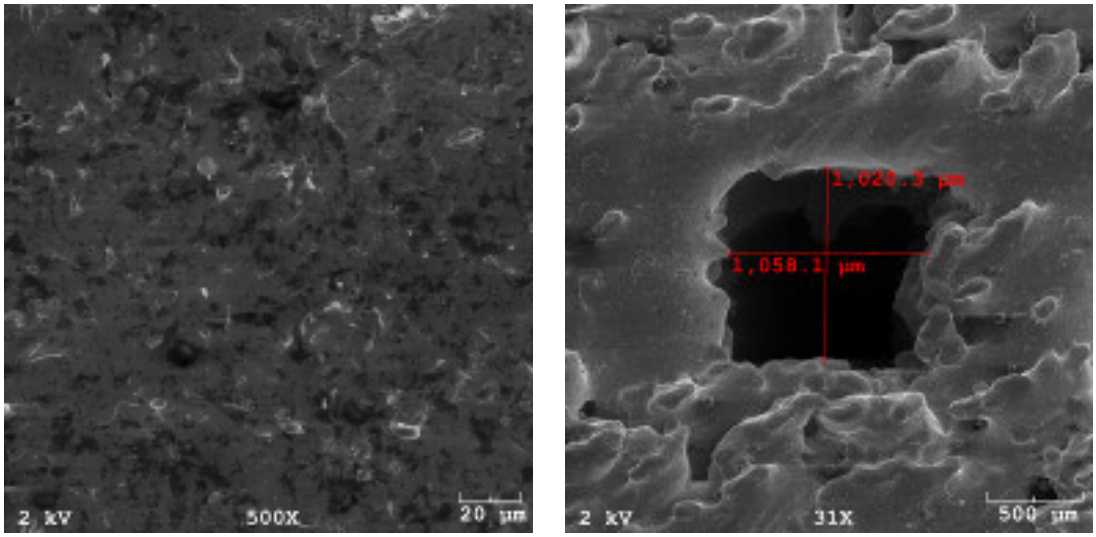
Figure 5. 13 Optical microscope images set 1, 2, 3 and 4 (scale bar = 2mm)

Table 5. 3 Average strut and pore sizes for the samples (n=7)

Set No	Actual strut size (µm)	Pore size (µm)
1	941 (+/-17.1)	1020 (+/- 45.0)
2	905 (+/-16.9)	1424(+/- 42.1)
3	882 (+/-13.2)	1960 (+/-49.4)
4	466 (+/- 39.7)	765(+/- 29.7)

Scanning Electron Microscopy

SEM images show no inter-layer differentiation when probed on the exterior face of the part. This indicates complete melting of powder metal and good metallurgical bonding between layers during the fabrication process as seen in Figure 5.14(a). Figure 5.14 (b) shows the pore dimension in the X and Y directions to be equal.



(a) **(b)**

Figure 5. 14 (a). SEM image of surface microstructure showing complete melting of powder particles. (b) SEM image of showing pore size

X-ray diffraction studies show the presence of mainly titanium, aluminum, vanadium, and small amounts of carbon, oxygen and silica are also seen (Figure 5.15). Silica is a residue of post processing wherein silica beads were blasted to remove the entrapped Ti6Al4V powder particles present inside the pores that act as the support material during the fabrication process. Presence of silica is also observed during high resolution scanning (Figure5.16).

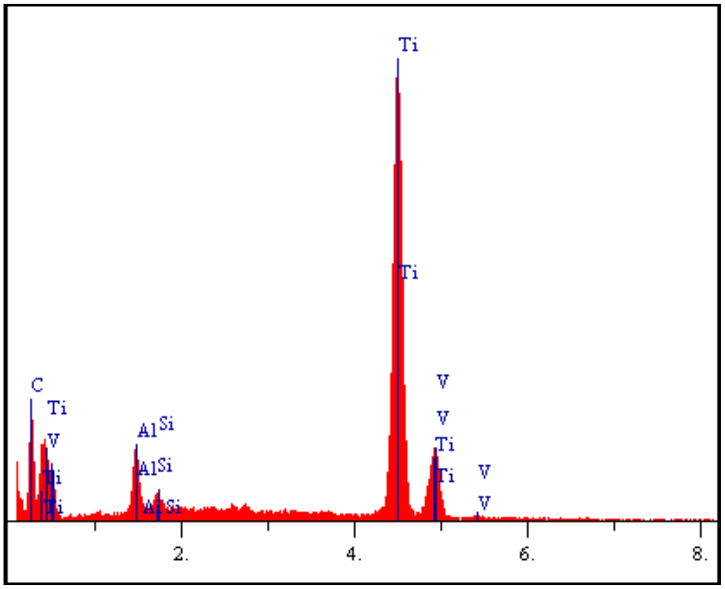


Figure 5. 15 EDS analysis of Ti6Al4V surface

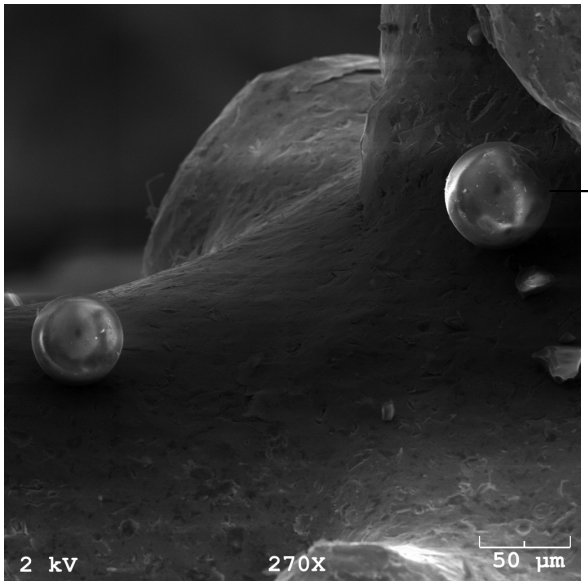


Figure 5. 16 SEM image showing Silica bead

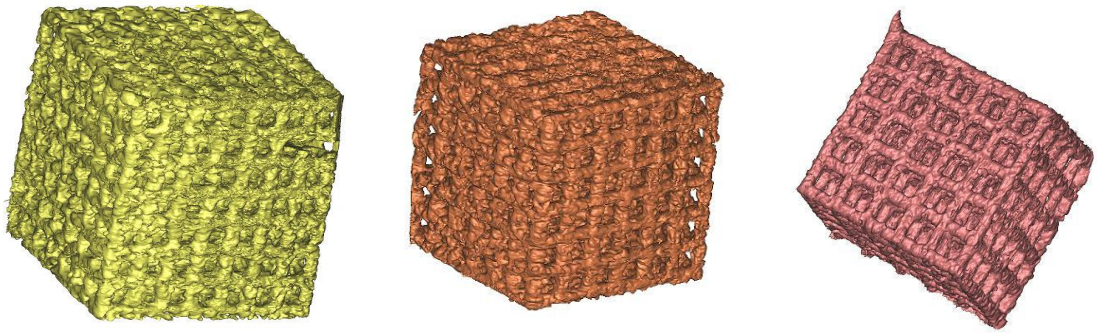
Elements present as observed by EDS evaluation studies are seen in Table 5.4. The percentage of the individual elements, however is not very reliable as the EDS calculation assumes smooth surface which is not the true with porous EBM parts.

Table 5. 4 EDS evaluation of elements present

Element.	Error 2-sig	Atomic %	Conc.	Units
C	0.670	17.437	6.667	wt.%
O	0.551	27.881	14.200	wt.%
Al	0.886	5.161	4.433	wt.%
Si	0.480	1.377	1.231	wt.%
Ti	2.801	46.997	71.611	wt.%
V	0.420	1.146	1.859	wt.%
		100.000	100.000	wt.%

5.5.2 Internal Characterization

Pore size distribution, surface area, pore connectivity, and porosity are studied using MicroCT data. Pores are evenly distributed and interconnected throughout the part. No evidence of residual metal particles is seen in any of the specimens. Figure 5.17 shows the 3D reconstructed models of sets 1, 2 and 3 of porous parts.



Set 1	Set 2	Set 3
Porosity – 50.37%	Porosity – 60.29%	Porosity – 71.32%
Surface – area 7534.32 mm^2	Surface – area 5588.82 mm^2	Surface – area 4158.64 mm^2

Figure 5. 17 3D reconstruction and analysis of micro-CT data

Since porosity has been varied by reducing the number of struts and increasing pore size in this design, the surface area is seen to decrease with increase in porosity as seen in Figure 5.18.

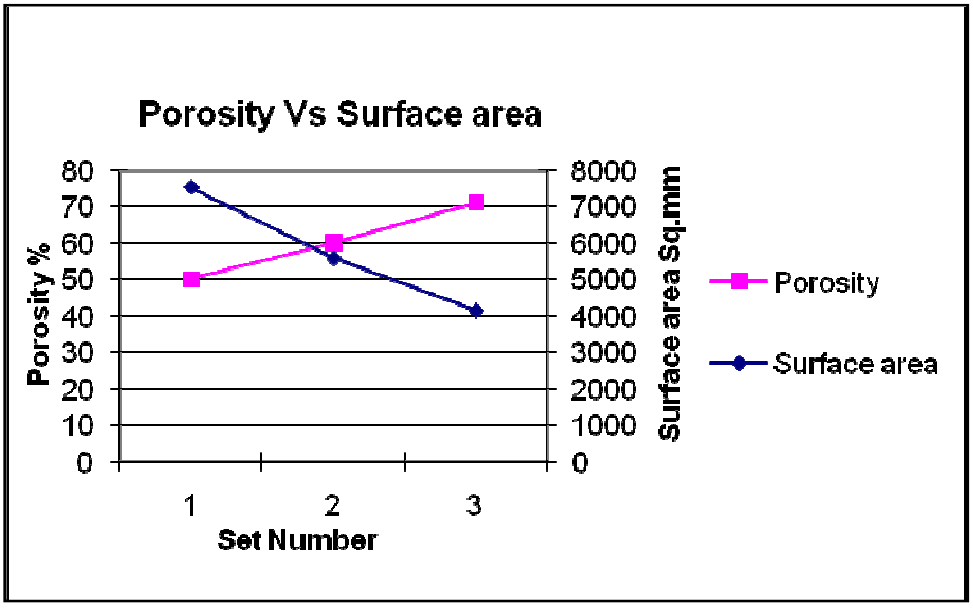


Figure 5. 18 Porosity Vs Surface area micro CT data

5.5.3 Evaluation of Mechanical Properties

Porosity

The parts were designed as 15 mm cubes. The average measured length of the parts is 15.15 (+/- 0.046)mm which is 1% more than the intended design. The average volume of the parts is 3479.365 (+/- 31.80) mm^3 as against the design volume of 3375 mm^3 which is 3.29% over the design volume. The average grain density of the Ti6Al4V structures is 4.42(+/- 0.14)g/cm^3 equivalent to that of dense Ti6Al4V. Table 5.5 shows the experimental weight and porosity values compared to that of the theoretical values. Calculation of theoretical values of weight is done by assuming the density of dense Ti6Al4V to be 4.42g/cm^3. Figure 5.19 shows the comparison between theoretical, experimental and micro CT image calculations of porosity of the samples as displayed in Table 5.2. The difference in values between the theoretical and experimental values can be attributed to the undulations on the surface of the solid Ti6Al4V structure. The designed parts are taken as flat surfaces for calculation of porosity values.

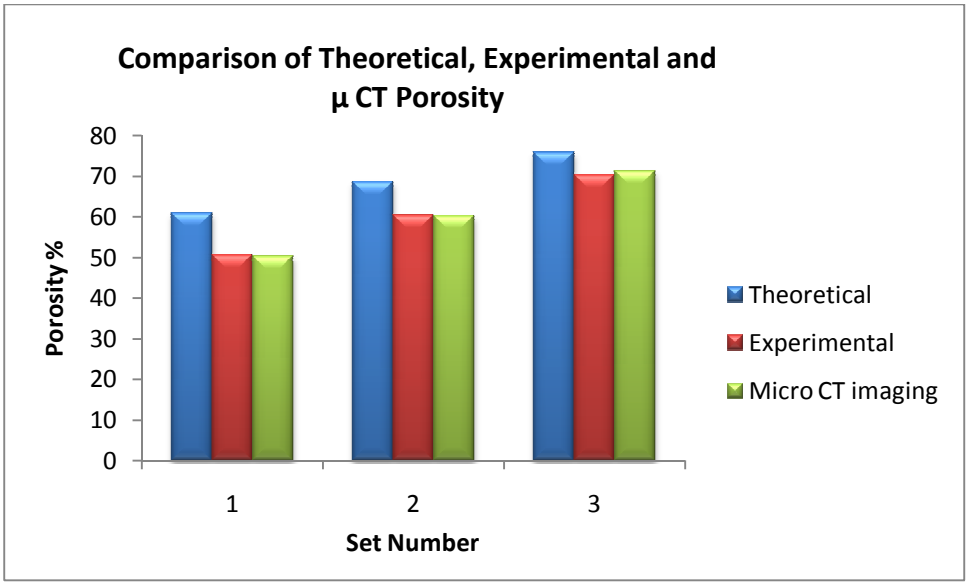


Figure 5. 19 Comparison of Theoretical, Experimental and Micro CT Porosity

Table 5. 5 Comparison of theoretical and actual values of weight and porosity

Set No	Parameter	Theoretical	Actual (n=7)	Difference %
1	Weight (g)	7.35	6.15 (+/-0.07)	15.04
2		5.89	4.99 (+/-0.09)	10.48
3		4.43	3.92 (+/- 0.06)	7.26
4		7.64	6.03 (+/- 0.06)	21.07
1	Porosity (%)	60.91	50.75 (+/- 0.69)	15.04
2		68.60	60.41 (+/- 0.81)	7.19
3		75.83	70.32 (+/- 0.63)	5.51
4		65.02	49.75 (+/- 1.00)	23.49

Compression Testing

Force displacement data was collected from which stress/strain values were calculated and plotted. Stiffness of the parts as given by the slope of the linear region of the stress-strain curve is seen in Table 5.6. The stress-strain curves are consistent for all of the samples as seen in Figure 5.20 and 5.21 which shows repeatability of the fabrication process and constant reproduction of mechanical properties in the fabricated parts. Average compressive stiffness, compressive strength and maximum load data of the parts are given in Table 5.6.

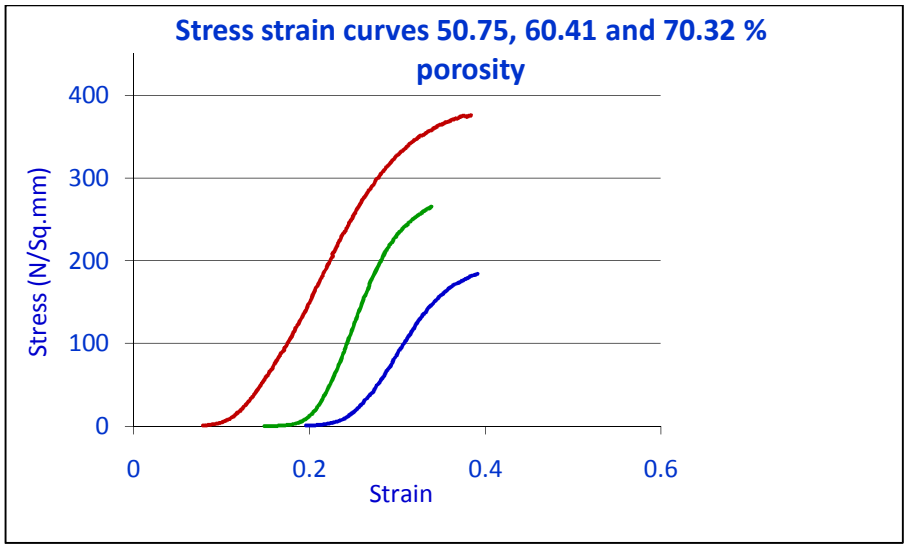


Figure 5. 20 Stress strain curves 50.75, 60.41 and 70.32 % porosity

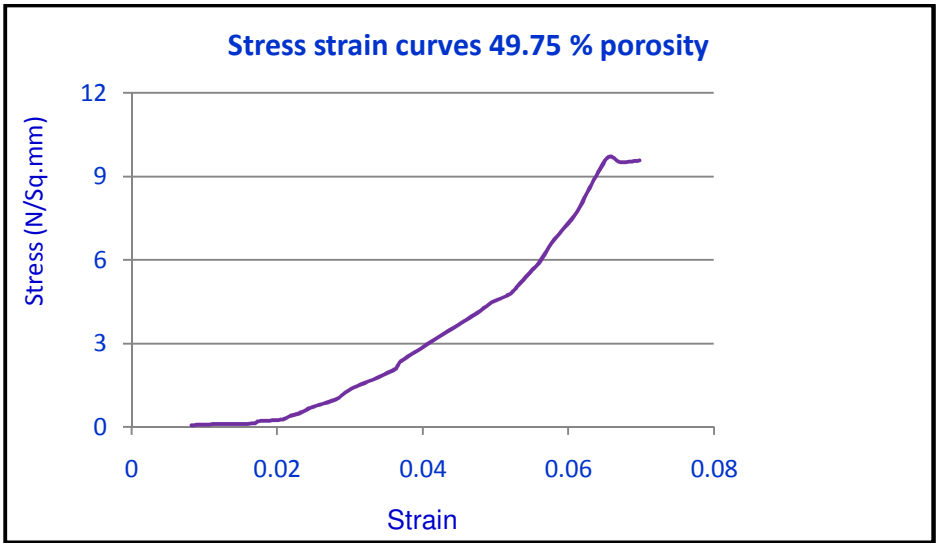


Figure 5. 21 Stress strain curves 49.75 % porosity

Average compressive stiffness and compressive strength of the parts as calculated are given in Table 5.6.

Table 5. 6 Compressive stiffness and compressive strength and maximum load of porous titanium parts

Set No.	Porosity	Comp. Stiffness (GPa)	Ultimate Comp. strength (Mpa) σ Max	Maximum Load (N)
1	50.75(± 0.69)	2.92(±0.17)	163.02(±11.98)	36759
2	60.41 (± 0.81)	2.68 (±0.12)	117.05(±5.54)	25224
3	70.32 (+0.63)	2.13 (±0.21)	83.13(±10.25)	18985
4	49.75 (±1.00)	0.57(±0.05)	7.28(±0.93)	1506

The effective modulus of the parts as obtained from the compression tests were compared with values obtained using Ashby and Gibson's formula (Ashby, M. F., & Gibson, L., 1988)

$$E_{eff} = E\,(q_{rel})^{2}$$

where, E = Elastic modulus of the solid structure, q rel = relative density of the cellular structure, E eff = Elastic modulus of the cellular structure. Compressive strength for similar porosities were predicted using the Ashby's and Gibson's formula

$$\sigma = 940\,(p/p0)^{3/2} \qquad (5)$$

Variation of compressive stiffness and ultimate compressive strength (σ_{max}) with variation in porosity is depicted in Figures 5.19 and 5.20. It is observed that both compressive stiffness and σ_{max} decrease with an increase in porosity consistent with expectations for cellular solids (Ashby, M. F.,& Gibson., 1988). However, there is a more significant drop in compressive strength as compared to compressive stiffness. From Figures 5.22 and 5.23 it is observed that both numerical values of elastic modulus and stiffness calculated using Ashby and Gibson's formula were much higher than the experimentally observed values of the compressive stiffness and strength for the porous parts.

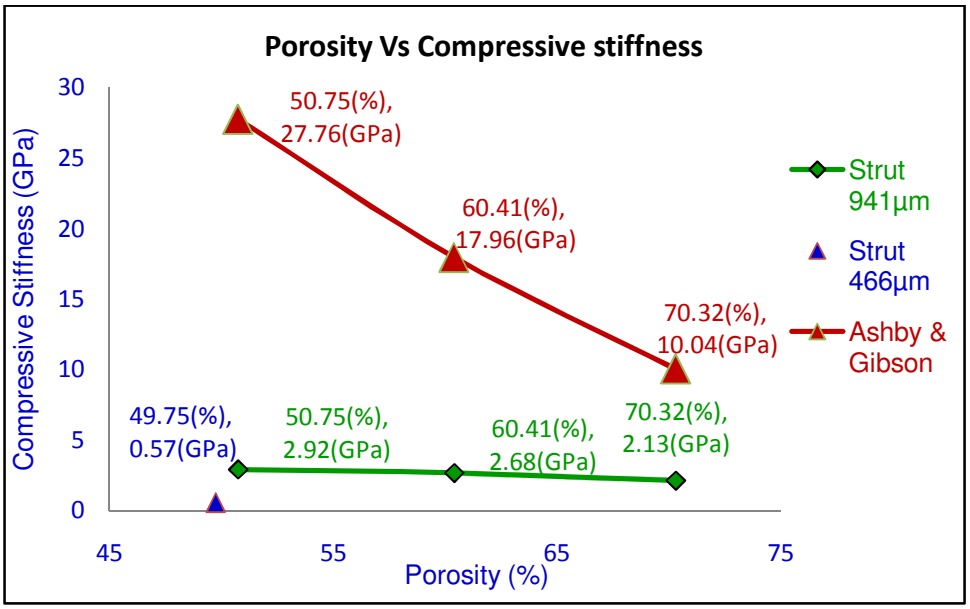


Figure 5. 22 Porosity Vs Compressive stiffness

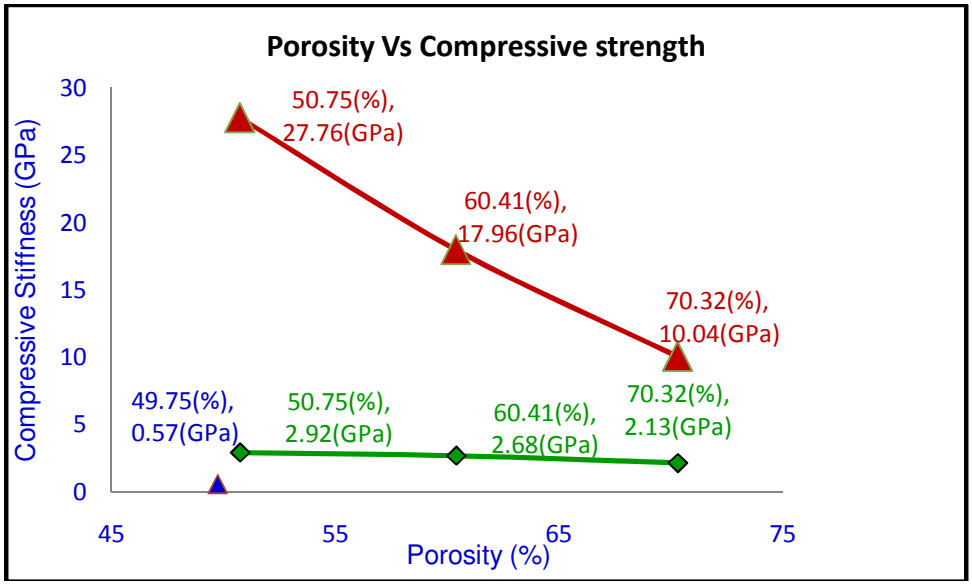


Figure 5. 23 Porosity Vs Compressive strength σ_{max}

An interesting observation is that for nearly the same porosity values, the compressive stiffness and compressive strength decreased significantly with reduction of the strut size and increase in the number of pores (Figure 5.22 and 5.23). These samples have

almost similar porosities (50.75 and 49.75%) but the strut size is reduced from 941µm to 466µm and the numbers of pores were increased from 7 to 10, volume of the cubic part remaining nearly the same. Similar compression tests show that the compressive stiffness reduces from 2.92GPa to 0.57GPa (80.5% reduction). The compressive strength reduced from 163.02MPa to 7.28MPa (93.54% reduction) in these samples suggests that mechanical properties especially the strength depends on the strut size apart from the porosity. The other contributing factor to these observations could be the possibility of increased structural variations in smaller strut sizes that result in thin structures that could cause failure at lesser loads.

In this study Ti6Al4V parts with porosities ranging from 49.75–70.32% were produced. Stiffness of the fabricated parts ranged from 0.57GPa to 2.92GPa. Parts with porosity as high as 70.32% with a stiffness of 2.13GPa were successfully fabricated. Assuming the density of cortical bone and trabecular bone to be 2 and 0.3g/cm^3 respectively, an equivalent volume of 15X15X15mm cubic part of cortical and trabecular bone would weigh 6.75 and 1.01g respectively. Weight of the fabricated porous titanium parts was found to range from 6.03 - 3.92g (Table 5.5) which is within acceptable limits of the part replaced.

Shear Testing

On removal of the fixture and the part from the shear testing apparatus it was observed that the epoxy was not affected and the part was still adherent to the fixture. The shear was, for the most part, straight across the middle but it did not make it all the way across. The layer that sheared almost all the way across had a greater resistance to shear stress than the leftmost columns of titanium had to the now pure bending force

being applied Figure 5.24. A point of interest is that the far left side did not shear as the rest of the piece. This proves that the piece is not being broken by one of its weak layers simply being peeled off. The layer that sheared almost all the way across had a greater resistance to shear stress than the leftmost columns of titanium had to the now pure bending force being applied. In all the cases a clean shear was not seen all the way across one layer of the electron beam melted part. This shows that parts produced by electron beam melting do not tear apart because of a weak connection between the layers fused one over the other.

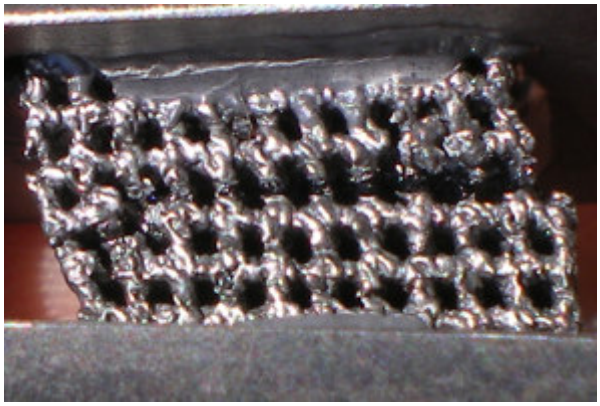


Figure 5. 24 Sheared part within the fixture

As in the compression test stress strain curves were plotted from the force displacement data collected. Shear modulus was the slope of the linear region of the stress strain curve.

Average values of shear modulus for the three specimens was 239.25, 254.62, 201.28, and 328.23 (MPa) respectively for set 1, 2, 3, and 4 as seen in Figure 5.25.

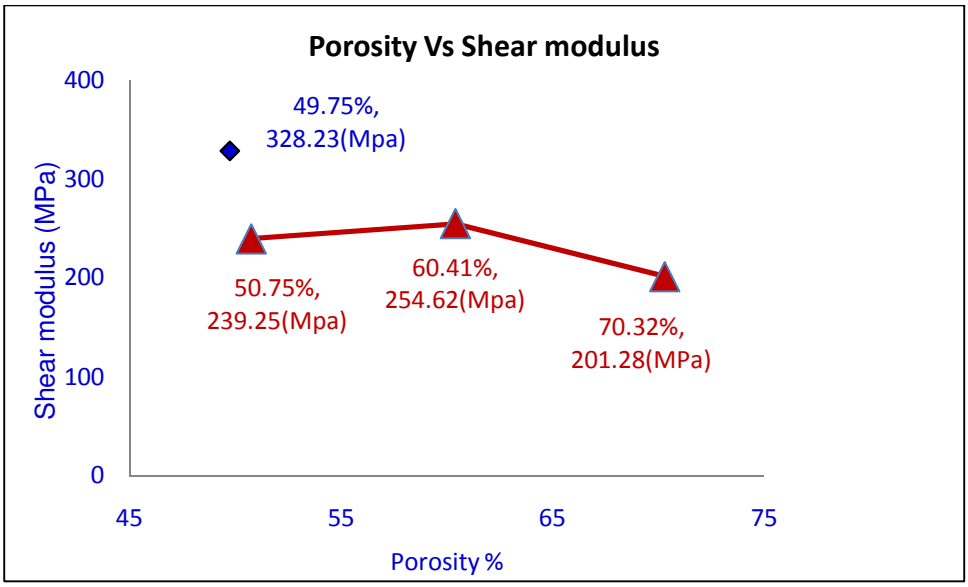


Figure 5. 25 Porosity Vs Shear modulus

5.6 Discussion

Mechanical properties such as elastic modulus and maximum compressive strength of cortical and trabecular bone varies with the anatomical site, age, loading direction and sex. Table 5.7 shows the characteristics of cortical bone and mandible trabecular bone as cited from literature (Misch C. E., et al 1999; Peterson J and Dechow P., 2003; Peterson J., and Dechow P., 2003; Dabney C.L.S and Dechow P.C., 2003; Ashman R.B., Reilly D.T., and Burstein A.H., 1975;). Porous Ti6Al4V structures fabricated with thicker struts (941µm) having porosities of 50.75, 60.41 and 70.32% had stiffness of 2.92(+ 0.17), 2.68 and 2.13 (+0.21)GPa respectively. These values fall between the elastic modulus range for cortical bone and trabecular bone seen in Table 5.7. The σ_{max} of the sample set 1(50.75%) porous structures was 163.02(+11.98) MPa which is close to that of cortical bone. The sample set 2(60.42%) porous structures had a compressive strength (σ_{max}) of 117.05(+5.54) MPa. These values tally well with those obtained by Heinl et al (2008). They have reported porous structures (59.75%) produced with

selective laser beam melting with a σ_{max} of 148.4(+3.5) and 127.1(+29.2)MPa in the parallel and perpendicular loading directions. In this study, structures with thinner struts of 466μm (sample set 4) had a stiffness of 0.57(+0.05) GPa and a σ_{max} of 7.28(+0.93) MPa which are close to that of mandibular trabecular bone stiffness (0.56GPa) (Table 5.7). However, these structures failed at much higher loads (Table 5.6) as against the masticatory load of a maximum of 300N seen in the molar region of the mandible (Wang, D., et al 2005). Structures with thicker struts and porosities in the range of 50 – 70% with stiffness values varying from 2.92 - 2.13GPa withstanding a maximum load of 36,759N could be used in load bearing regions such as the mandible cortical bone and dental abutment reconstruction regions. Structures with thinner struts with stiffness of .57GPa could be used for replacement of trabecular bone and non load bearing applications such as in cranial replacement.

From Figure 5.22, it is seen that the differences between the theoretically observed effective stiffness calculated using Ashby and Gibson's formula and the experimentally observed values can be attributed to the size of the blocks (15mm x 15mm x 15mm) used for the experiments. The theoretically formulation assumes a block with an infinite number of pores. This is nearly impossible to replicate in the EBM manufacturing process due to process, time and financial constraints. More importantly, any craniofacial or mandibular implant will have a finite amount of pores built into the implant. The differences in theoretical and experimentally observed values can also be attributed to the melting of titanium alloy powder at high temperatures and subsequent solidification by cooling that causes unevenness of the surface leading to cell surface curvatures and corrugations as seen in the SEM studies

(Figure 5.11b). These curvatures and corrugations of the cell surface result in local heterogeneities and stress concentrations which affect the peak stress as reported by Simone and Gibson et al (1998). Such deformations through the entire specimen also lead to early failure of the thinner struts and results in reduced stiffness and strength of the metallic porous structures. Similar reduction in compressive stiffness and strength in aluminum foams made from irregularly shaped sea salt preforms that had irregular architecture and less clearly defined struts has been reported by Marchi et al (2000). We have therefore chosen to use the experimentally observed effective stiffness and ultimate strength values to aid us in the design of the implants.

The strut sizes were found to be 941 (+/-17.1), 905 (+/-16.9), 882 (+/-13.2)μm as against the intended design size of 800μm for sample set 1-3 respectively. Consequently, the designed pore sizes are observed to reduce from 1230, 1570, 2040μm, to 1020 (+/- 45.0), 1424(+/- 42.1), 1960 (+/-49.4). The differences between the observed dimensions to the intended design dimension reduce considerably with increase in pore sizes. As the pore dimensions become relatively small (<400μm), Ti6Al4V particles may get clogged within the pores, thereby reducing the effective pore dimension. However, the deviations within each sample set were minimal indicating the consistency of the fabrication process (Table 5.3). Differences observed between the intended design and observed values for the dimensions of the pore and struts of the fabricated parts are attributed to the surface irregularities and lack of a smooth finish in the fabricated parts. The size of the titanium particles present within the bed of the EBM system will significantly influence the final dimensional values of

the parts. Smaller size titanium particles will help to alleviate the differences in dimensional values.

Table 5. 7 Elastic modulus and maximum compressive strength of cortical and trabecular bone

Material	E(GPa)	σ_{max} (MPa)	Ref
Mandible trabecular Bone	0.56	3.94	Misch et al (1999)
Cranial vault & Zygoma (MBB) bone	12.5	-	Peterson and Dechow (2003a)
Cranial vault & Zygoma (NMBB) bone	13.0	-	Peterson and Dechow (2003a)
Parietal	11.8	-	Peterson and Dechow (2003b)
Mandible	12.7	-	Dabney and Dechow(2003)
Tibia	11.6	-	Ashman R B(1982)
Femur	18.2	205 ($\pm$17.3)	Reilly and Burstein(1975)

From Table 5.7, it is seen that for structures with porosities of 50.75, 60.41 and 70.32%, the stiffness values were 2.92($\pm$0.17), 2.68 ($\pm$0.12) and 2.13 ($\pm$0.21)GPa showing that compressive stiffness reduces with increase in porosity and pore sizes. Similar observations are also made with compressive strength. However for a small variation of porosity of 1% created by reducing the strut size from 941 (+/-17.1) to 466 (+/- 39.7)µm the compressive stiffness and strength drops down to 0.57($\pm$0.05)GPa and 7.28($\pm$0.93)MPa respectively despite the grain density being 4.42 (+/- 0.14)g/cm^3 which is equal to that of dense titanium. The cellular structure is similar to a cubic truss. Mechanical properties such as stiffness and strength therefore depend on the cross section and length of the individual truss structures and the distance between them. These observations show that the mechanical properties not only depend on overall porosity but also on the dimension of the solid structures and pore sizes.

Similar observation of the reduction in elastic modulus from 2.9 to 1.2GPa and maximum load from 289kN to 200kN when the strut diameter was reduced from 3.2 to 2.9 mm have been made by Li et al (2008) using cast Ti6Al4V octet truss lattice structures. The researchers fabricated Ti6Al4V octet truss lattice structures with struts having diameters of 3.2 and 2.9 mm and porosities of 84 and 86.9% respectively. Similar to our studies, they have observed a drop in elastic modulus and maximum strength from 2.9 to 1.2GPa and 31 to 22MPa respectively.

Titanium reconstruction plates presently used for mandibular and dental reconstruction do not conform to the exact morphology of the mandible and therefore do not possess pleasing aesthetic qualities. Electron beam melting as a net shaped manufacturing process can open up new design solutions for mandibular implants with a porous region to replace the bone structure and an inbuilt dense metal for the placement of fixed prosthodontic restorations. This may lead to improved masticatory functions and verbalization. Since the stiffness of the parts is reduced to match that of the surrounding natural tissue, stress shielding effects can be minimized considerably.

In this chapter fabrication of porous Ti6Al4V parts with porosities ranging from 49.75 – 70.32 % with an electron beam based rapid manufacturing process is discussed. Structures with pore sizes ranging from 765 – 1960μm and strut sizes of 466 – 941μm that facilitate tissue ingrowth were fabricated. Effect of variation of pore and strut sizes on the mechanical properties of porous titanium structures have been studied. External characterization of the samples using SEM studies showed complete melting of titanium with no interlayer bonding differences. Micro CT studies showed well defined struts throughout the lattice structure. Grain density of the porous

titanium structures was found to be 4.423g/cm3 equivalent to that of dense Ti6Al4V. Compression tests of the samples showed effective stiffness values ranging from 0.57 (+0.05) – 2.92(+0.17)GPa and compressive strength values of 7.28(+0.93) - 163.02(+11.98)MPa. For nearly the same porosity values of 49.75% and 50.75% with a variation in the strut thickness, the compressive stiffness and strength decreased significantly from 2.92GPa to 0.57GPa (80.5% reduction) and 163.02MPa to 7.28MPa (93.54% reduction) respectively showing that strength of the lattice structure depended on the geometrical dimensions of the solid struts apart from the overall porosity values. Mechanical strength studies indicate the fabricated structures with porosities as high as 50-70% satisfy the mechanical strength requirements needed for craniofacial applications.

CHAPTER 6

6. CONCLUSION, RESEARCH CONTRIBUTIONS AND SCOPE OF FUTURE WORK

6.1 Conclusion

A design strategy has been developed for the eventual direct fabrication of titanium implants for cranial and mandibular reconstruction with mechanical properties close to that of bone. Advantages of this design strategy are preparation of custom porous titanium implants with controlled mechanical properties. With the predicted mechanical properties, masticatory and other functions of the mandible can be tested and implants with better longevity fabricated. Patients requiring mandibular reconstruction would have better aesthetics and functions with this new innovative design of implants. The design of implants would conform to the external geometry, and have mechanical properties close to parts replaced. Provision for post operative dental rehabilitation would enhance the functional value.

In this study porous Ti6Al4V parts with porosities ranging from 49.75 – 70.32 % were fabricated using EBM. Structures with pore sizes ranging from 765 – 1960 µm and strut sizes of 466 – 941 µm that facilitate tissue ingrowth were fabricated. Then, the effect of variation of pore and strut sizes on the mechanical properties of porous titanium structures with small pore sizes was studied. External, internal characterization and analysis was done using optical microscopy, SEM and Micro CT.

Mechanical properties as porosity, grain density compressive and shear, stiffness and strength were assessed and evaluated for use in craniofacial applications.

The study showed EBM as a promising process for direct fabrication of patient specific custom implants with predictable mechanical properties. Implants fabricated in this manner using medical imaging technologies and advanced manufacturing technologies as metal RP technologies would satisfy the need to have highly porous lighter implants with high mechanical strength using the least amount of metal as preferred by surgeons. Patients requiring craniofacial reconstruction would have implants with improved aesthetics and functionality with this new innovative method of fabrication. The mechanical properties within the implant can also be varied according to the requirements of the anatomical region of implantation. This innovative concept can be applied to the design of custom implants for other parts of the body as well.

6.2 Research Contributions

A general design strategy has been developed for the eventual direct fabrication of titanium implants for cranial mandibular reconstruction with mechanical properties close to that of bone. Advantages of this design strategy are preparation of custom porous titanium implants with controlled mechanical properties that can also be varied according to the anatomical region of implantation. With the predicted mechanical properties, masticatory and other functions of the mandible can be tested and implants with better longevity can be fabricated.

A methodology for fabrication of mandibular implants that would have better aesthetics and improved masticatory functions therefore enhance patient comfort and compliance has been developed.

EBM has been evaluated as a suitable method for consistent fabrication of net shaped porous titanium structures with controlled porosity for use in craniofacial applications leading to the direct fabrication of craniofacial implants reducing lead time and cost.

Relationship of mechanical properties and strength to the overall porosity and also to the dimension of the solid structures and pore sizes has been made.

6.3 Scope for future work

Future work in this area could be directed towards taking this research from the laboratory to making this a technology available for the surgeon's everyday clinical use.

1. Fabrication patient specific porous titanium implants and evaluation of mechanical properties simulating real time scenarios as mastication and fatigue testing.
2. In vitro and in-vivo evaluation of tissue in growth in porous titanium structures fabricated with additive manufacturing.
3. Surface modifications as plasma coating and ion beam irradiation/deposition for enhancement of osseointegration
4. Evaluation of advantages and disadvantages EBM and other Laser based metal rapid prototyping methods as applicable to fabrication of porous implants in relation to mechanical properties, overall cost, and lead time.

REFERENCES

1. Aksakal, B., Yildrim, O. S., & Gul, H. (2004). Metallurgical failure analysis of various implant materials used in orthopedic applications. *Journal of failure analysis and prevention , 4* (3), 17-23.

2. Albrektsson, T., Br~nemark, P.-I., Hansson, H. A., Kasemo, B., Larsson, K., LundstrOm, I., et al. (1983). The interface zone of inorganic implants in vivo: titanium implants in bone. *Annals of Biomedical Engineering , 11*, 1-27.

3. Anup, S., Sivakumar, S. M., & Suraishkumar, G. K. (2007). Natural optima in human skull: a low-velocity impact study. *International Journal of Crashworthiness , 12* (1), 17-20.

4. Ashby, M. F., & Gibson. (1988). *Cellular Solids: Structures and Properties.* Pergamon Press.

5. Ashman R.B. (1975). *Ultrasonic determination of the elastic properties of cortical bone:techniques and limitations.* New Orleans: Tulane University.

6. Barranco, V. P., & Soloman, H. ". (1972). Eczematous dermatitis from nickel. *Journal of American Medical Association , 220* (9), 1244.

7. Black, J. (1996). *Prosthetic materials.* New York: VCH Publishers .

8. Brånemark, P.-I., Hansson, B. O., Adell, R., Breine, U., Lindström, J., Hallén, O., et al. (1977). *Osseointegrated implants in the treatment of the edentulous jaw.* Stockholm: Almqvist and Wiksell, 132.

9. Chen, J. J., Liu, W., Li, M. Z., & Wang, C. T. (2006). Digital manufacture of titanium prosthesis for cranioplasty. *International Journal of Advanced Manufacturing Technology , 27*, 1148–1152.

10. Connell, H., Statham, P., Collie, D., Walker, F., & Moos, K. (1999). Use of a template for custom cranioplasty. *Phidias – EC Funded Network Project on Rapid Prototyping in Medicine* (2), 7-8.

11. Cormier, D., Harrysson, O., & West, H. (2004). Characterization Of High Alloy Steel Produced Via Electron Beam Melting. *Rapid Prototyping Journal , 10* (1), 35-41.

12. Cormier, D., West, H., Harrysson, O., & Knowlson, K. (2004). Characterization of thin walled Ti-6Al-4V components produced via electron beam melting. *Solid Freeform Symposium Austin Texas* , (pp. 440-447).

13. Cox, T., Kohn, M., & Impelluso, T. (2003). Computerized Analysis of Resorbable Polymer Plates and Screws for the Rigid Fixation of Mandibular Angle Fractures. *Int J of Oral Maxillofac Surg , 61*, 481–487.

14. Dabney, C. L., & Dechow, P. C. (2003). Variations in cortical material properties throughout the human dentate mandible. *American Journal of Physical Anthropology , 120*, 252–277.

15. Datti, R., Cavagnaro, G., & Camici, S. (1985). Stainless steel wire mesh cranioplasty: Ten years' experience with 183 patients (100 followed up). *Acta Neurochirurgica* , 3-4.

16. Dean, D., Min, K. J., & Bond, A. (2003). Computer aided design of large format prefabricated cranial plates. *The Journal of Craniofacial Surgery* , 819-832.

17. D'Urso, P. S., Earwaker, W. J., T, B. M., Redmond, J. M., Thompson, J. R., Effeney, D. J., et al. (2000). Custom cranioplasty using stereolithography and acrylic. *British Journal of Plastic Surgery , 53*, 200–204.

18. Eufinger, H., Rasche, C., J, L., M, W., Weihe S Schmitz, I., Schiller, C., et al. (2007). "Performance of functionally graded implants of polylactides and calcium phosphate/calcium carbonate in an ovine model for computer assisted craniectomy a. *Biomaterials* , 475–485.

19. Fernandez, J., Gallas, M., Burguera, M., & Viano, J. (2003). A Three-Dimensional Numerical Simulation of Mandible Fracture Reduction With Screwed Miniplates. *Journal of Biomechanics , 36*, 329–337.

20. Grant, G. A., Jolley, M., Ellenbogen, R., Roberts, T. S., Gruss, J. R., & Loeser, J. D. (2004). Failure of autologous bone-assisted cranioplasty following decompressive craniectomy in children and adolescents. *Journal of Neurosurgery-Suppl Pediatrics , 100* (2), 163-8.

21. Griffith, M. L., Ensz, M. T., Puskar, J. D., Robino, C. V., Brooks, J. A., Philliber, J. A., et al. (2000). Understanding the microstructure and properties of components fabricated by Laser Engineered Net Shaping (LENS). *Materials Research Society Symposium - Proceedings*, (pp. 9-20).

22. Hallab, N. J., Urban, R. M., & Jacobs, J. J. (2004). Corrosion and biocompatibility of orthopedic materials. In M. J. Yaszemski, D. J. Trantolo, K. U. Lewandrowski, D. E. Altobelli, & D. L. Wise, *Biomaterials in orthopedics.* ": Marcel Dekker Inc.

23. Halpin, D. S. (1975). An unusual reaction in muscle in association with Vitallium plate: a report of possible metal hypersensitivity. *Journal of Bone and Joint Surgery of Britain , 57* (4), 451-3.

24. Harrysson, O., & Cormier, D. R. (2003). "Direct Fabrication of Custom Orthopedic Implants Using Electron Beam Melting Technology. In E. D. 9780470016886 (Ed.), *Advanced Manufacturing Technology for Medical Applications* (pp. 191-206).

25. Harrysson, O., Cansizoglu, O. D., & West, H. A. (2007). Direct metal fabrication of titanium implants with tailored materials and mechanical properties using electron beam melting technology. *Material Science Engineering* , doi:10.1016/j.msec..04.022.

26. Harrysson, O., Deaton, B., Bardin, J., West, H., Cansizoglu, O., Cormier, D., et al. (2005). Evaluation of Titanium Implant Components Directly Fabricated Through Electron Beam Melting Technology. *Advanced materials and processes , 163* (7), 72-77.

27. Hayashi, T., Maekawa, K., Tamura, M., & Hanyu, K. (2005). Selective Laser Sintering Method Uisng Titanium Powder Sheet Toward Fabrication of Porous Bone Substitutes. *JSME International Journal, Series A Solid mechanics and material Engineering , 48* (4), 369-75.

28. He, J., Dichen, L., Bingheng, L., Zhen, W., & Zhang, T. (2006a). Custom fabrication of a composite hemi-knee joint based on rapid prototyping. *Rapid Prototyping Journal , 12* (4), 198–205.

29. He, Y., Ye, M., & Wang, C. A. (2006b). Method in the design and fabrication of exact-fit customized implant based on sectional medical images and rapid prototyping technology. *International Journal of advanced Manufacturing Technology , 28*, 504-508.

30. Heinl, P. M., Muller, L. A., Körner, C., Singer, R. F., & Muller, F. A. (2008). Cellular Ti-6Al4V structures with interconnected macroporosity for bone implants fabricated by selective electron beam melting. *Acta Biomateralia , 4*, 1536-1544.

31. Heinl, P., Rottmair, A., Körner, A., & Singer, R. F. (2007). Cellular titanium by selective electron beam melting. *Advanced Engineering Materials , 9* (5), 360 – 364.

32. Hieu, L. C., Bohez, E., Stolen, J. V., Phien, H. N., Vatcahraporn, E., Binh, P. H., et al. (2003). Design for medical rapid prototyping of cranioplasty implants. *Rapid Prototyping Journal , 9* (3), 175-186.

33. Hollister, S. J., CY, L., Satio, E., Schek, R., Taboas, J., Willams, J., et al. (2005). Engineering craniofacial scaffolds. *Orthodontic Craniofacial Research , 8*, 162-173.

34. Itokawaa, H. T., Hiraideb, M., Moriyaa, M., Fujimotoa, Nagashimaa, G., Suzukia, R., et al. (2007). A 12 month in vivo study on the response of bone to a hydroxyapatite–Polymethylmethacrylate cranioplasty composite. *Biomaterials , 28*, 4922–4927.

35. Jacobs, J. J., Gilbert, J. L., & Urban, R. M. (1998). Corrosion of metal orthopedic implants. *Journal of Bone and Joint Surgery , 80*, 268-282.

36. Jasty, M., Maloney, W. J., Bragdon, C. R., O'Connor, D. O., Zalenski, E. B., & Harris,
37. W. H. (1991). The initiation of failure of cemented femoral components of hip arthroplasties. *Journal of Bone Joint Surgery , 73B*, 551–558.

38. Kalinyuk, A. N., Trigub, N. P., Zamkov, V. N., Ivasishin, O. M., Markovsky, P. E., Tovich, R. V., et al. (2003). Microstructure,texture and mechanical properties of electron beam melted Titanium. *Materials Science and Engineering A , 346*, 178-188.

39. Khan, S. N., Tomin, E., & Lane, J. M. (2000). Clinical applications of bone grafts substitutes. *Tissue Engineering in Orthopedic Surgery , 31*, 389-398.

40. Kindt–Larsen, T., Smith, D. B., & Jensen, J. S. (1995). Innovations in acrylic bone cement and application equipment. *Journal of Applied Biomaterials* , 75–83.

41. Knoll, W., Gaida, A., & Maurer, P. (2006). Analysis of mechanical stress in reconstruction plates for bridging mandibular angle defects. *J. Craniofac surg , 34*, 201-209.

42. Kotan, G., & Bor, S. A. (2007). Production and Characterization of High Porosity Ti-6Al-4V Foam by Space Holder Technique in Powder Metallurgy. *Turkish Journal of Engineering Environmental Science , 1*, 149 – 156.

43. Kraay, M. J., Thomas, R. D., Rimnac, C. M., J, F. S., & and Goldberg, V. M. (2006). Zirconia versus Co-Cr femoral heads in total hip arthroplasty: early assessment of wear. *Clinical Orthopedic Related Research , 453*, 86-90.

44. Kruth, J.-P., Mercs, P., Vaerenbergh, J. V., Froyen, L., & Rombouts, M. (2005). Binding mechanisms in selective laser sintering and selective laser melting. *Rapid Prototyping Journal , 11* (1), 26–36.

45. Kummailil, J., Sammarco, C., S. D., Brown, C. A., & Rong, K. (2005). Effect of Select lens TM processing parameters on the deposition of Ti-6AI-4V. *Journal of Manufacturing Processes , 11* (1), 42-50.

46. Lane, H. S., & Sandhu, J. M. (1987). Current approaches to experimental bone grafting. *Orthopedic Clinics of North America , 18*, 213-225.

47. Laoui, T., Santos, E., Osakada, K., Shiomi, M., Morita, M., Shaik, S. K., et al. (2004). Properties of Titanium implants made by Laser processing. In M. Geiger, & Otto A (Ed.), *Laser Net Shape Engineering, Proceedings of LANE,* , (pp. 475-484).

48. Lara, W., Schweitze, r. J., Rodney, P., Odum, B. C., Edlich, R. F., & Gampper, T. J. (1998). Technical considerations in the use of polymethylmethacrylate in cranioplasty. *Journal of Long-Term Effects of Medical Implants , 8* (1), 43-53.

49. Levi, A., Choi, W., Keller, P., Heiserman, J., Sonntag, V., & Dickman, C. (1998). The radiographic and imaging characteristics of porous tantalum implants within the human cervical spine. *Spine , 23*, 1245–1250.

50. Levine, B. R., Sporer, S., Poggie, R. A., Valle, C. J., & Jacobs, J. J. (2006). Experimental and clini cal performance of porous tantalum on orthopedic surgery. *Biomaterials , 27* (27), 4671-4681.

51. Lewis, G. (1997). Properties of acrylic bone cement: State of the Art Review. *Journal of Biomedical Materials Research, Applied Biomaterials , 38* (2), 155 – 182.

52. Li, J. P., Wijn, J. R., Blitterswijk, C. A., & Groot, K. D. (2006). Porous Ti6Al4V scaffold directly fabricating by rapid prototyping Preparation and in vitro experiment. *Biomaterials , 27*, 1223–1235.

53. Li, J. P., Wijn, J. R., Blitterswijk, C. A., & Groot, K. D. (2005). Porous Titanium scaffolds directly fabricated by 3D fibre deposition technique: Effect of nozzle diameter. *Journal Of Materials Science: Materials In Medicine , 16*, 1159 – 1163.

54. Li, J., H., L. S., Van Blitterswijk, C., & De Groot, K. (2006). Cancellous bone from porous Titanium by multiple coating technique. *Journal Of Materials Science: Materials In Medicine , 17*, 179– 185.

55. Li, J., Li, S., De Groot, K., & Layrolle, P. (2002). Preparation and characterization of porous titanium. *Key Engineering Materials , 218-220*, 51-54.

56. Li, J., Wijn, J., Van Blitterswijk, C., & De Groot, K. (2007). Comparison of porous Titanium made by sponge replication and directly 3D fiber deposition and cancellous bone. *Key Engineering Materials , 330-332* (2), 999-1002.

57. Li, L., Blake, F., Heiland, M., Schmelzle, R., & Pohlenz, P. (2007). Long-Term evaluation after mandibular reconstruction with fibular grafts versus microsurgical fibular Flaps. *Journal of Oral and Maxillofacial Surgery , 65* (2), 281-286.

58. Lijian, Z., Sheng, C. T., Wei, W., & Lei, C. (2000). Study of commercially pure titanium implants bone, integration, mechanism. *European Journal of Plastic Surgery , 23*, 301–304.

59. Lin, C. Y., Wirtz, T., LaMarca, F., & Hollister, S. J. (2007). Structural and mechanical evaluations of a topology optimized titanium interbody fusion cage fabricated by selective laser melting process. *Journal of Biomedical Materials Research - Part A , 83* (2), 272-9.

60. Lopez-Heredia, M. A., Goyenvalle, E., Aguado, E., Pilet, P., Leroux, C., Dorget, M., et al. Bone growth in rapid prototyped porous titanium implants. *Journal of Biomedical Materials Research Part A , 85 A* (3), 664 - 673.

61. Lovald, S., Khraishi, T., Wagner, J., Baack, B., Kelly, J., & Wood, J. (2006). Comparison of Plate-Screw Systems Used in Mandibular Fracture Reduction: Finite Element Analysis. *Journal of Biomechanical Engineering , 128*, 654 – 656.

62. Marchi, C. S., Despois, J. F., & Mortensen, A. (2000). Fabrication and compressive response of open-cell aluminum foams with sub-millimeter pores,. In T. a. Clyne (Ed.), *Euromat Vol 5,* (pp. 34-39). Wiley-VCH V.

63. Martin, P. J., J, O. M., & Hayden, R. E. (1994). Free tissue transfer in oromandibular reconstruction. Necessity or extravagance? *Otolaryngological Clinics of North America , 27* (6), 1141-50.

64. Martola, M., Lindqvist, C., Hann, u. H., & J., A.-S. (2007). Fracture of Titanium Plates Used for Mandibular Reconstruction Following Ablative Tumor Surgery. *Journal of biomedical materials research. Part B, Applied biomaterials , 80* (2), pp. 345-52.

65. Matsuno, A., Tanaka, H., Iwamuro, H., Takanashi, S., Miyawaki, S., Nakashima, M., et al. (2006). Analyses of the factors influencing bone graft infection after delayed cranioplasty. *Acta Neurochirgery , 148*, 535–540.

66. Maurer, P., Holweg, S., & Schubert. (1999). Finite-Element-Analysis of different screw-diameters in the sagittal split osteotomy of the mandible. *J Cranio Maxillofac Surg , 27*, 365-372.

67. Ming, Y. L., Chang, C. C., Lin, C. C., Lo, L. J., & Chen, Y. R. (2002). Custom implant design for patients with cranial defects. *Engineering in Medicine and Biology Magazine, IEEE , 21* (2), 38 – 44.

68. Misch C. E., Q. Z. (1999). Mechanical Properties of Trabecular Bone in the Human Mandible: Implications for Dental Implant Treatment Planning, and Surgical Placement. *J Oral Maxiilofac Surg , 57*, 700-706.

69. Moncler, S., Salama, H., Reingewirtz, Y., & Dubruille, J. (1998). Timing of Loading and Effect of Micromotion on Bone–Dental Implant Interface: Review of Experimental Literature. *Journal of Biomedical Material Research , 43* (2), 192-203.

70. Nam, J., Starly, B., Darling, A., & S, W. (2004). Computer aided tissue engineering for modeling and design of novel tissue scaffolds. *Computer Adided Design and Applications , 1* (1-4), 633-40.

71. Park, J. B., & Lakes, R. S. (1992). *Biomaterials and introduction.* New York: Plenum.

72. Parthasarathy, J., & and Parthiban, J. K. (2008). Rapid Prototyping in Custom Fabrication of Titanium Mesh Implants for Large Cranial Defects. *RAPID 2008, May 20–22.* Lake Buena Vista, FL, USA: Society of Manufacturing Engineers,.

73. Parthasarathy, J., Starly, B., & Raman, S. (2009). Computer Aided Bio-modeling and Analysis of Patient Specific Porous Titanium Mandibular Implants . *Journal of Medical Devices* .

74. Parthasarathy, J., Starly, B., & Raman, S. (2008). Design of Patient-Specific Porous Titanium Implants for Craniofacial Applications. *RAPID 2008 May 20-22. TP08PUB116.* Lake Buena Vista, FL, USA: Society of Manufacturing Engineers.

75. Peterson, J., & Dechow, P. (2003). Material properties of the human cranial vault and zygoma. *The anatomical record part A* , 785-797.

76. Peterson, J., & Dechow, P. (2003). Material properties of the parietal bone. *The anatomical record part A , 268*, 7-15.

77. Rack, H. J., & Qazi, J. I. (2006). Titanium alloys for biomedical applications. *Material Science and Engineering,C, Biomimetic materials and, sensors and systems , 26*, 8.

78. Rajagopalan, S., & Robb, R. A. (2006). Schwarz meets Schwan: Design and fabrication of biomorphic and durataxic tissue engineering scaffolds. *Medical Image Analysis , 10b*, 693-712.

79. Robertson, D. M., Pierre, L., & Chahal, R. (1976). Preliminary observations of bone ingrowth into porous materials. *Journal of Biomedical Materials Research , 10*, 335–44.

80. Ryan, G., Pandit, A., & Apatsidis, D. (2006). Fabrication methods of porous metals for use in orthopedic applications. *Biomaterials , 27*, 2651–2670.

81. Samman, N., Luk, W., Chow, T., Cheung, L., Tideman, H., & Clark, R. (1999). Custom made titanium mandibular reconstruction tray. *Australian Dental Journal , 44* (3), 195–9.

82. Schlickewei, W., & Schlickewei, C. (2007). The use of bone substitutes in the treatment of bone defects - The clinical view and history. *Macromolecular Symposia , 253*, 10-23.

83. Shimko, D. A., & Nauman, E. A. (2007). Development and characterization of a porous poly(methyl methacrylate) scaffold with controllable modulus and permeability . *Journal of Biomedical Materials Research - Part B Applied Biomaterials , 80* (2), 360-369.

84. Silber, J. S., Anderson, G. D., Daffner, S. D., Brislin, T. B., Leland, J. M., Hilibrand, A. S., et al. (2003). Donor site morbidity after anterior iliac crest bone harvest for single-level anterior cervical discectomy and fusion. *Spine , 28*, 134 – 139.

85. Simone, A. E., & Gibson, L. J. (1998). The effect of cell face curvature and corrugations on the stiffness and strength of metallic foams. *Acta mater. , 46* (11), 3929-3935.

86. Singare, S., Dichen, L., Bingheng, L., Yanpu, L., Zhenyu, G., & Yaxion, G. L. (2004). Design and fabrication of custom mandible titanium tray based on rapid prototyping. *Medical Engineering & Physics , 26*, 671–676.

87. Singare, S., Yaxiong, L., Dichen, L., Bingheng, L., Sanhu, H., & Gang, L. (2006). Customized design and manufacturing of chin implant based on rapid prototyping. *Rapid Prototyping Journal , 12* (4), 206–213.

88. Singare, S., Yaxiong, L., Dichen, L., Bingheng, L., Sanhu, H., & Gang, L. (2006). Fabrication of customized maxillo-facial prosthesis using computer-aided design and rapid prototyping techniques. *Rapid Prototyping Journal , 12* (4), 206–213.

89. Singh, R., & Dahotre, N. B. (2007). Corrosion degradation and prevention by surface modification of biometallic materials. *Journal of Material Science Material Medicine , 18*, 725–751.

90. Spector, M. (1992). Biomaterial failure. *Orthopedic Clinics of North America , 23*, 211– 29 217.

91. St.John, Vaccaro R, A., Sah P, A., M, S., Berta C, S., Albert, T., et al. (2003). Physical and monetary costs associated with autogenous bone graft harvesting. *American Journal of Orthopedics , 32*, 18 –23.

92. Staffa, G., Nataloni, A., C, C., & Servadei, F. (2007). Custom made cranioplasty prostheses in porous hydroxy-apatite using 3D design techniques: 7 years experience in 25 patients. *Acta Neurochirurgica , 149*, 2.

93. Starly, B., Fang, Z., Wei, S., Shokoufandeh, A., & Regli, W. (2005). Three Dimensional reconstruction for Medical CAD Modelling. *Computer Aided Design and applications , 2* (1-4), 431-438.

94. Starly, B., Gomez, C., Darling, A., Fang, Z., Lau, A., Sun, W., et al. (2003). Computer-aided bone scaffold design: a biomimetic approach. *Proceedings of the IEEE 29th Annual Northeast Bioengineering Conference*, (pp. 172-3).

95. Starly, B., Lau, W., Bradbury, T., & Sun, W. (2006). Internal architecture design and freeform fabrication of tissue replacement structures. *Computer-Aided Design , 38* (2), 115-124.

96. Sumita, M., & Teoh, A. (2004). Durability of metallic materials. In T. S. Hin (Ed.), *Engineering materials for biomedical applications* (pp. 2-2). ISBN981-256-061-0.

97. Taggard, D. A., & Menezes, A. H. (2001). Successful use of rib grafts for cranioplasty in children. *Pediatric Neurosurgery , 34*, 3.

98. Thelen, S., Francois, B., & Catherine, B. L. (2004). Mechanics considerations for microporous titanium as an orthopedic implant material. *Journal of Biomedical Materials Research - Part A , 69* (4), 601-610.

99. Tie, Y., Wang, D. M., Ji, T., Wang, C. T., & Zhang, C. P. (2006). Three dimensional finite element analysis investigating the biomechanical effects of human mandibular reconstruction with autogenous bone grafts. *J CranioMaxillofac Surg. , 34*, 290-298.

100. Tomancok, B., Wurm, G., Holl, K., Trenkler, J., & Pogady, P. (1998). Cranioplasty with computer-generated carbon fibre reinforced plastic implants. *CAR'97. Computer Assisted Radiology and Surgery Proceedings of the 11th International Symposium and Exhibiition,* , (p. 1034).

101. Torontolo, D. J., Gresser, J. D., Wise, D. L., Lewandrowski, K. W., & J, B. K. (2000). Biocompatibility of self reinforced polylactide co glycolide implants. In W. D. L (Ed.), *Biomaterials and Bionengineering Handbook* (pp. 617 - 637).

102. Ueyama, Y., Naitoh, R., A, Y., & Matsumura, T. (1996). Analysis of reconstruction of mandibular defects using single stainless steel A-O reconstruction plates. *Journal of Oral and Maxillofacial Surgery , 54* (7), 858-862.

103. Urban, R. M., Jacobs, J. J., Gilbert, J. L., Skipor, A. K., Hallab, N. J., Mikecz, K., et al. (2003). Corrosion Products Generated from Mechanically Assisted Crevice Corrosion of Stainless Steel Orthopedic Implants. *DOI: 10.1520/STP11169S* .

104. Vaucher, S., Mrelli, E. C., Andre, C., & Beffort, O. (2003). Selective Laser Sintering of Aluminium- and titanium-based composites: processing and characterization. *Physica status solidi. Rapid Research note , 3*, pp. R11-R13.

105. Wang, D., Wang, C., Zhang, X., Xu, & L. (2005). Design and Biomechanical Evaluation of a Custom lateral mandible Titanium Prosthesis. *Engineering in Medicine and Biology Society, IEEE-EMBS 27th Annual International Conference* , 6188-6191.

106. Wang, J. C., Warren, D., Sandhu, H. S., Tam, V., & Delamarter, R. A. (1998). Comparison of Magnetic Resonance and Computed Tomographic Image Quality After the Implantation of Tantalum and Titanium Spinal Instrumentation. *Spine , 23*, 1684-1688.

107. Wang, J.-S., Franze´n, H., Toksvig–Larsen, S., & Lidgren. (1995). The performance of Charnley total hip prostheses. Does vacuum mixing of bone cement affect heat generation/analyses of four cement brands. *Journal of Applied Biomaterials , 6*, 105–108.

108. Wei, S., Darling, A., Starl, B., Nam, J., & Darling, A. (2005). Bio-CAD modeling and its applications in computer-aided tissue engineering. *Computer-Aided Design , 37*, 1097–1114.

109. Wei, S., Starly, B., Darling, A., & Gomez, C. (2004). "Computer aided tissue engineering and application to biomimetic modeling and design of tissue scaffolds. *Biotechnology and Applied Biochemistry , 39*, 49-58.

110. Wettergreen, M. A., Bucklena, B. S., Starly, B., Yuksel, E., Wei, S., & Liebschnera, M. A. (2005). Creation of a unit block library of architectures for use in assembled scaffold engineering. *Computer-Aided Design , 37*, 1141–1149.

111. Williams, J. M., Adewunni, A., Schek, R. M., Flanagan, C. L., Krebsbach, P. H., Feinberg, S. E., et al. (2005). Bone tissue engineering using polycaprolactone scaffolds fabricated via selective laser sintering. *Biomaterials , 26*, 4817-4827.

112. Yaxiong, L., Dichen, L., Bingheng, He, S., & Li, G. (2003). The customized mandible substitute based on rapid prototyping. *Rapid Prototyping Journal , 9* (3), 167–174.

APPENDIX

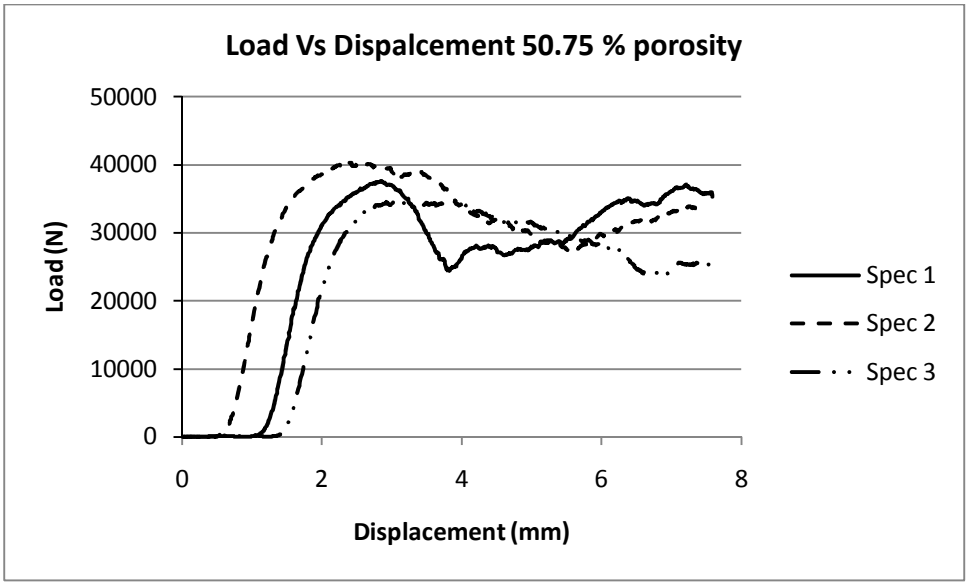


Figure 1 Load Vs Displacement Set 1

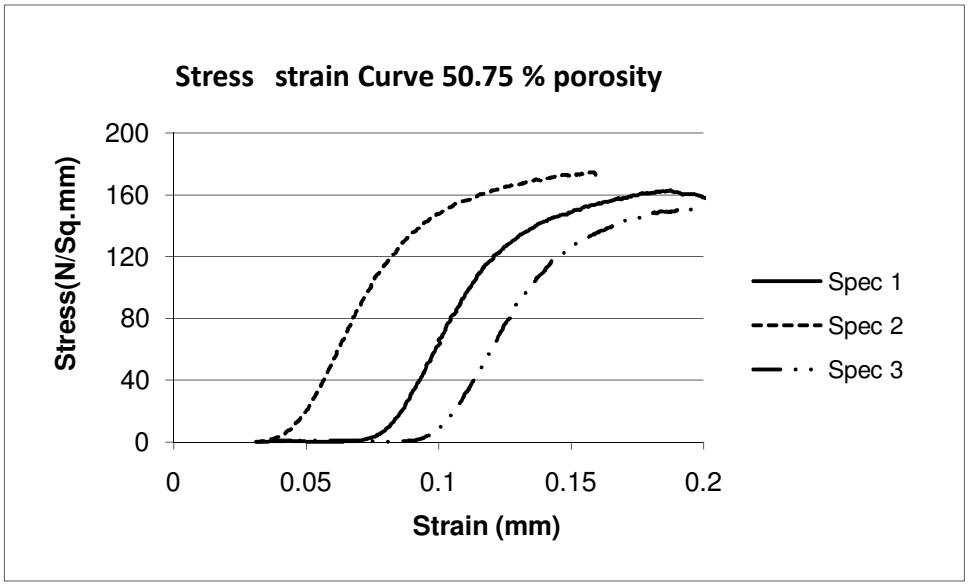


Figure 2 Stress Vs Strain curve Set 1

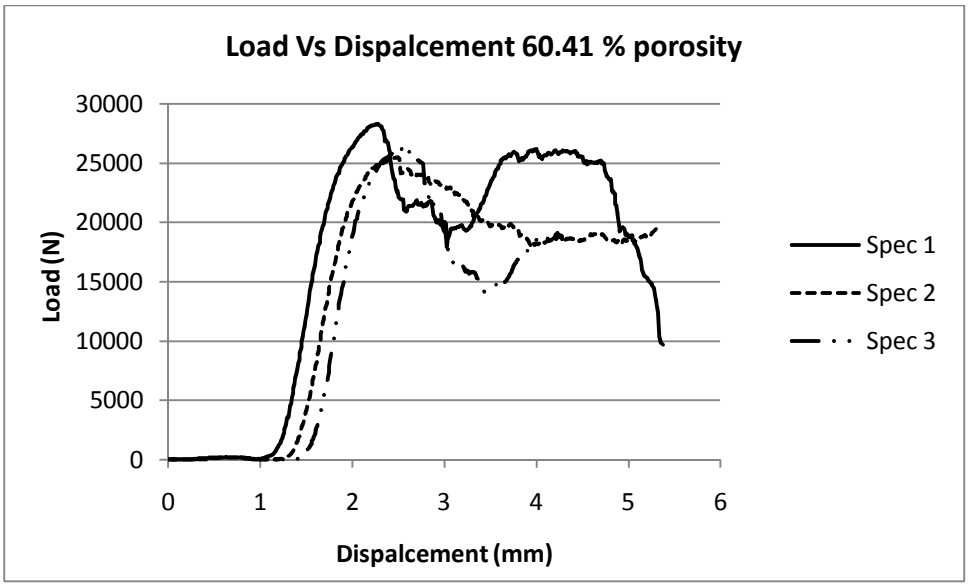


Figure 3 Load Vs Displacement Set 2

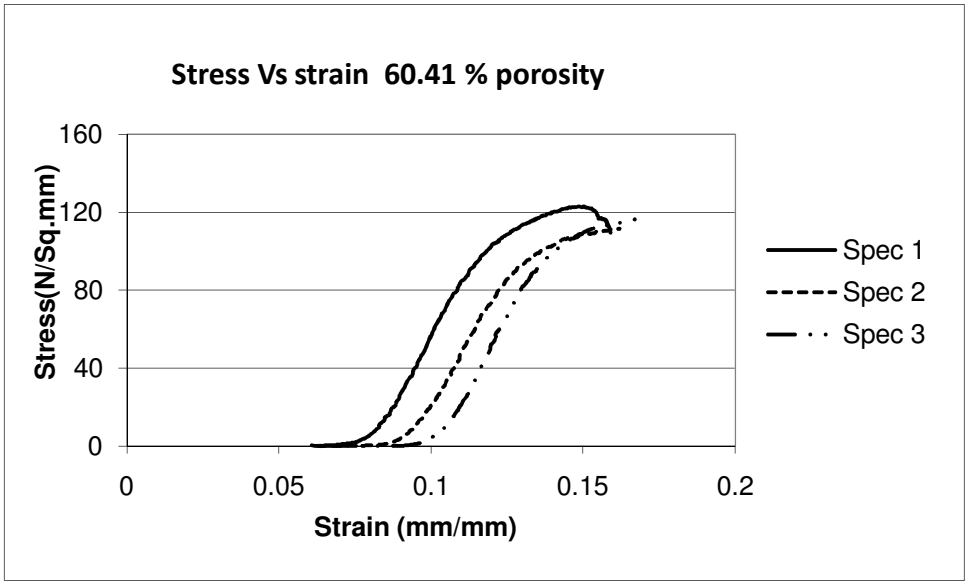


Figure 4 Stress Vs Strain curve Set 2

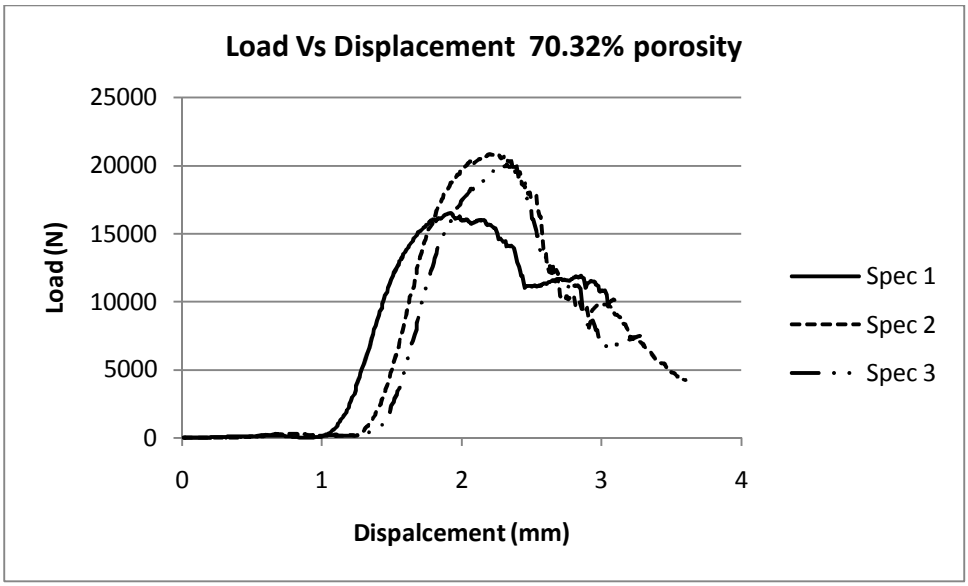


Figure 5 Load Vs Displacement Set 3

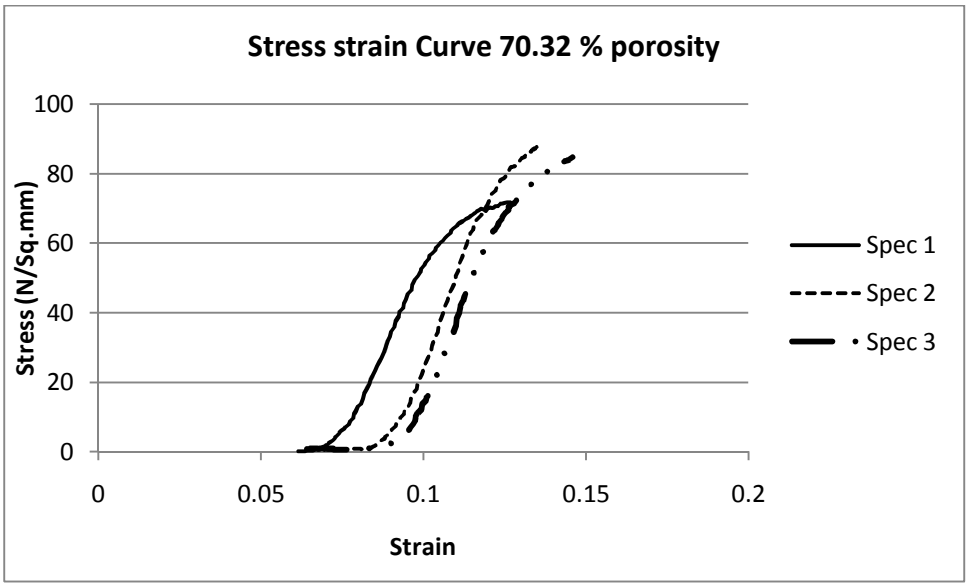


Figure 6 Stress Vs Strain curve Set 3

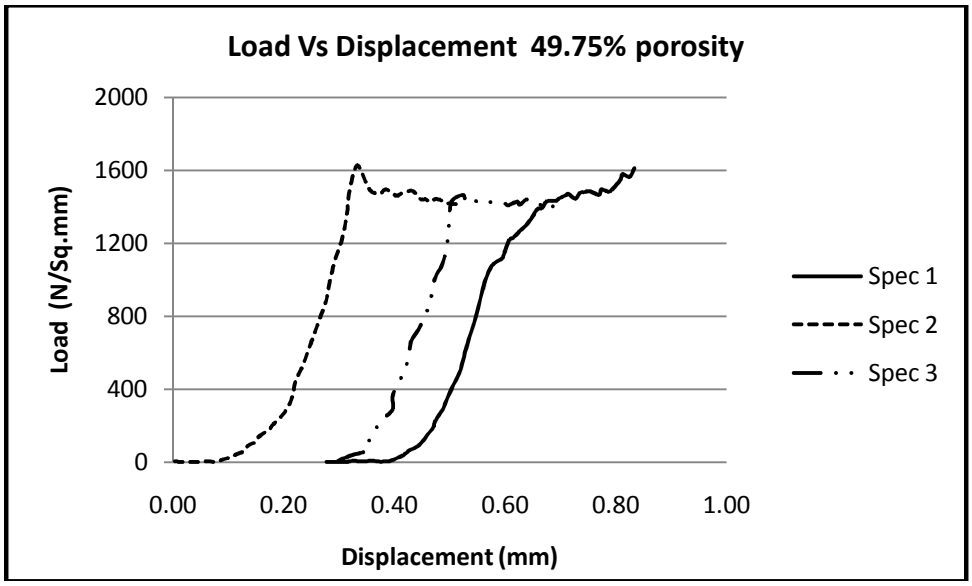


Figure 7 Load Vs Displacement Set 4

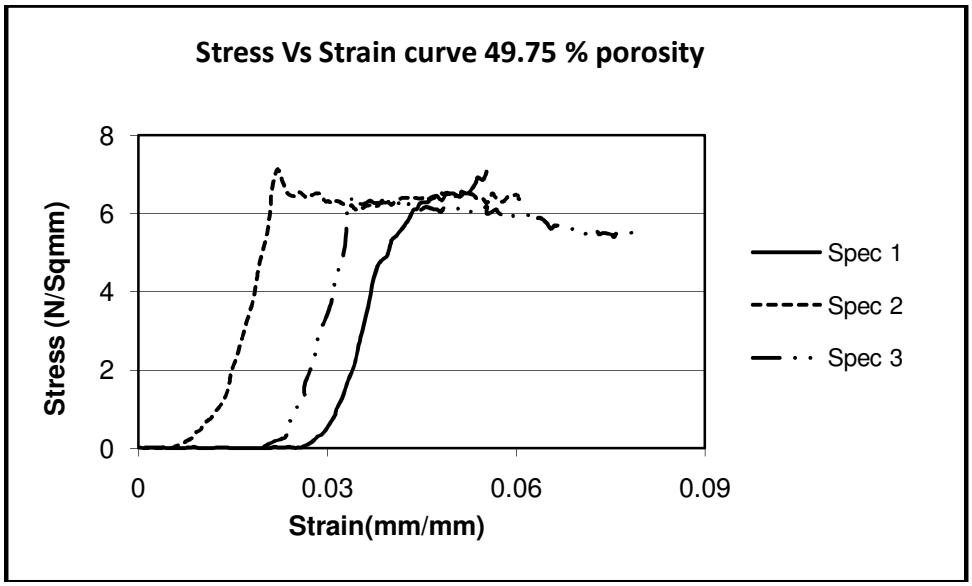


Figure 7 Stress Vs Strain curve Set 4

ACRONYMS

µm – Micrometers

3DP – 3D Printing

ASTM – American Standard Testing Method

BMMP - Biomechanical titanium mandibular prosthesis

CAD – Computer Aided Design

CAM – Computer Aided Manufacture

CAP - Calcium Phosphate

Co-Cr-Mo – Cobalt – Chromium – Molybdenum

CPTi - Commercially pure titanium

CT – Computer Tomography

DICOM - Digital Imaging and Communications in Medicine

DMLS - Direct Metal Laser Sintering

E - Elastic modulus

EBM – Electron Beam Melting

ECM - Extra Cellular Matrix

FDM – Fusion Deposition Method

FEA – Finite Element Analysis

GPa – Giga Pascals

HA - Hydroxyapatite

IAD - Interior Architecture Design

LENS - Laser Engineered Net Shaping

MHZ – Mega Hertz

MPa – Mega Pascals

MRI – Magnetic Resonance Imaging

N – Newtons

NEMA - National Electrical Manufacturers Association

NURBS – Non Uniform Relational B Spline

PCL - Polycaprolactone

PET – Positron Emission Tomography

PGA - Polyglycolides

PLA - Polylactides

PMMA - Polymethylmethacrylate

RP - Rapid Prototyping

RVE - Representative Volume Element

SEM – Scanning Electron Microscope

SFF – Solid Freeform fabrication

SLA – Stereolithography

SLM - Selective Laser Melting

SLS - Selective Laser Sintering

STL – Stereolithography file

Ta - Tantalum

TCP – Tri Calcium phosphate

Ti-6Al-4V – Titanium – 6Aliminum- 4 Vanadium

TiO_2 – Titanium Oxide

UHMW - Polyethylene Ultra-high-molecular-weight

Zr - Zirconium

ZrO_2 - Zirconia